PHILOSOPHICAL TRANSACTIONS OF THE ROYAL SOCIETY A MATHEMATICAL, PHYSICAL & ENGINEERING SCIENCES

Topographic Waves in a Stratified Elliptical Basin, with Application to the Lake of Lugano

L. A. Mysak, G. Salvade, K. Hutter and T. Scheiwiller

Phil. Trans. R. Soc. Lond. A 1985 **316**, 1-55
doi: 10.1098/rsta.1985.0055

Phil. Trans. R. Soc. Lond. A **316**, 1–55 (1985)

Printed in Great Britain

TOPOGRAPHIC WAVES IN A STRATIFIED ELLIPTICAL BASIN, WITH APPLICATION TO THE LAKE OF LUGANO

By L. A. MYSAK[1], G. SALVADÈ[2], K. HUTTER[3] and T. SCHEIWILLER[3]

[1] *Departments of Mathematics and Oceanography, The University of British Columbia, Vancouver, British Columbia, Canada V6T IW5*

[2] *Laboratorio di Fisica Terrestre, Istituto Cantonale Tecnico Sperimentale, CH-6952 Lugano–Trevano, Switzerland*

[3] *Laboratory of Hydraulics, Hydrology and Glaciology, ETH, CH-8092 Zurich, Switzerland*

(*Communicated by P. H. Roberts, F.R.S.* – *Received* 1 *September* 1983 – *Revised* 22 *May* 1984)

[Pullout 1]

CONTENTS

 [Published 26 September 1985

A theory is presented for the wind generation of topographic waves in a stratified, elongated lake. The stratification is modelled by a two-layer fluid with upper layer thickness $D_1 \ll D_2$, the characteristic lower layer depth. It is shown by means of scale analysis that to $O(D_1/D_2)$, the governing pair of equations for the barotropic stream function ψ and interfacial displacement ζ decouple, with ψ satisfying the linearized potential vorticity equation, which includes wind stress forcing. The solution of this equation is then substituted into the governing equation for ζ, which can now be solved in terms of the known forcing ψ. The solutions for ψ and ζ are next used to find $\boldsymbol{u}_1$ and $\boldsymbol{u}_2$, the upper and lower layer velocities respectively. To $O(D_1/D_2)$ the velocity field $\boldsymbol{u}_2$ is barotropic, whereas $\boldsymbol{u}_1$ consists of a barotropic part, a baroclinic part, and a directly forced wind component. The horizontal currents are generally surface intensified.

The general theory described is applied to an elliptically shaped basin in which the shoreline and depth contours form a family of confocal ellipses. For an exponential depth profile, simple solutions for the radial and azimuthal barotropic modes describing free, elliptically travelling waves are obtained by using a variational method. The corresponding solutions for ζ, $\boldsymbol{u}_1$ and $\boldsymbol{u}_2$ can be expressed in terms of elementary functions provided $r_1^2 \ll L^2$, where r_1 is the two-layer internal Rossby radius of deformation and L is the half-length of the lake.

The theory is applied to the Lake of Lugano, Switzerland, where a distinct 74 h oscillation in both the temperature and current records was observed during summer 1979. It is shown that the period, direction of phase propagation, isotherm-depth amplitude distribution along the lake, and horizontal current motion associated with this signal are consistent with the model of a free, fundamental-mode topographic wave that travels anticlockwise around an elliptical basin representative of the Lake of Lugano. From scaling arguments and cross-spectral analysis it is also demonstrated that the energy source for this wave is probably the wind along the shore at the southern end of the lake. However, a complete solution to the forced problem with the observed wind spectrum as input is not given.

The existence of topographic waves (rotational modes) in the Lake of Lugano is surprising, considering the small horizontal dimensions of this Alpine lake (approximately 17 km × 1.5 km). Thus it would be of considerable interest to apply the theory developed here to other intermontane lakes to see whether low-frequency topographic waves of this scale are a common occurrence in nature.

1. Introduction

Recent temperature and current measurements from two intermontane Swiss lakes show persistent low-frequency fluctuations with a characteristic period of a few days. In the Lake of Zurich, Mortimer & Horn (1982) and Horn *et al.* (1983) detected a distinct 100 h signal in both temperature and current meter data collected during summer 1978, but Hutter *et al.* (1983) noted the existence of a 74 h oscillation in the temperature records made during summer 1979 at the Lake of Lugano. Since these lakes are relatively small (roughly 20 km long and 2 km wide), the periods of the internal gravity wave seiches are quite short (of the order of one day or less; see Mortimer & Horn (1982); Hutter *et al.* (1983)) and are thus quite separate from the 3 to 4 day periods described above. Such internal seiches will be excluded from this study. To explain the longer-period signals two suggestions have been made: (i) direct meteorological forcing (Mortimer & Horn 1982), and (ii) second-class (topographic) waves (Hutter *et al.* 1983).

The purpose of this paper is to demonstrate that, remarkably, the low-frequency signals in the elongated Swiss lakes are probably due to small-scale topographic waves that freely

propagate anticlockwise around the basin. Topographic waves (also known as vortex modes, rotational modes and second-class waves) can only exist in a rotating fluid with variable bottom topography. In the northern hemisphere, where the Coriolis parameter is positive, shallower water is always to the right of the direction of phase propagation. The current motions associated with topographic waves are obtained from the solution of a potential vorticity equation (LeBlond & Mysak 1978, ch. 3). Topographic waves have been observed in the ocean (see, for example, Mysak 1980), and also in the relatively large Laurentian Great Lakes in which Coriolis effects are known to be important (see, for example, Simons 1975; Csanady 1976; Saylor *et al.* 1980). However, in diminutive lakes such as the Lake of Lugano, one does not expect Coriolis effects to play a significant role in the dynamic balance.

For the Lake of Lugano, it appears that the energy source for these topographic waves is the wind blowing along the shore over the southern end of the lake. The wind-stress spectrum for this component is broadly peaked between two and three days. Further, a cross-spectral analysis of the wind and water temperature fluctuations from this location shows a marginally significant correlation at 74 h. At other lake locations, however, the wind has little energy at around three days and the wind and temperature fluctuations are not significantly correlated at 74 h. Thus it is evident that the 74 h temperature oscillation across the width of the basin in the Lake of Lugano is not simply due to direct meteorological forcing over the whole lake, but is wind-generated. It is believed that a similar situation also occurs in the Lake of Zurich, in contrast to the Mortimer & Horn (1982) conjecture regarding direct meteorological forcing. Recently, Mysak (1985) has shown that the 100 h signal observed there is very close to the theoretical period of a fundamental-mode topographic wave for an elliptical lake representative of this basin.

In the theoretical part of this article (§§ 2–5), a model is developed for wind-generated topographic waves in an elongated two-layer lake in which the upper layer thickness D_1 is small by comparison with D_2, the characteristic depth of the lower layer. The general stratified theory developed in § 3 is applied to an elliptically shaped lake in §§ 4, 5. In § 4 a brief review is given of a new class of solutions (Mysak 1985) for elliptical topographic waves that travel around a basin whose shoreline and depth contours form a family of confocal ellipses. The barotropic solution given in § 4 is used in § 5 to find the wave-induced interfacial displacement and horizontal velocity field in each layer. An important feature of the model used here is that the side walls of the lake are assumed to be vertical, down to a depth below the interface (see figure 1). This is a reasonable assumption for most intermontane lakes, and is necessary to avoid awkward singularities that would otherwise occur in the governing two-layer equations if the depth vanished at the shoreline. Since the shoreline depth is zero for the elliptic paraboloid, the classical Ball (1965) solution cannot be readily extended to a two-layer stratified lake.

The theory developed in §§ 2–5 is applied in § 6 to the Lake of Lugano where, during July–August 1979, an extensive field programme was undertaken to study the lake's response to meteorological forcing. The low-frequency (i.e. subdiurnal) fluctuations of the wind, current and temperature are statistically analysed, and the results strongly support the hypothesis for a fundamental-mode topographic wave with a 74 h period that propagates anticlockwise around the lake. It is important to emphasize, however, that the theory presented in this paper could also be supplied to other 'small' intermontane lakes. Also, with one or two minor modifications (specified later), the theory could be used to study low-frequency waves in large,

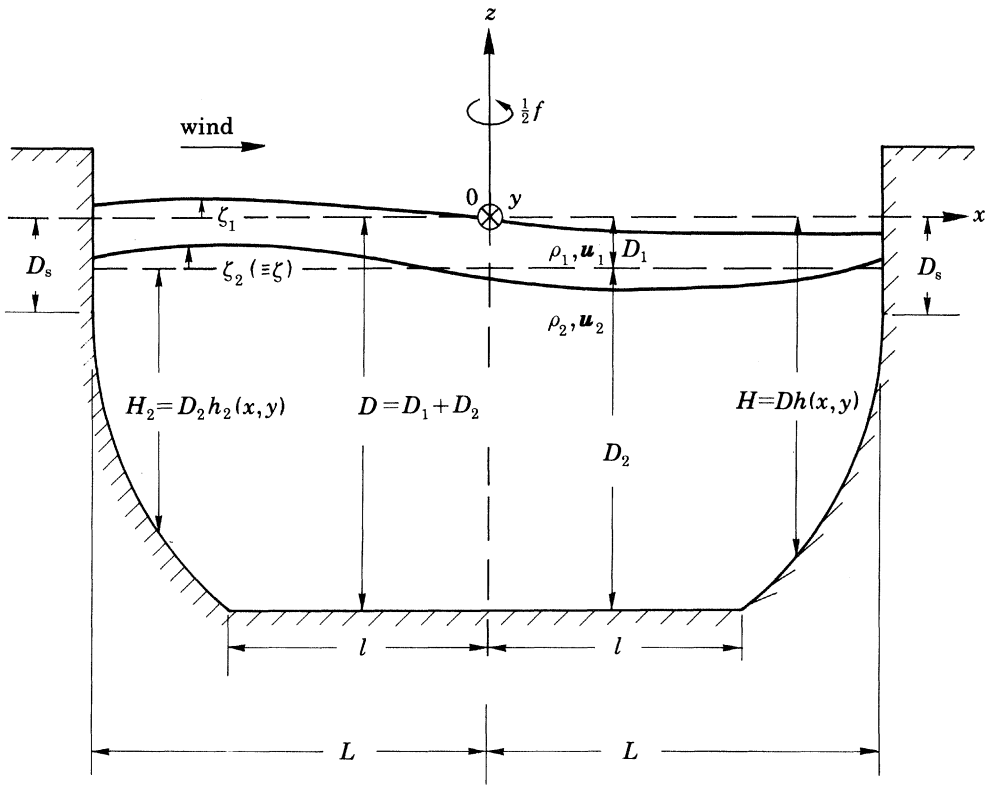

FIGURE 1. Sketch of rotating two-layer lake model used in this paper. The right-handed coordinates (x, y, z) are centred on the lake surface. The vector $\boldsymbol{u}_j = (u_j, v_j)$ denotes the depth-averaged horizontal velocity in layer j.

stratified deep lakes, such as the Lakes of Geneva and Constance and the Laurentian Great Lakes. In particular, the theory should be capable of resolving the internal Kelvin wave against topographic wave controversy that has been raised, for example, with regard to low-frequency signals that have been observed propagating along the south shore of Lake Ontario (see, for example, Simons 1980, p. 124).

2. GOVERNING EQUATIONS

We consider wind-driven small-amplitude motions in a uniformly rotating, two-layer lake, as illustrated in figure 1. We assume that the upper layer is thin ($D_1 \ll D_2$) and has an equilibrium depth $D_1 < D_s$, the depth at the lake edge. The assumption of vertical side walls is reasonable for many intermontane lakes; it also simplifies the mathematical analysis because depth variations are confined to the lower layer. In such a model with a deep lower layer, bottom-friction effects are negligible (Huang & Saylor 1982). The governing equation, in which the surface wind stress is modelled as a body force distributed over the upper layer, can be written as (LeBlond & Mysak 1978, p. 542)

$$\left.\begin{aligned} u_{1_t} - fv_1 &= -g\zeta_{1_x} + \tau^x/\rho_1 D_1, \\ v_{1_t} + fu_1 &= -g\zeta_{1_y} + \tau^y/\rho_1 D_1, \end{aligned}\right\} \tag{2.1}$$

$$D_1(u_{1_x} + v_{1_y}) = \zeta_{2_t} - \zeta_{1_t}, \tag{2.2}$$

$$\left.\begin{aligned} u_{2_t} - fv_2 &= -g\zeta_{1_x} - \epsilon g(\zeta_{2_x} - \zeta_{1_x}), \\ v_{2_t} + fu_2 &= -g\zeta_{1_y} - \epsilon g(\zeta_{2_y} - \zeta_{1_y}), \end{aligned}\right\} \tag{2.3}$$

$$(H_2 u_2)_x + (H_2 v_2)_y = -\zeta_{2_t}, \tag{2.4}$$

where $\boldsymbol{\tau} = (\tau^x, \tau^y)$ is the surface wind stress vector and $\epsilon = (\rho_2 - \rho_1)/\rho_2 \ll 1$, (u_1, v_1) and (u_2, v_2) are the x- and y-components of the layer velocities, ζ_1, ζ_2 are the free surface and the interface displacements, g is the gravity constant and f the Coriolis parameter. In ensuing calculations the subscripts 1 and 2 will indicate the upper and lower layers, respectively. Furthermore, superscripts x, y indicate (vector) components in the x- and y-directions, respectively, and subscripts t, x and y denote partial differentiation with respect to t, x and y, respectively.

To filter out all surface gravity waves and the barotropic Kelvin wave from the analysis, we invoke the rigid-lid approximation, which corresponds to neglecting the term $-\zeta_{1_t}$ in (2.2). Since typically $\epsilon = O(2 \times 10^{-3})$ for most lakes during summer, $\epsilon g\zeta_{1_x} \ll g\zeta_{1_x}$ and $\epsilon g\zeta_{1_y} \ll g\zeta_{1_y}$. Thus we shall also neglect the terms $-\zeta_{1_x}$ and $-\zeta_{1_y}$ in (2.3).

Under the rigid-lid approximation, the sum of (2.2) and (2.4) yields

$$(D_1 u_1 + H_2 u_2)_x + (D_1 v_1 + H_2 v_2)_y = 0; \tag{2.5}$$

hence we can introduce a stream function $\psi = \psi(x, y, t)$ for the depth-averaged flow:

$$-\psi_y = D_1 u_1 + H_2 u_2, \quad \psi_x = D_1 v_1 + H_2 v_2. \tag{2.6}$$

The function ψ is called the *barotropic* or *mass transport* stream function. To study topographic waves in a stratified fluid it is most convenient to work with a pair of coupled equations for ψ and ζ_2, the latter quantity representing the *baroclinic* part of the motion. The derivation of these equations, without $\boldsymbol{\tau}$, is given in Allen (1975) and in Wright & Mysak (1977). Here we quote only the final results, with $\boldsymbol{\tau}$ now included:

$$\begin{aligned} &\nabla \cdot (H^{-1} \nabla \psi_t) + f(\nabla \psi \times \nabla H^{-1}) \cdot \hat{\boldsymbol{z}} \\ &\qquad = -g' D_1 (\nabla \zeta \times \nabla H^{-1}) \cdot \hat{\boldsymbol{z}} + \frac{1}{\rho_1} \left[\nabla \times (\boldsymbol{\tau} H^{-1}) + \frac{H}{D_1} \boldsymbol{\tau} \times \nabla H^{-1} \right] \cdot \hat{\boldsymbol{z}}, \end{aligned} \tag{2.7}$$

$$\begin{aligned} &H \nabla^2 \zeta_t - \frac{H^2}{g' D_1 H_2} \mathscr{L} \zeta_t + \frac{D_1}{H_2} \nabla \zeta_t \cdot \nabla H - \frac{f D_1}{H_1} (\nabla \zeta \times \nabla H) \cdot \hat{\boldsymbol{z}} \\ &\qquad = \frac{1}{g' H_2} [\nabla (\mathscr{L} \psi) \times \nabla H] \cdot \hat{\boldsymbol{z}} - \frac{H \mathscr{L}}{\rho_1 g' D_1 f} (\nabla \times \mathscr{L} \boldsymbol{\tau}) \cdot \hat{\boldsymbol{z}}, \end{aligned} \tag{2.8}$$

where $\hat{\boldsymbol{z}}$ is a unit vector in the z-direction, $\mathscr{L} = \partial_{tt} + f^2$, and $g' = \epsilon g$, the reduced gravity. For convenience, we have written ζ for ζ_2.

In the absence of stratification and wind forcing, the right side of (2.7) is zero and the equation reduces to the familiar potential vorticity equation for barotropic topographic waves (see LeBlond & Mysak 1978, equation (20.11)). In a stratified fluid with topography, the first term on the right side of (2.7) produces the so-called joint baroclinic-topographic effect. That is, the term acts as a vorticity input for barotropic currents. Holland (1973) has shown that this coupling term combines additively with the wind stress terms to produce an enhanced western boundary transport in a wind-driven ocean-circulation model of the Gulf stream. For deep lakes, however, this coupling term is negligible, as will be seen from a scale analysis in

§3. For a fluid of constant depth and no wind forcing, only the first two terms on the left side of (2.8) survive, yielding the long-wave equation for internal gravity waves and Kelvin waves that propagate with speed $c_i = (g' D_1 H_2/H)^{\frac{1}{2}}$ (here and henceforth the index i will stand for 'internal'). When H is variable such waves are slightly modified by the relatively small third and fourth terms on the left side of (2.8), and are driven by the barotropic component of the motion (ψ) and the wind stress curl.

Once ψ and ζ are known from the solution of the coupled system (2.7) and (2.8), the velocity fields can be found from the relations

$$\mathscr{L}\boldsymbol{u}_1 = \frac{1}{H}\left[\hat{\boldsymbol{z}}\times\nabla(\mathscr{L}\psi) + H_2 g'(\nabla\zeta_t - f\hat{\boldsymbol{z}}\times\nabla\zeta) + \frac{H_2}{\rho_1 D_1}(\boldsymbol{\tau}_t - f\hat{\boldsymbol{z}}\times\boldsymbol{\tau})\right], \tag{2.9}$$

$$\mathscr{L}\boldsymbol{u}_2 = \frac{1}{H}\left[\hat{\boldsymbol{z}}\times\nabla(\mathscr{L}\psi) - D_1 g'(\nabla\zeta_t - f\hat{\boldsymbol{z}}\times\nabla\zeta) - \frac{1}{\rho_1}(\boldsymbol{\tau}_t - f\hat{\boldsymbol{z}}\times\boldsymbol{\tau})\right]. \tag{2.10}$$

The first and second terms in (2.9) and (2.10) represent, respectively, the barotropic and baroclinic parts of the current; the third term is a directly forced wind-driven component.

As a final simplification in this section we invoke the low-frequency approximation

$$\mathscr{L} = \partial_{tt} + f^2 \simeq f^2, \tag{2.11}$$

which filters out the internal gravity waves (for example, the internal seiches) and the internal Kelvin wave from the analysis. (Internal gravity wave seiches with a period of 74 h do not occur in the two-layer Lake of Lugano model during summer when the stratification is characterized by a sharp thermocline near 10 m (see figure 15). Hutter *et al.* (1983) showed that in a numerical two-layer model of the Lake of Lugano that incorporates the actual topography, the internal seiche periods are up to 24 h long. Moreover, they found that each peak in the observed temperature spectra covering the period range up to 24 h could be identified with one of the computed internal seiche periods.) For oscillations with periods of 3 days and longer, $\partial_t \sim \omega \leqslant 2.42\times10^{-5}\ \mathrm{s}^{-1}$ and therefore $\omega^2/f^2 \leqslant 0.05$ for $f = 1.05\times10^{-4}\ \mathrm{s}^{-1}$ (for example, at the Lake of Lugano). Therefore, the approximation (2.11) introduces a small percentage error for the topographic waves. For large lakes (for example, the Laurentian Great Lakes) the omission of the internal Kelvin wave mode may not be permissible (Simons 1980). However, for smaller lakes we argue that its wavelength is too long for the wave to wrap itself around the inside of the basin. For the Lakes of Lugano and Zurich, a typical internal wave phase speed is $c_i = 45\ \mathrm{cm\ s}^{-1}$ (Mortimer & Horn 1982; Hutter *et al.* 1983). For a period of 3 days, the corresponding wavelength of a Kelvin wave is 117 km, which is roughly three times the circumference of these Swiss lakes.

3. Scale analysis of the governing equations

The first scale analysis of the coupled equations (2.7) and (2.8) with $\boldsymbol{\tau} = \mathbf{0}$ was done by Allen (1975) in the context of free coastal trapped waves that propagate along an exponential shelf–slope bottom topography. In his non-dimensional version of these equations, there appeared the dimensionless parameter $\lambda = r_i/L_T$, where r_i is the internal Rossby radius of deformation (i.e. $r_i = c_i/f$) and L_T is a characteristic horizontal scale of the bottom topography.

Off the coast of Oregon, and in other eastern boundary current régimes during summer, $r_i = O(15\text{ km})$ and $L_T = O(100\text{ km})$, so that $\lambda \ll 1$. Thus Allen was able to study the strength of the coupling between ψ (shelf waves) and ζ (internal Kelvin waves) through a perturbation expansion in λ. For many intermontane lakes, and especially those in Switzerland, $r_i = O(4\text{ km})$ in summer and $L_T = O(5\text{ km})$, so that $\lambda = O(1)$. Hence Allen's perturbation analysis cannot be used to solve (2.7) and (2.8) for low-frequency lake-motions.

Another type of low-frequency wave that can arise out of the solution of (2.7) and (2.8) with $\boldsymbol{\tau} = \mathbf{0}$, is the bottom-trapped topographic Rossby wave studied by Rhines (1970) (see also LeBlond & Mysak 1978, §20). In this case the scaling of these equations yields the non-dimensional parameter $\delta_s = |\nabla H| L_T/D$, where D is the total depth and L_T is the same as defined above. For typical continental slope regions, $|\nabla H| = O(10^{-2})$, $L_T = O(50\text{ km})$ and $D = O(4\text{ km})$. Thus $\delta_s = O(10^{-1})$ and a perturbation expansion in δ_s can be used to solve the governing system of equations. For the Swiss lakes, we typically have $|\nabla H| = 3 \times 10^{-2}$, $L_T = 5$ km and $D = 200$ m, yielding $\delta_s = 0.75$. So this approach does not apply either.

A suitable scale analysis of (2.7) and (2.8) that can be applied to many lakes has, however, been recently developed by Gratton (1982, 1983). But before describing this work, it is helpful to first estimate the relative importance of the different wind stress terms since these were not included in Gratton's analysis.

(a) *Wind stress forcing mechanisms*

The wind stress terms in (2.7) can be written as (upon neglecting the common factor ρ_1)

$$\left[\nabla \times (\boldsymbol{\tau} H^{-1}) + \frac{H}{D_1}\,\boldsymbol{\tau} \times \nabla H^{-1}\right] \cdot \hat{\boldsymbol{z}} = \Big[\underbrace{H^{-1}\nabla \times \boldsymbol{\tau}}_{\text{(i)}} + \underbrace{(\nabla H^{-1}) \times \boldsymbol{\tau}}_{\text{(ii)}} + \underbrace{\frac{H}{D_1}\,\boldsymbol{\tau} \times \nabla H^{-1}}_{\text{(iii)}}\Big] \cdot \hat{\boldsymbol{z}}. \tag{3.1}$$

The first term on the left represents the driving term that arises in a strictly barotropic lake model with topography (Simons 1980, p. 99), whereas the second term on the left appears because of the stratification. For lakes, the wind stress curl term (i) on the right side of (3.1) is generally small compared to the topographic driving terms (ii) and (iii). This is because L_W, the horizontal length scale for $\boldsymbol{\tau}$, is generally much larger than the topographic length scale L_T (Simons 1980, p. 73). Thus the ratio of terms (i):(ii) is $O(L_T/L_W) \ll 1$. In practice, therefore, one usually takes $\boldsymbol{\tau} = \boldsymbol{\tau}(t)$ in lake wave models that include wind forcing (see, for example, Birchfield & Hickie 1977; Huang & Saylor 1982). For a spatially constant $\boldsymbol{\tau}$, it also follows that the wind stress curl term in (2.8) drops out.

Finally, comparing the two topographic driving terms on the right side of (3.1), we find that the ratio of terms (ii) : (iii) is $O(D_1/D)$. So for a deep lake with a thin upper layer (as in figure 1), we can neglect term (ii) as well, leaving term (iii) as the sole wind-forcing term in our system. For convenience, we now rewrite here the simpler forms of (2.7) and (2.8), which take into account these approximations and the low-frequency approximation (2.11):

$$\nabla \cdot (H^{-1}\nabla\psi) + f(\nabla\psi \times \nabla H^{-1}) \cdot \hat{\boldsymbol{z}} = -g' D_1 (\nabla\zeta \times \nabla H^{-1}) \cdot \hat{\boldsymbol{z}} + \frac{H}{\rho_1 D_1}\,(\boldsymbol{\tau} \times \nabla H^{-1}) \cdot \hat{\boldsymbol{z}}, \tag{3.2}$$

$$\frac{1}{H}\nabla^2\zeta_t - \frac{f^2}{g' D_1 H_2}\,\zeta_t - \frac{D_1}{H_2}\,\nabla\zeta_t \cdot \nabla H^{-1} + \frac{f D_1}{H_2}\,(\nabla\zeta \times \nabla H^{-1}) \cdot \hat{\boldsymbol{z}} = -\frac{f^2}{g' H_2}\,(\nabla\psi \times \nabla H^{-1}) \cdot \hat{\boldsymbol{z}}. \tag{3.3}$$

PHILOSOPHICAL TRANSACTIONS OF THE ROYAL SOCIETY A MATHEMATICAL, PHYSICAL & ENGINEERING SCIENCES

Invoking (2.11) in (2.9) and (2.10) we also find

$$\boldsymbol{u}_1 = \frac{1}{H}\left[\hat{\boldsymbol{z}}\times\nabla\psi + \frac{H_2 g'}{f^2}(\nabla\zeta_t - f\hat{\boldsymbol{z}}\times\nabla\zeta) + \frac{H_2}{\rho_1 D_1 f^2}(\boldsymbol{\tau}_t - f\hat{\boldsymbol{z}}\times\boldsymbol{\tau})\right], \tag{3.4a}$$

$$\boldsymbol{u}_2 = \frac{1}{H}\left[\hat{\boldsymbol{z}}\times\nabla\psi - \frac{D_1 g'}{f^2}(\nabla\zeta_t - f\hat{\boldsymbol{z}}\times\nabla\zeta) - \frac{1}{\rho_1 f^2}(\boldsymbol{\tau}_t - f\hat{\boldsymbol{z}}\times\boldsymbol{\tau})\right]. \tag{3.4b}$$

(*b*) *The Gratton scaling*

Because of the variable depth H, the coupled equations (3.2) and (3.3) have variable coefficients and are not readily solved by analytical methods. However, it was shown by Gratton (1982, 1983) that for a deep fluid with a thin upper layer (i.e. $D_1 \ll D_2$), the first coupling term on the right side of (3.2) is of $O(D_1/D_2)$ compared with the ψ terms on the left side. Therefore, to a first approximation, this term can be dropped and the equations become uncoupled. Then one can solve (3.2) for ψ, and substitute this solution into the right side of (3.3). The latter equation can then be integrated to find ζ. Finally, $\boldsymbol{u}_1$ and $\boldsymbol{u}_2$ can be found from (3.4*a*) and (3.4*b*).

To show this we now introduce the following set of non-dimensional variables, denoted by primes:

$$\psi = \psi_0\psi', \quad \zeta = \zeta_0\zeta', \quad \boldsymbol{\tau} = \tau_0\boldsymbol{\tau}', \quad (x, y) = (Lx', Ly'), \quad t = f^{-1}t', \tag{3.5}$$

where τ_0 is a characteristic wind stress scale (determined from observations), L is the lake half-length (see figure 1), and ψ_0 and ζ_0 are amplitude scales to be determined later. Substituting (3.5) into (3.2) and (3.3) and using the relations (see figure 1)

$$H = Dh, \quad H_2 = D_2 h_2, \tag{3.6}$$

where h, h_2, $|\nabla_{x'} h|$, $|\nabla_{x'} h_2|$ are all of order unity, we obtain the scaled equations

$$\nabla\cdot(h^{-1}\nabla\psi_t) + (\nabla\psi\times\nabla h^{-1})\cdot\hat{\boldsymbol{z}} = -C_1(\nabla\zeta\times\nabla h^{-1})\cdot\hat{\boldsymbol{z}} + \left(\frac{LD\tau_0}{f\rho_1 D_1\psi_0}\right)(h\boldsymbol{\tau}\times\nabla h^{-1})\cdot\hat{\boldsymbol{z}}, \tag{3.7}$$

$$\frac{1}{h}\left(\nabla^2\zeta_t - \frac{L^2 h}{r_i^2 h_2}\zeta_t\right) - \frac{D_1}{D_2 h_2}\nabla\zeta_t\cdot\nabla h^{-1} + \frac{D_1}{D_2 h_2}(\nabla\zeta\times\nabla h^{-1})\cdot\hat{\boldsymbol{z}} = -C_2 h_2^{-1}(\nabla\psi\times\nabla h^{-1})\cdot\hat{\boldsymbol{z}}, \tag{3.8}$$

where the *coupling coefficients* C_i are given by

$$C_1 = \frac{g' D_1\zeta_0}{f\psi_0}, \quad C_2 = \frac{f\psi_0}{g' D_2\zeta_0}, \tag{3.9}$$

and $r_i = (g' D_1 D_2/Df^2)^{\frac{1}{2}}$ is the internal Rossby radius. Note that in (3.7) and (3.8) we have dropped the primes on the scaled (non-dimensional) variables.

Let us now suppose that (3.7) and (3.8) are strongly coupled, i.e. that C_1 and C_2 are both $O(1)$. Then (3.9) implies that

$$\zeta_0 = O(f\psi_0/g' D_1) \tag{3.10}$$

and

$$\zeta_0 = O(f\psi_0/g' D_2). \tag{3.11}$$

We observe that independent of the ψ_0 scale, (3.10) and (3.11) are consistent *only if* $D_1/D_2 = O(1)$. Since we are concerned with the case $D_1 \ll D_2$, it follows that C_1 and C_2 cannot

both be of order unity, i.e. that (3.7) and (3.8) are only weakly coupled. Suppose we assume that (3.10) applies and thus choose

$$\zeta_0/\psi_0 = f/(g'D_1) \tag{3.12}$$

as the scaling for the ratio ζ_0/ψ_0. Then $C_1 = 1$ and $C_2 = D_1/D_2 \ll 1$. Therefore to $O(D_1/D_2)$, equation (3.8) reduces to

$$(\nabla^2 - L^2/r_i^2)\,\zeta_t = 0, \tag{3.13}$$

where we have used $h/h_2 = 1 + O(D_1/D_2)$. Apart from (3.13) not being a conventional wave equation for internal motions, the scale choice (3.12) leads to an unrealistically large value for the ζ_0 scale (for the Lake of Lugano, $\zeta_0 \approx 50$ m, which is several times the upper layer depth (10 m)).

Hence we are compelled to choose the scaling (3.11) (Gratton's choice, which was based on data from the Strait of Georgia, British Columbia). Putting

$$\zeta_0/\psi_0 = f/(g'D_2), \tag{3.14}$$

we find $C_2 = 1$ and $C_1 = D_1/D_2 \ll 1$. We choose the ψ_0 scale by setting the coefficient of the wind stress term in (3.7) equal to unity, which gives

$$\psi_0 = LD\tau_0/(f\rho_1 D_1). \tag{3.15}$$

Substituting (3.15) into (3.14) gives an expression for ζ_0 in terms of the wind stress scale τ_0:

$$\zeta_0 = LD\tau_0/(\rho_1 g' D_1 D_2). \tag{3.16}$$

Also, substituting $\psi_0 = LDU$ into (3.15), where U is the velocity scale for the barotropic currents (see equation (2.6)), we find

$$U = \tau_0/(\rho_1 f D_1). \tag{3.17}$$

Using (3.14) and (3.15) in (3.7) and (3.8), we obtain, correct to $O(D_1/D_2)$,

$$\nabla\cdot(h^{-1}\nabla\psi_t) + (\nabla\psi\times\nabla h^{-1})\cdot\hat{\boldsymbol{z}} = (h\boldsymbol{\tau}\times\nabla h^{-1})\cdot\hat{\boldsymbol{z}}, \tag{3.18}$$

$$(\nabla^2 - S^{-1})\,\zeta_t = -(\nabla\psi\times\nabla h^{-1})\cdot\hat{\boldsymbol{z}}, \tag{3.19}$$

as the appropriate non-dimensional equations for ψ and ζ. In (3.19) note that we have introduced the stratification parameter S, defined as

$$S = r_i^2/L^2. \tag{3.20}$$

For the derivation of (3.19) it is important that $h_2 \neq 0$ (as illustrated in figure 1). If $h_2 = 0$, the third and fourth terms on the left side of (3.8) are not uniformly $O(D_1/D_2)$ and hence could not be neglected. If an elliptic paraboloid contained a two-layer fluid, then clearly $h_2 = 0$ where the interface touches the basin wall and (3.19) would not be valid. Thus Ball's (1965) solution for second-class waves in an elliptic paraboloid could not be easily extended to the stratified case by our analysis.

PHILOSOPHICAL TRANSACTIONS OF THE ROYAL SOCIETY A MATHEMATICAL, PHYSICAL & ENGINEERING SCIENCES

Substituting (3.5) into (3.4a, b) and using (3.14), (3.15), $\psi_0 = LDU$ and U for the velocity scale, we obtain the following formulae:

$$\boldsymbol{u}_1 = \frac{1}{h}\left\{\hat{\boldsymbol{z}}\times\nabla\psi + h_2\left[(\nabla\zeta_t - \hat{\boldsymbol{z}}\times\nabla\zeta) + \frac{D_2}{D}(\boldsymbol{\tau}_t - \hat{\boldsymbol{z}}\times\boldsymbol{\tau})\right]\right\}, \tag{3.21}$$

$$\boldsymbol{u}_2 = \frac{1}{h}\left\{\hat{\boldsymbol{z}}\times\nabla\psi - \frac{D_1}{D_2}\left[(\nabla\zeta_t - \hat{\boldsymbol{z}}\times\nabla\zeta) + \frac{D_2}{D}(\boldsymbol{\tau}_t - \hat{\boldsymbol{z}}\times\boldsymbol{\tau})\right]\right\}. \tag{3.22}$$

To $O(D_1/D_2)$ these can be approximated by

$$\boldsymbol{u}_1 = \frac{1}{h}[\hat{\boldsymbol{z}}\times\nabla\psi + h(\nabla\zeta_t - \hat{\boldsymbol{z}}\times\nabla\zeta + \boldsymbol{\tau}_t - \hat{\boldsymbol{z}}\times\boldsymbol{\tau})], \tag{3.23a}$$

$$\boldsymbol{u}_2 = \frac{1}{h}\hat{\boldsymbol{z}}\times\nabla\psi. \tag{3.23b}$$

Thus for deep lakes, the lower layer current associated with topographic waves is essentially barotropic, whereas the upper layer current consists of a barotropic part, a baroclinic part and a contribution directly forced by the wind. Hence we conclude that the current motions are generally surface intensified. As will be seen in §6, this is certainly the case for the Lake of Lugano, for which the scale analysis applies.

(*c*) *Boundary conditions*

To solve (3.18) and (3.19) in some domain $\mathscr{D}$ for a given $\boldsymbol{\tau}$, we have to prescribe initial values for ψ and ζ and the boundary conditions on $\partial\mathscr{D}$, the boundary of $\mathscr{D}$. The first boundary condition we impose is that the total mass flux normal to $\partial\mathscr{D}$ must vanish: in non-dimensional variables this can be written as $\hat{\boldsymbol{n}}\cdot(D_1\boldsymbol{u}_1 + D_2 h_2 \boldsymbol{u}_2)\,D^{-1} = 0$ on $\partial\mathscr{D}$, where $\hat{\boldsymbol{n}}$ is a unit vector perpendicular to $\partial\mathscr{D}$. On substituting for $\boldsymbol{u}_1$ and $\boldsymbol{u}_2$ from (3.21) and (3.22), this reduces to

$$\hat{\boldsymbol{n}}\cdot(\hat{\boldsymbol{z}}\times\nabla\Psi) = 0 \quad \text{on } \partial\mathscr{D}. \tag{3.24}$$

Since $\hat{\boldsymbol{n}}\cdot(\hat{\boldsymbol{z}}\times\nabla\psi) = (\hat{\boldsymbol{n}}\times\hat{\boldsymbol{z}})\cdot\nabla\psi = \hat{\boldsymbol{s}}\cdot\nabla\psi$, where $\hat{\boldsymbol{s}}$ is a unit vector tangential to $\partial\mathscr{D}$, (3.24) implies $\partial\psi/\partial s = 0$ on $\partial\mathscr{D}$, or $\psi =$ constant on $\partial\mathscr{D}$. Thus without loss of generality, we take

$$\psi = 0 \quad \text{on } \partial\mathscr{D}. \tag{3.25}$$

Next we require $\hat{\boldsymbol{n}}\cdot\boldsymbol{u}_i = 0$ on $\partial\mathscr{D}$ for each layer i. Upon again using (3.21) and (3.22), together with (3.24), we find

$$\begin{aligned}\frac{\partial}{\partial n}\frac{\partial\zeta}{\partial t} - \frac{\partial\zeta}{\partial s} &= -\frac{D_2}{D}(\boldsymbol{n}\cdot\boldsymbol{\tau}_t - \hat{\boldsymbol{s}}\cdot\boldsymbol{\tau}) \\ &= -\hat{\boldsymbol{n}}\cdot\boldsymbol{\tau}_t + \hat{\boldsymbol{s}}\cdot\boldsymbol{\tau} \quad \text{on } \partial\mathscr{D}\end{aligned} \tag{3.26}$$

to $O(D_1/D_2)$.

A detailed analysis of the forced system (3.18), (3.19) is beyond the scope of this paper. In §6 we shall use the relations (3.16) and (3.17) to obtain estimates of ζ_0 and U for a τ_0 scale derived from wind data at the Lake of Lugano. Since these estimates for the interfacial displacement and current compare favourably with the observed amplitudes, we conclude that (3.18) and (3.19) are an accurate characterization of the low-frequency fluctuations of stratified intermontane lakes.

4. Barotropic solution for elliptical topographic waves

(a) *Analytical solution*

As a first step toward solving the forced system (3.18), (3.19) we need the free topographic wave solutions for a specific lake geometry. Here we give a brief review of the recently derived (Mysak 1985) topographic wave modes for the elliptically shaped lake illustrated in figure 2. We assume that the shoreline and depth contours of the lake form a *family of confocal ellipses* with foci at $x = \pm a$. In terms of the elliptic cylinder coordinates (ξ, η) defined by (see also figure 3)

$$\left.\begin{aligned} x &= a\cosh\xi\cos\eta, \quad 0 < \xi < \infty, \\ y &= a\sinh\xi\sin\eta, \quad 0 < \eta < 2\pi, \end{aligned}\right\} \tag{4.1}$$

the shoreline is denoted by the ellipse $\xi = \xi_s$ and the lake bottom along the main axis of the lake corresponds to the degenerate ellipse $\xi = 0$ $(y = 0, |x| \leqslant a)$. Elimination of η from (4.1) yields the family of ellipses

$$x^2/(a^2\cosh^2\xi) + y^2/(a^2\sinh^2\xi) = 1, \tag{4.2}$$

which are illustrated in figure 3. The orthogonal curves are the family of hyperbolas

$$x^2/(a^2\cos^2\eta) - y^2/(a^2\sin^2\eta) = 1, \tag{4.3}$$

which are also illustrated in figure 3. Since the shoreline $\xi = \xi_s$ has the equation $x^2 + y^2/R^2 = 1$ (see figure 2) it follows from (4.2) that

$$1 = a\cosh\xi_s, \quad R = a\sinh\xi_s \tag{4.4}$$

and hence that

$$R = \tanh\xi_s. \tag{4.5}$$

The relation between ξ_s and R (which equals W/L, where W and L are the dimensional semi-minor and semi-major lake axes respectively) is given in table 1 for various W, L pairs.

In terms of the (ξ, η) coordinates, (3.18) with $\boldsymbol{\tau} = \mathbf{0}$ reduces to

$$\frac{\partial}{\partial\xi}\left(\frac{1}{h}\frac{\partial^2\psi}{\partial\xi\,\partial t}\right) + \frac{1}{h}\frac{\partial^3\psi}{\partial^2\eta\,\partial t} - \frac{\mathrm{d}}{\mathrm{d}\xi}\left(\frac{1}{h}\right)\frac{\partial\psi}{\partial\eta} = 0, \tag{4.6}$$

where $h = h(\xi)$ only because of our assumption about the distribution of the depth contours. Remarkably, (4.6) is independent of the scale factors h_ξ, h_η for elliptic coordinates, which are given by

$$h_\xi = h_\eta = aJ(\xi, \eta) = a(\sinh^2\xi + \sin^2\eta)^{\frac{1}{2}}. \tag{4.7}$$

(Here, the scale factors h_ξ, h_η arising in (4.7) and (4.9) (and also in (5.7)) should not be confused with derivatives of h. They arise nowhere else in this paper, which is why we maintain the common notation.) Therefore, we can readily find separable solutions of (4.6) of the form

$$\psi = \psi_{mn}(\xi, \eta, t) = F_n(\xi)\,\mathrm{e}^{\mathrm{i}(m\eta - \sigma t)}, \tag{4.8}$$

where $m = 1, 2, \ldots$ is the azimuthal mode number and $n = 1, 2, \ldots$ is the radial mode number. Equation (4.8) represents an elliptically travelling wave whose phase moves along the ellipse $\xi = \xi_0$ with speed

$$c_p = \left.\frac{\mathrm{d}s}{\mathrm{d}t}\right|_{\xi=\xi_0} = h_\eta(\xi_0, \eta)\frac{\mathrm{d}\eta}{\mathrm{d}t} = a(\sinh^2\xi_0 + \sin^2\eta)^{\frac{1}{2}}\frac{\sigma}{m}. \tag{4.9}$$

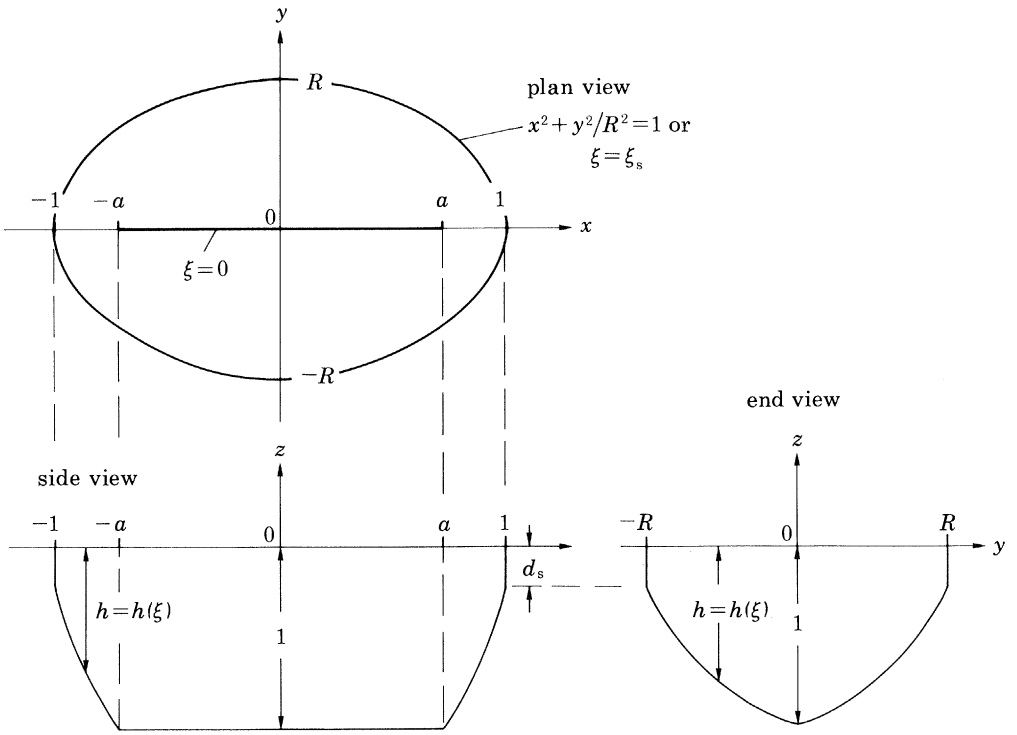

FIGURE 2. Elliptical lake model in terms of non-dimensional coordinates (x, y, z). The horizontal and vertical coordinates have been scaled by L and D respectively. Therefore, $d_s = D_s/D$ and $a = l/L$ (see figure 1). Also, $R = W/L$, where $2W$ is the dimensional width of the lake. The loci ξ = constant represent a family of confocal ellipses, with foci at $x = \pm a$. (From Mysak 1985.)

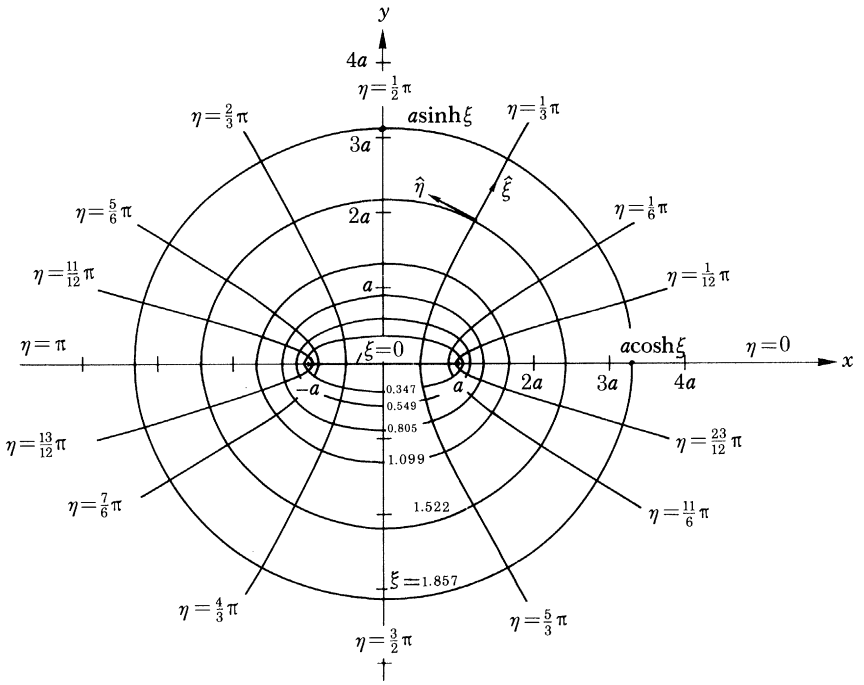

FIGURE 3. Elliptic cylinder coordinates (ξ, η). The parameters $\hat{\boldsymbol{\xi}}$ and $\hat{\boldsymbol{\eta}}$ are unit vectors in the directions of increasing ξ and η. We refer to ξ and η as radial and angular coordinates respectively.

PHILOSOPHICAL TRANSACTIONS OF THE ROYAL SOCIETY A MATHEMATICAL, PHYSICAL & ENGINEERING SCIENCES

TABLE 1. NUMERICAL RELATIONS BETWEEN W, L, R, ξ_s AND a

W/L	R (W/L)	ξ_s (artanh R)	a $(1/\cosh \xi_s)$
$1/\infty$	0	0	1
1/10	0.100	0.100	0.995
1/5	0.200	0.203	0.980
1/3	0.333	0.347	0.943
1/2	0.500	0.549	0.866
1/1.5	0.667	0.805	0.745
1/1.25	0.800	1.099	0.600
1/1.10	0.909	1.522	0.417
1/1	1	∞	0

Note that c_p varies with η, the angular coordinate! For $\xi_0 \gg 1$ (a 'circular' ellipse) $\sinh^2 \xi_0 \gg \sin^2 \eta$, and $c_p \approx$ constant for all η, as for a circularly travelling wave.

Substitution of (4.8) into (4.6) yields

$$(h^{-1}F_n')' + [m\sigma^{-1}(h^{-1})' - m^2 h^{-1}]\, F_n(\xi) = 0, \quad 0 < \xi < \xi_s. \tag{4.10}$$

At the outer boundary $\xi = \xi_s$, $\psi = 0$ (see equation (3.25)); hence from (4.8)

$$F_n(\xi_s) = 0. \tag{4.11}$$

As pointed out in Mysak (1985), there is no obvious boundary condition that can be applied at $\xi = 0$ to close the two-point boundary value problem for the radial eigenfunction $F_n(\xi)$ and corresponding eigenvalue σ^{-1}. However, if we put $\psi = \psi(\xi, \eta)\, e^{-i\sigma t}$ into (4.6) and (3.25), recast the resulting boundary value problem for $\psi(\xi, \eta)$ as a variational principle, and then invoke periodicity with respect to $\eta (\psi \propto e^{im\eta})$, we find that the solution of the problem (4.10) and (4.11) is equivalent to finding all functions $G(\xi)$ that satisfy (4.11) and then minimizing the functional (see equation (8.4) in Mysak (1985)):

$$I(G) = \int_0^{\xi_s} h^{-1}(G'^2 + m^2 G^2)\, d\xi - m\sigma^{-1} \int_0^{\xi_s} (h^{-1})' G^2\, d\xi. \tag{4.12}$$

In practice, once a specific depth profile $h(\xi)$ has been chosen, we substitute into (4.12) a trial function satisfying (4.11) and containing a set of parameters α_j and then minimize I by solving the equations $\partial I/\partial \alpha_j = 0$ for the α_j. The resulting trial function is then an approximation to F, which appears as the amplitude in the waveform (4.8). Also, minimization with respect to one of the α_js yields the (approximate) eigenfrequency relation. This procedure is known as the Rayleigh–Ritz method. Also, the *barotropic* velocity components along $\hat{\boldsymbol{\xi}}$ and $\hat{\boldsymbol{\eta}}$ (see figure 3) can be determined by using the relations

$$u_\xi = -\frac{1}{haJ}\frac{\partial \psi}{\partial \eta}, \quad u_\eta = \frac{1}{haJ}\frac{\partial \psi}{\partial \xi}. \tag{4.13}$$

We refer to u_ξ and u_η as the 'cross-isobath' and 'alongshore components', respectively.

If G is a true eigenfunction F with eigenvalue σ^{-1}, then $I(F) \equiv 0$, which yields the Rayleigh quotient

$$\frac{m}{\sigma} = \int_0^{\xi_s} h^{-1}(F'^2 + m^2 F^2)\, d\xi \Big/ \int_0^{\xi_s} (h^{-1})' F^2\, d\xi. \tag{4.14}$$

Equation (4.14) shows that $m/\sigma > 0$ provided $(h^{-1})' > 0$ on average (which is true for most lakes). Thus (4.9) implies that $c_p > 0$ and hence the waves travel anticlockwise around the lake, with the shoreline (shallow water) on the right. In the southern hemisphere the time scale $f^{-1} < 0$ and the waves travel clockwise around the lake.

For the exponential depth profile

$$h = e^{-b\xi}, \quad b > 0, \tag{4.15}$$

which is well known in shelf wave theory (see Buchwald & Adams 1968), a trial function that minimizes the functional (4.12) can be written in the form (for details, see Mysak 1985)

$$G(\xi) = (-1)^n e^{-\frac{1}{2}b\xi} \sin \alpha_n(\xi - \xi_s), \tag{4.16a}$$

where α_n is the nth root of

$$\alpha + \tfrac{1}{4}[1 - \alpha^{-2}(\lambda - A)]\,\xi_s^{-1} \sin 2\alpha\xi_s + \tfrac{1}{2}[\alpha + \alpha^{-1}(\lambda - A)] \cos 2\alpha\xi_s + \tfrac{1}{2}b \sin 2\alpha\xi_s = 0 \tag{4.16b}$$

in which $\lambda - A$ is given by

$$\lambda - A = \frac{\frac{1}{2}\xi_s\,\alpha^2 + \frac{1}{4}\alpha \sin 2\alpha\xi_s + \frac{1}{2}b \sin^2 \alpha\xi_s}{\frac{1}{2}\xi_s - \frac{1}{4}\alpha^{-1} \sin 2\alpha\xi_s}. \tag{4.16c}$$

In (4.16c), $\lambda = mb/\sigma$ and $A = m^2 + \frac{1}{4}b^2$, so that (4.16c) is effectively the eigenfrequency relation for the problem. However, the eigenfrequencies $\sigma = \sigma_{mn}$ have to be determined numerically by first solving (4.16b) for the roots $\alpha = \alpha_n$, and then substituting these values into (4.16c). Note that α depends only on b and ξ_s, and thus is independent of m, the azimuthal mode number.

In practice it is convenient to let

$$\alpha = \alpha_n = n\pi(1 + \delta_n)/\xi_s \tag{4.17}$$

and solve (4.16b) for δ_n. When $\delta_n = 0$, (4.16a) and (4.16c) reduce to

$$G = e^{-\frac{1}{2}b\xi} \sin (n\pi\xi/\xi_s),$$

$$\frac{1}{\sigma_{mn}} = \frac{1}{mb}\left[m^2 + \frac{b^2}{4} + \left(\frac{n\pi}{\xi_s}\right)^2\right],$$

which are the *exact* eigenfunctions and eigenfrequencies for a lake with a vertical barrier (a 'narrow' island) along the degenerate ellipse $\xi = 0$ (Mysak 1985). For this 'barrier' solution it is clear that there is no cross-isobath flow at the centreline $\xi = 0$ and that $\sigma/m > 0$; the latter result being in accordance with (4.14). Exterior to a thin elliptically shaped region surrounding the barrier at $\xi = 0$, the 'barrier' eigenfunctions are qualitatively similar to those given by (4.16a). Also, for b and ξ_s of order unity, a 'barrier' eigenfrequency σ_{mn} is roughly 30–40 % lower than the corresponding non-barrier eigenfrequency given by (4.16c) (see Mysak (1985) for further details).

Using (4.16a) in (4.8), the real form of ψ is found to be

$$\psi_{mn} = (-1)^n e^{-\frac{1}{2}b\xi} \sin [n\pi(1 + \delta_n)\,(\xi - \xi_s)/\xi_s] \cos (m\eta - \sigma_{mn}\,t). \tag{4.18}$$

Substituting (4.18) into (4.13) we obtain the corresponding velocity field

$$u_\xi = (-1)^n\,(m/aJ)\,e^{\frac{1}{2}b\xi} \sin [n\pi(1 + \delta_n)\,(\xi - \xi_s)/\xi_s] \sin (m\eta - \sigma_{mn}\,t), \tag{4.19}$$

$$u_\eta = (-1)^n\,(1/aJ)\,e^{\frac{1}{2}b\xi}\{-\tfrac{1}{2}b \sin [n\pi(1 + \delta_n)\,(\xi - \xi_s)/\xi_s] + [n\pi(1 + \delta_n)/\xi_s] \cos [n\pi(1 + \delta_n)\,(\xi - \xi_s)/\xi_s]\} \cos (m\eta - \sigma_{mn}\,t), \tag{4.20}$$

PHILOSOPHICAL TRANSACTIONS OF THE ROYAL SOCIETY A MATHEMATICAL, PHYSICAL & ENGINEERING SCIENCES

which show that u_ξ and u_η are respectively in quadrature and in phase with ψ. Contours of ψ_{mn} and the corresponding velocity profiles are illustrated in §4*b*.

Although the exponential depth profile (4.15) is not too realistic for some lakes (it has the wrong curvature), the analytical simplicity of the solution enables us to proceed with ease to an analysis of the motions in a stratified lake.

(*b*) *Numerical examples*

To illustrate the analytical solution for the exponential depth profile (4.15), we compute, for the first few modes, the periods, streamline patterns and associated velocity fields for a model elliptic lake with shoreline $\xi_s = 0.805$, corresponding to $W/L = 1/1.5$ and $a = 0.745$ (see table 1).

An important free parameter in our model is d_s, the non-dimensional depth at the edge of the lake (see figure 2). Since $0 < d_s < 1$, it is interesting to consider the limits $d_s \lesssim 1$ (weak topography) and $d_s \ll 1$ (strong topography). For the first, the bottom slope is relatively small, corresponding to a weak restoring force for topographic waves; thus the periods are generally very long (several weeks). For the second, the bottom slope (restoring force) is relatively large and the periods are much shorter. For most lakes, the second case applies. From (4.15), we find $d_s = e^{-b\xi_s}$, or

$$b = b(\xi_s, d_s) = (1/\xi_s) \ln (1/d_s). \tag{4.21}$$

Thus for fixed ξ_s, $b\downarrow$ as $d_s\uparrow$ but only logarithmically, so that weak topography corresponds to 'small' b, and strong topography, to 'large' b. As an example of strong topography, table 2 gives different modal periods for $b = 2.86$ ($d_s = 0.1$). Note that the lower modes have periods of a few days, which is characteristic of the Lugano and Zurich lake observations.

TABLE 2. THE PERIODS $T_{mn} = 2\pi/\sigma_{mn} f$ (IN DAYS), WITH $f = 1.05 \times 10^{-4}$ s^{-1} (46° N), $\xi_s = 0.805$ AND $b = 2.86$ ($d_s = 0.1$)

(The term σ_{mn} is given by (4.16*c*). The last line gives the first five values of δ_n (see equation (4.17)), which satisfy (4.16*b*) and which are subsequently used in (4.16*c*).)

$m\backslash n$ ...	1	2	3	4	5
1	2.35	9.86	24.64	46.77	76.28
2	1.54	5.29	12.68	23.75	38.50
3	1.43	3.93	8.86	16.24	26.07
4	1.50	3.37	7.07	12.60	19.98
5	1.63	3.13	6.09	10.52	16.42
δ_n	−0.339	−0.214	−0.152	−0.117	−0.095

At a fixed latitude, (4.16*c*) and (4.21) imply that the period $T_{mn} = 2\pi/f\sigma_{mn}$ is a function of the two independent parameters ξ_s and d_s. In Ball's (1965) solution for an elliptic paraboloid, the only free parameter in T_{mn} is $R = W/L$, or equivalently, ξ_s. Comparison of T_{mn} for the two models shows that, in general, the periods are comparable for d_s in the range 0.1–0.2 in the model (4.15) (see Mysak 1985 for further details).

Figure 4 shows the time evolution of the contours of ψ_{11} as given by (4.18) through one quarter of the wave period. The double cell structure of this mode seen in figure 4 is reminiscent of the pattern that also arises in Ball's (1965) fundamental mode for an elliptic paraboloid (see

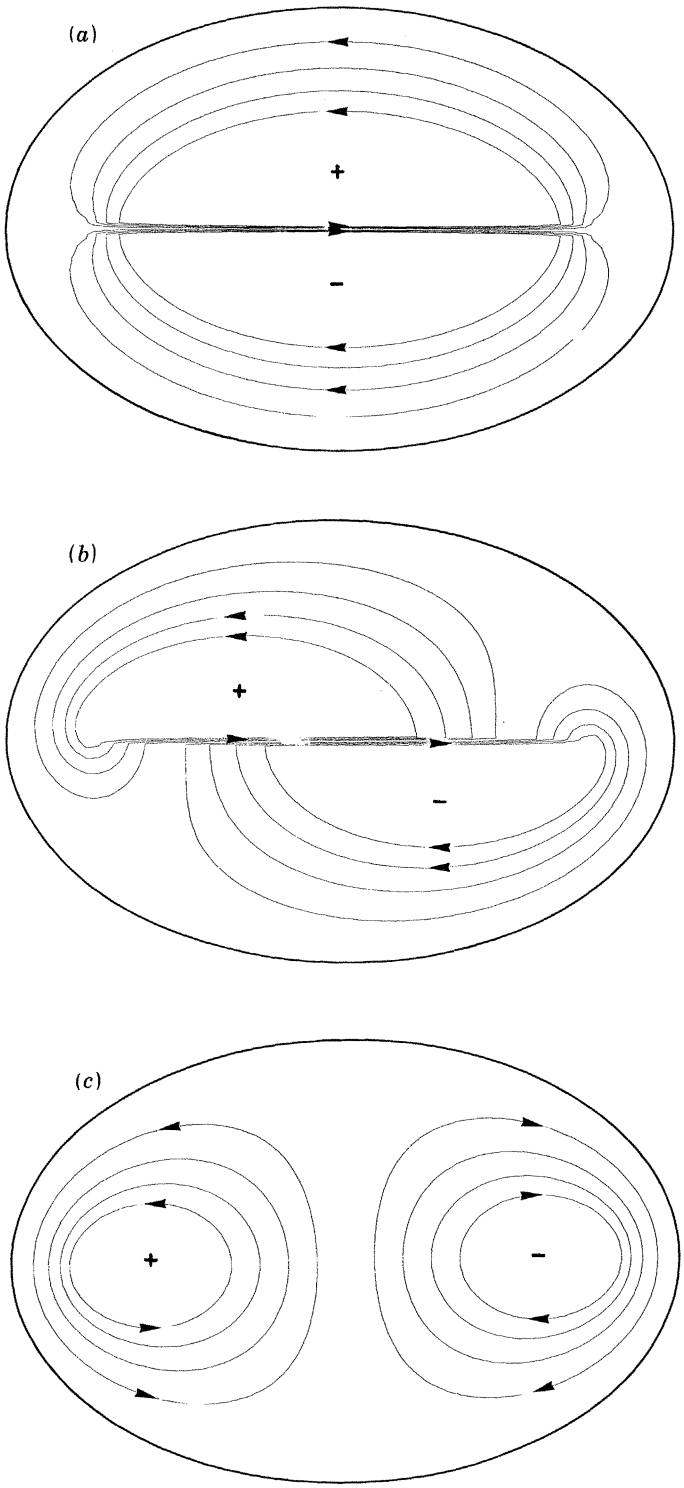

FIGURE 4. Contours of the stream function ψ_{11} with $b = 2.86$ ($d_s = 0.1$) and $\xi_s = 0.805$ at (*a*) $\sigma_{11}\, t = -\frac{1}{2}\pi$, (*b*) $-\frac{1}{4}\pi$, (*c*) 0. (From Mysak 1985.)

PHILOSOPHICAL TRANSACTIONS OF THE ROYAL SOCIETY A MATHEMATICAL, PHYSICAL & ENGINEERING SCIENCES

for example, figure 12*a* in Saylor *et al.* 1980). Furthermore, both models show the variable angular speed of propagation of the cells anticlockwise around the lake, with the speed being largest at the top and bottom of the ellipse ($\eta = \frac{1}{2}\pi$ and $\frac{3}{2}\pi$). For the Mysak model this can be easily seen from (4.9), which implies that c_p is a maximum at $\eta = \frac{1}{2}\pi, \frac{3}{2}\pi$ and a minimum at $\eta = 0, \pi$.

Figure 5 shows the time evolution of the barotropic velocity $\boldsymbol{u}_{11}$, whose components are given by (4.19) and (4.20). Except near the foci at $x = \pm a$, the barotropic velocity field is largely

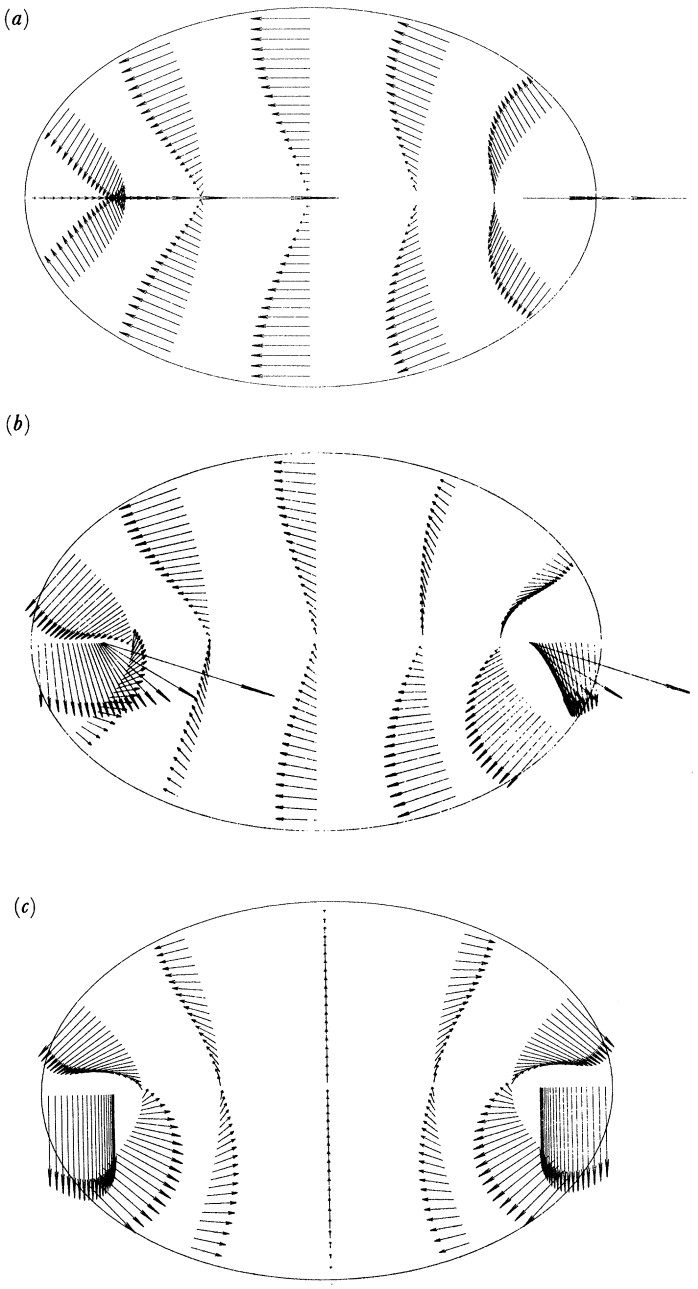

FIGURE 5. Arbitrarily scaled fundamental-mode barotropic velocity field $\boldsymbol{u}_{11}$ with $b = 2.86$ ($d_s = 0.1$), $\xi_s = 0.805$ and $a = 0.745$ are (*a*) $\sigma_{11} t = -\frac{1}{2}\pi$, (*b*) $-\frac{1}{4}\pi$, (*c*) 0.

PHILOSOPHICAL TRANSACTIONS OF THE ROYAL SOCIETY A MATHEMATICAL, PHYSICAL & ENGINEERING SCIENCES

along the shore ($u_\eta \gg u_\xi$) and the particle path about any fixed point is an elongated ellipse. In particular, we note that the motion is anticlockwise near the centre of the lake and clockwise near the sides. The large arrows emanating from near the foci in figures 5*b*, *c* are a somewhat artificial feature of the solution, and are due to the nature of elliptic cylinder coordinates. They arise because of the vanishing at $\xi = 0$ and $\eta = 0, \pi$ of the scale factor aJ, which appears in the denominator of u_ξ and u_η (see equations (4.19) and (4.20)).

Examples of the streamline patterns for the next two higher modes are illustrated in figure 6. As shown in Mysak (1985), these patterns also rotate anticlockwise around the basin as the waves propagate.

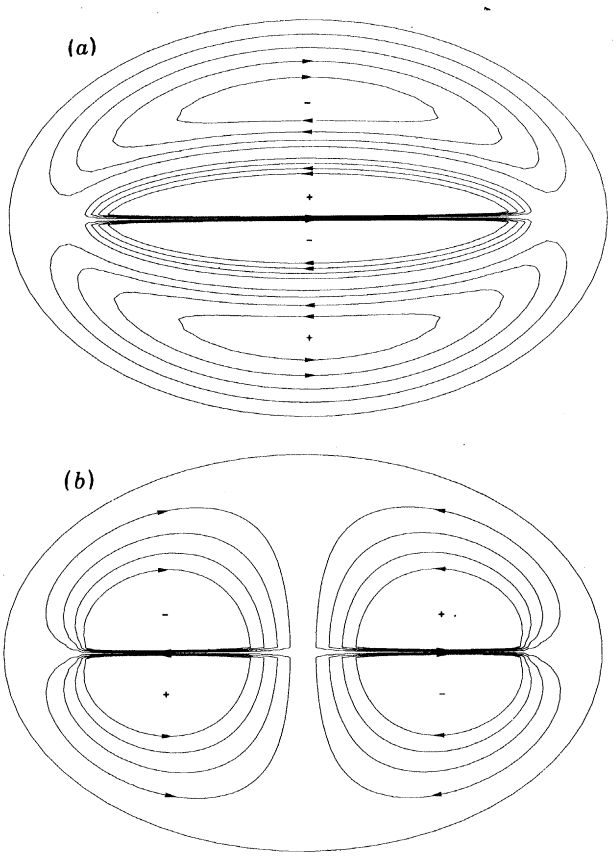

FIGURE 6. Contours of (*a*) ψ_{12} at $\sigma_{12}t = -\frac{1}{2}\pi$ and (*b*) ψ_{21} at $\sigma_{21}t = -\frac{1}{2}\pi$ with $b = 2.86$ ($d_s = 0.1$) and $\xi_s = 0.805$. (From Mysak 1985.)

5. BAROCLINIC PART OF ELLIPTICAL TOPOGRAPHIC WAVE SOLUTION

Having obtained the free wave solution for ψ in §4*a*, we can now proceed to (3.19) and (3.26) to find ζ, the interfacial displacement. The currents are then obtained from (3.23*a*) and (3.23*b*). For convenience, we rewrite these equations here, setting $\boldsymbol{\tau} = \mathbf{0}$ where necessary. To find ζ we have to solve

$$(\nabla^2 - S^{-1})\,\zeta_t = -(\nabla\psi \times \nabla h^{-1})\cdot\hat{\boldsymbol{z}} \quad \text{in} \quad \xi < \xi_s, \tag{5.1}$$

subject to the boundary condition

$$\frac{\partial^2\zeta}{\partial n\,\partial t}-\frac{\partial\zeta}{\partial s}=0 \quad \text{on} \quad \xi=\xi_s. \tag{5.2}$$

The currents in each layer are then given by

$$\boldsymbol{u}_1 = h^{-1}[\hat{\boldsymbol{z}}\times\nabla\psi + h(\nabla\zeta_t - \hat{\boldsymbol{z}}\times\nabla\zeta)], \tag{5.3}$$

$$\boldsymbol{u}_2 = h^{-1}\hat{\boldsymbol{z}}\times\nabla\psi. \tag{5.4}$$

For a given wave mode ψ_{mn}, equation (5.1) takes the form of a forced modified Helmholtz equation after integrating with respect to t. This equation could be solved by using the relevant Green function, or by an appropriate eigenfunction expansion. In either case, Mathieu and modified Mathieu functions would be involved. Since these special functions are not very well known to most limnologists, it is desirable to find another approach for obtaining ζ. This is outlined in §5*a*.

(*a*) *Geometrical optics approximation*

For many intermontane lakes (including the Lake of Lugano and the Lake of Zurich), the inverse stratification parameter S^{-1} is fairly large, namely

$$S^{-1} = O(5\text{–}10). \tag{5.5}$$

Therefore $S^{-1} \gg \nabla^2 = O(1)$, and the dominant term on the left side of (5.1) is $-S^{-1}\zeta_t$. Because the left side of (5.1) has the form of a modified Helmholtz equation with S^{-1} as the large 'wavenumber', the simplification

$$S^{-1}\zeta_t = (\nabla\psi\times\nabla h^{-1})\cdot\hat{\boldsymbol{z}} \tag{5.6}$$

can be described as a geometrical optics approximation for ζ. With $h = h(\xi)$, (5.6) reduces to

$$\zeta_t = -\frac{S}{h_\xi h_\eta}\frac{\partial\psi}{\partial\eta}\frac{\mathrm{d}}{\mathrm{d}\xi}\left(\frac{1}{h}\right), \tag{5.7}$$

which implies that along the shore

$$\zeta(\xi_s, \eta, t) = 0 \tag{5.8}$$

since $\psi(\xi_s, \eta, t) = 0$. This is consistent with the boundary condition (5.2) provided we neglect the 'small' $\partial^2\zeta/\partial n\,\partial t$ term; this can be done since $\partial_t \sim \sigma = O(10^{-1})$ for the low-frequency topographic waves under consideration. Therefore, (5.2) can be approximated by $\partial\zeta/\partial s = \partial\zeta/\partial\eta = 0$, or equivalently, $\zeta(\xi_s, \eta, t) = 0$. Further support for our geometrical optics approximation (5.7) comes from Gratton (1983), who solved the complete system (5.1) and (5.2) for low-frequency waves in a channel with strong topography. In several numerical examples, his solution for ζ has a very small amplitude at the boundary, typically 10–20% of the maximum value near the channel centre. Moreover, the lower the frequency, the closer ζ is to zero, which is consistent with our 'low-frequency' approximation of the boundary condition (5.2).

Since $S \propto r_i^2 \propto g'$ (see (3.20) and the line following (3.9)), $S^{-1}\uparrow$ as $g'\downarrow$; thus the geometrical optics approximation (5.6) improves with weakening stratification. Also, from (5.7) we note that ζ is small for weak stratification ($S \ll 1$) and vanishes when $S = 0$ (homogeneous fluid).

PHILOSOPHICAL TRANSACTIONS OF THE ROYAL SOCIETY A MATHEMATICAL, PHYSICAL & ENGINEERING SCIENCES

Thus in this limit only barotropic topographic waves exist, being manifested in the horizontal current field given by (4.19) and (4.20).

For the exponential depth profile solution (4.18), (5.7) gives

$$\zeta_{mn} = \frac{\lambda_{mn} S(-1)^n}{a^2 J^2} \mathrm{e}^{\frac{1}{2}b\xi} \sin\left[n\pi(1+\delta_n)\,(\xi-\xi_s)/\xi_s\right] \cos\left(m\eta-\sigma_{mn}\,t\right), \tag{5.9}$$

where $\lambda_{mn} = mb/\sigma_{mn}$ is given by (4.16c) in which α has the form (4.17). Note that ζ_{mn} has the same phase and radial nodes as ψ_{mn}. However, since $J^2 = \sinh^2\xi + \sin^2\eta$, ζ_{mn} has a singularity at $\xi = 0$ and $\eta = 0$ or π, i.e. at the foci. Therefore we might expect to observe large thermocline displacements near these points in a lake.

The lower layer current $\boldsymbol{u}_2$ is barotropic to $O(D_1/D_2)$ (see equation (5.4)) and hence no further calculation is required: the components of $\boldsymbol{u}_2$ are given by (4.19) and (4.20). To find the upper layer current $\boldsymbol{u}_1$ we use (5.3) with the low-frequency term $\nabla\zeta_t$ neglected. This approximation is necessary to be consistent with the geometrical optics solution (5.7). Thus we have, approximately,

$$\begin{aligned} \boldsymbol{u}_1 &= h^{-1}\hat{\boldsymbol{z}}\times\nabla\psi - \hat{\boldsymbol{z}}\times\nabla\zeta \\ &\equiv \boldsymbol{u}^{\mathrm{bt}} + \boldsymbol{u}^{\mathrm{bc}}, \end{aligned} \tag{5.10}$$

which reveals that ζ behaves like a stream function for the baroclinic part of the upper layer current. Using (5.9) in the expression for $\boldsymbol{u}^{\mathrm{bc}}$ defined in (5.10), we find

$$\begin{aligned} u_\xi^{\mathrm{bc}} = &-\left[\lambda_{mn} S(-1)^n/a^3J^3\right] \mathrm{e}^{\frac{1}{2}b\xi} \sin\left[n\pi(1+\delta_n)\,(\xi-\xi_s)/\xi_s\right] \\ &\times\left[m\sin\left(m\eta-\sigma_{mn}\,t\right) + (1/J^2)\cos\left(m\eta-\sigma_{mn}\,t\right)\sin\left(2\eta\right)\right], \end{aligned} \tag{5.11}$$

$$\begin{aligned} u_\eta^{\mathrm{bc}} = &-\left[\lambda_{mn} S(-1)^n/a^3J^3\right] \mathrm{e}^{\frac{1}{2}b\xi} \cos\left(m\eta-\sigma_{mn}\,t\right) \times\{\tfrac{1}{2}b \sin\left[n\pi(1+\delta_n)\,(\xi-\xi_s)/\xi_s\right] \\ &+\left[n\pi(1+\delta_n)/\xi_s\right]\cos\left[n\pi(1+\delta_n)\,(\xi-\xi_s)/\xi_s\right] - (1/J^2)\sin\left[n\pi(1+\delta_n)\,(\xi-\xi_s)/\xi_s\right]\sinh\left(2\xi\right)\}, \end{aligned} \tag{5.12}$$

where λ_{mn} is given by (4.16c). Comparison of (5.11) and (5.12) with the barotropic components (4.19) and (4.20) shows that

$$u^{\mathrm{bc}}/u^{\mathrm{bt}} \approx 1/J^2 \tag{5.13}$$

for each component, and hence that near the foci where J^2 is small, the baroclinic currents will dominate. From the numerical calculations in §5b we shall see that this property also applies in other parts of the lake.

(*b*) *Numerical examples*

Figure 7 shows a bird's-eye view of the time evolution, through half a wave period, of the interfacial displacement ζ_{11} as given by (5.9). We have taken a value of S that applies to the Lake of Lugano, but since S is merely a multiplicative factor (see equation (5.9)) its value does not affect the interfacial patterns seen in figure 7. Since ζ is in phase with ψ (see equations (5.9) and 4.18)), the anticlockwise propagation of the highs and lows of ζ_{11} in figure 7 are analogous to the anticlockwise propagation of the cells seen in figure 4. However, because of the factor $1/J^2$ (see equation (5.9)), large displacements occur at certain times near the foci of the lake (see, for example, figure 7b–d).

Figure 8 shows the time evolution of the baroclinic part of the upper layer current associated

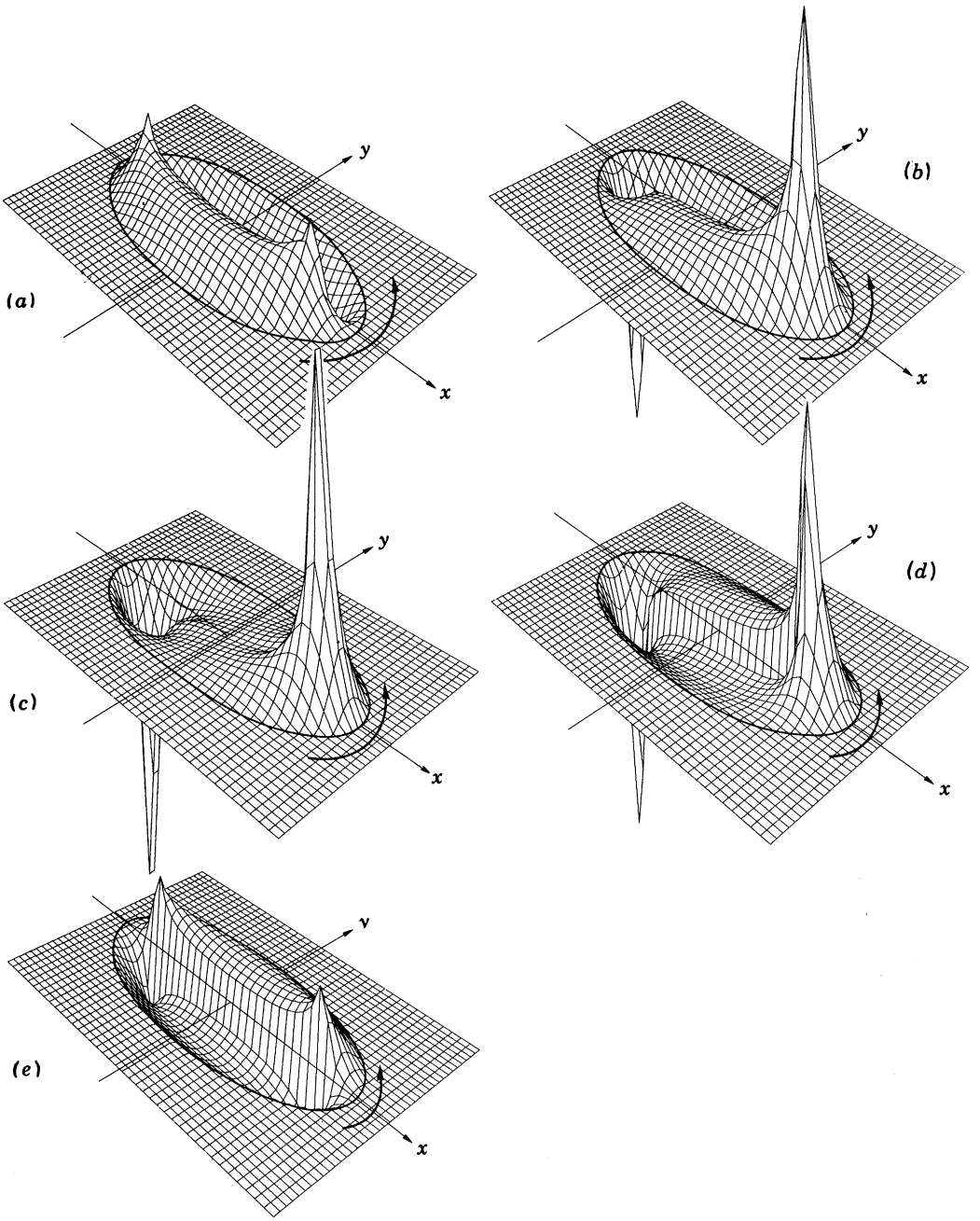

FIGURE 7. Evolution of interfacial displacement ζ_{11} with $b = 2.86$, $\xi_s = 0.805$, $a = 0.745$ and $S = 0.22$ for (*a*) $\sigma_{11}\, t = -\frac{1}{2}\pi$, (*b*) $-\frac{1}{4}\pi$, (*c*) 0, (*d*) $\frac{1}{4}\pi$, (*e*) $\frac{1}{2}\pi$.

with the fundamental mode. The components of $\boldsymbol{u}^{bc}$ are given by (5.11) and (5.12) with $m = n = 1$. The flow pattern at each instant of time in figure 8 is similar to the flow at the corresponding instants in figure 5, which give the time evolution of the barotropic part of the fundamental mode current. However, the currents are approximately 180° out of phase. Furthermore, it is interesting to note that near the lake centre and sides, the baroclinic current vectors rotate anticlockwise and clockwise respectively. Another important feature of figure 8

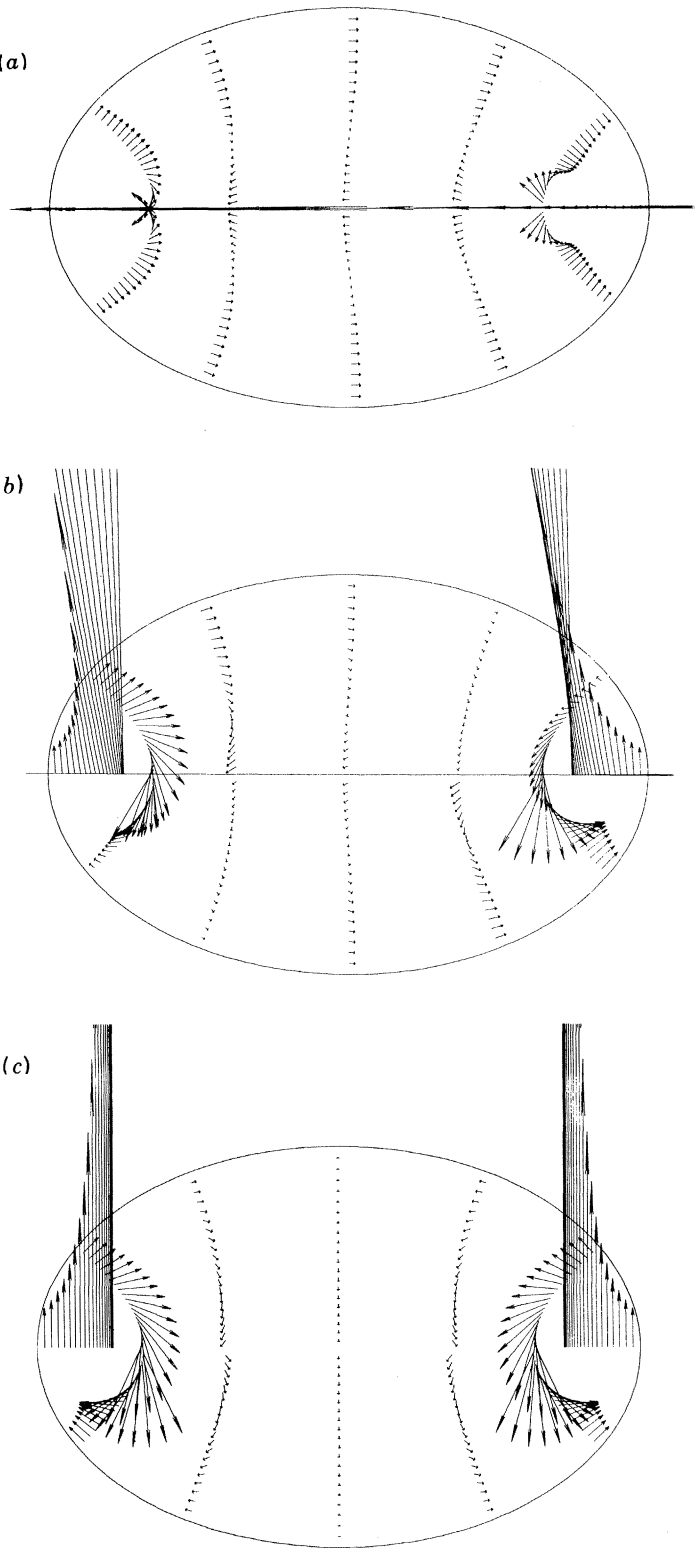

FIGURE 8. Evolution of fundamental-mode, upper-layer baroclinic current, $\boldsymbol{u}^{\mathrm{bc}}$, with S, b, ξ_{s} and a as in figure 7 for (*a*) $\sigma_{11}\, t = -\frac{1}{2}\pi$, (*b*) $-\frac{1}{4}\pi$, (*c*) 0. To compare vector magnitudes with those in figure 5, multiply the baroclinic vector here by 25.

PHILOSOPHICAL TRANSACTIONS OF THE ROYAL SOCIETY A MATHEMATICAL, PHYSICAL & ENGINEERING SCIENCES

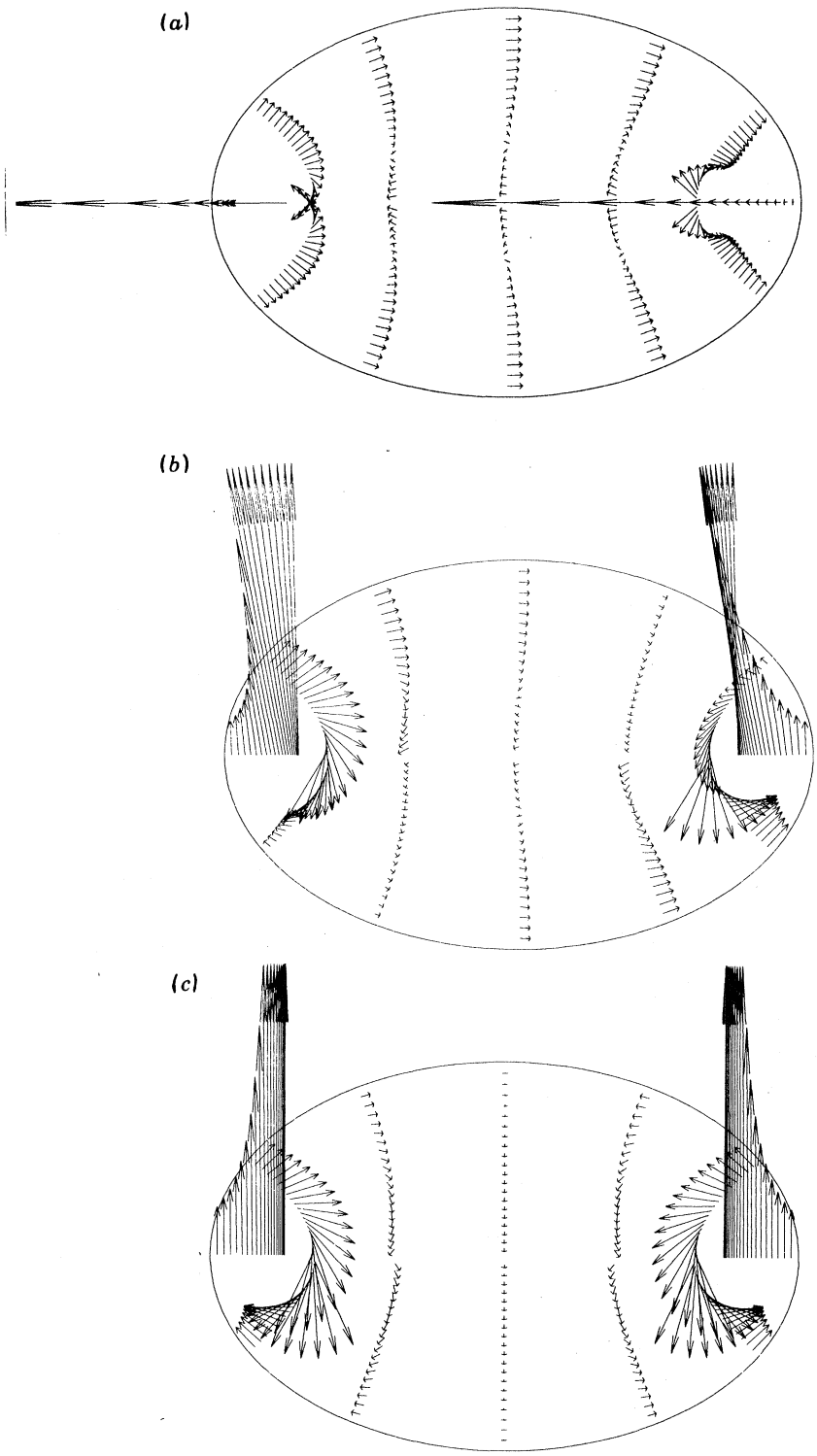

FIGURE 9. Evolution of fundamental-mode, upper layer total current $\boldsymbol{u}_1$ as given by (5.10) with $m = n = 1$ for (*a*) $\sigma_{11}\, t = -\frac{1}{2}\pi$, (*b*) $-\frac{1}{4}\pi$, (*c*) 0. The parameters S, b, ξ_s and a are the same as in figure 8, but the current vectors must be divided by two before comparing with those of figure 8. In parts (*b*) and (*c*) the arrows have been truncated along $\eta = 0$ and $\eta = \pi$, near the ends of the ellipse.

PHILOSOPHICAL TRANSACTIONS OF THE ROYAL SOCIETY A MATHEMATICAL, PHYSICAL & ENGINEERING SCIENCES

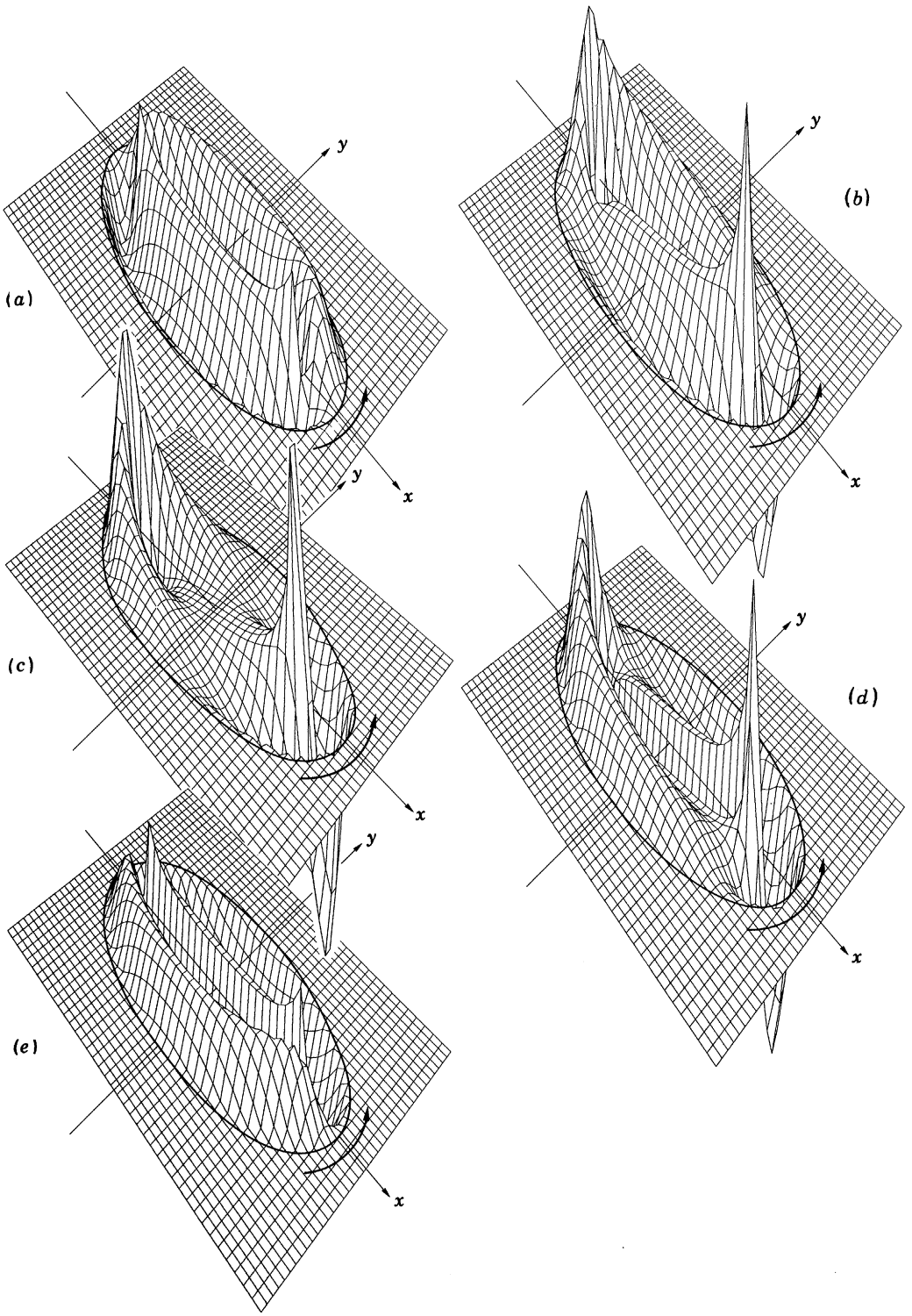

FIGURE 10. Evolution of interfacial displacement ζ_{12} with b, ξ_8, a and S as in figure 7 for (*a*) $\sigma_{12}t = -\frac{1}{2}\pi$, (*b*) $-\frac{1}{4}\pi$, (*c*) 0, (*d*) $\frac{1}{4}\pi$, (*e*) $\frac{1}{2}\pi$.

PHILOSOPHICAL TRANSACTIONS OF THE ROYAL SOCIETY A MATHEMATICAL, PHYSICAL & ENGINEERING SCIENCES

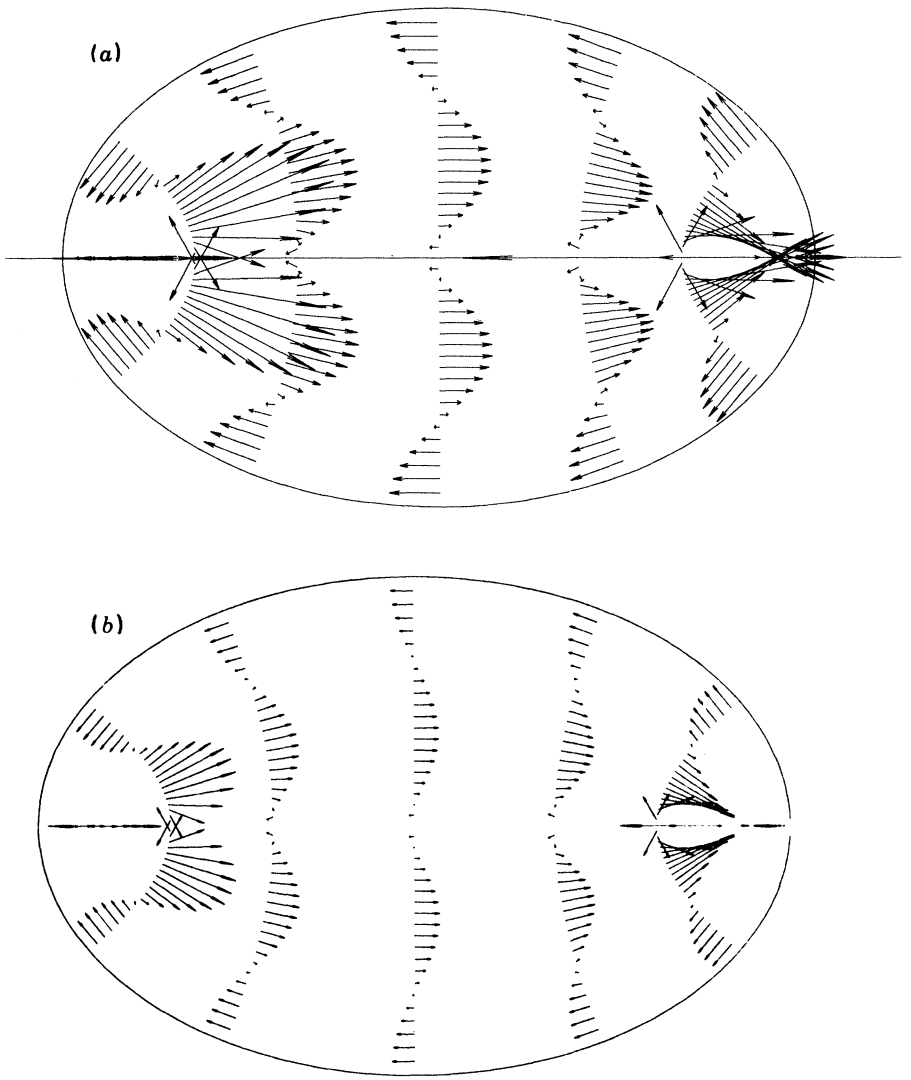

FIGURE 11. (*a*) Upper layer baroclinic current, $\boldsymbol{u}^{bc}$, for mode $m = 1$, $n = 2$ at $\sigma_{12}\, t = -\frac{1}{2}\pi$. The parameters S, b, ξ_s and a are the same as in figure 8. However, the current vectors have to be extended twice before comparing with those in figure 8. (*b*) Upper layer total current $\boldsymbol{u}_1$ as given by (5.10) for mode $m = 1$, $n = 2$ at $\sigma_{12}\, t = -\frac{1}{2}\pi$. The parameters are the same as in (*a*), but the current vectors must be multiplied with 1.25 before comparing with those of figure (*b*).

is that at each point the magnitude of the current is generally much larger than that of the barotropic current. For example, near the lake centre, the baroclinic currents are about ten times as large or more, whereas along the sides the factor is about four. Since the depth is relatively shallow near the sides, the increasing importance of the barotropic current is to be expected. The very large baroclinic currents in figure 8*b*, *c* along the line segments $\eta = 0$ and $\eta = \pi$ near the ends of the lake are due to the presence of the factor $1/J^2$ in each component (see equations (5.11) and (5.12)). The composite of figures 5 and 8 is shown in figure 9, which reveals that the barotropic part of the current reduces the flow quite noticeably along the shoreline. Nonetheless, the 180° phase shift and rotational properties described above for the baroclinic flow in figure 8 also apply to the total upper layer current in figure 9. Comparison

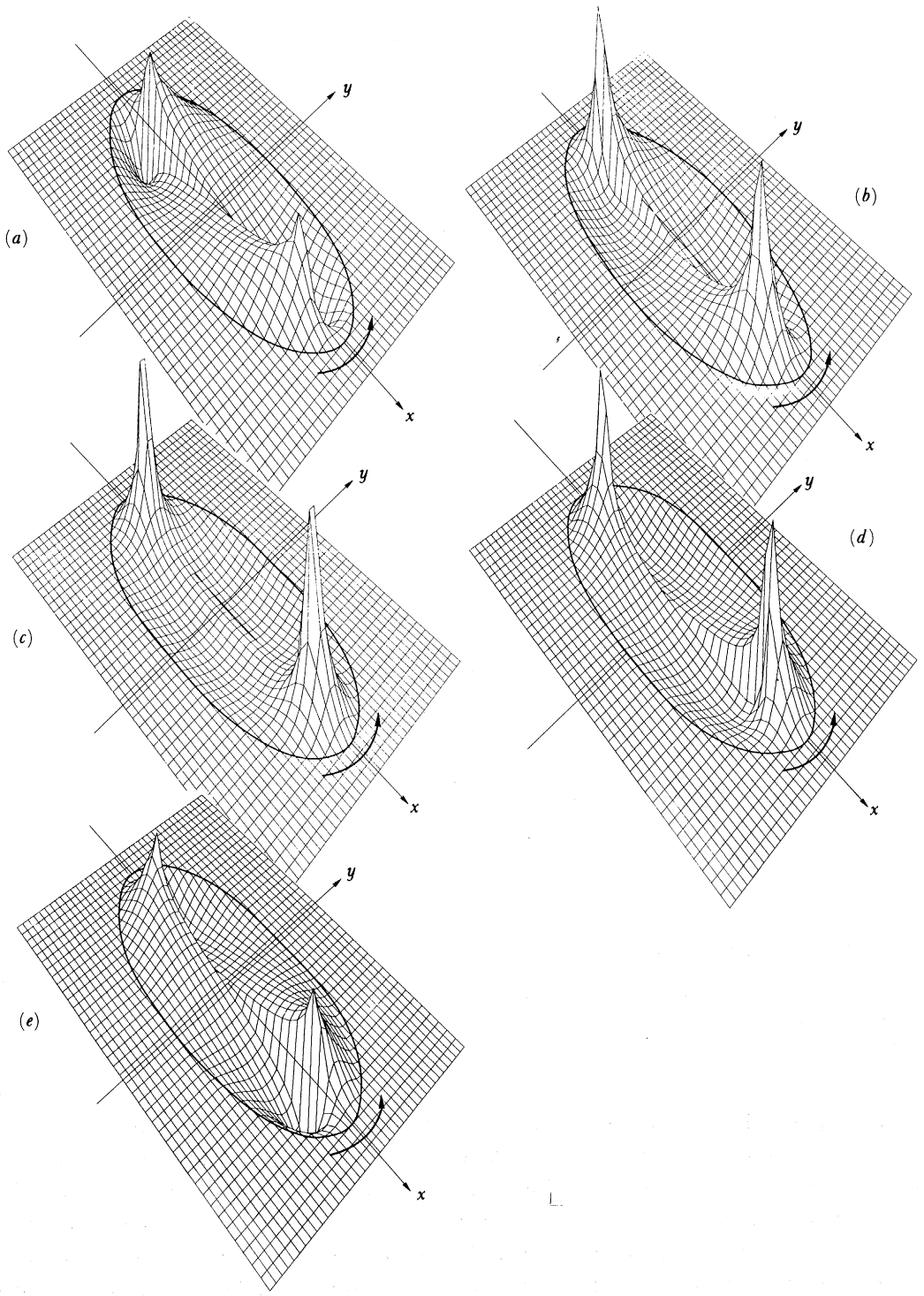

FIGURE 12. Evolution of the interfacial displacement ζ_{21} with b, ξ_S, a and S as in figure 7, for (*a*) $\sigma_{21}\, t = -\frac{1}{2}\pi$, (*b*) $-\frac{1}{4}\pi$, (*c*) 0, (*d*) $\frac{1}{4}\pi$, (*e*) $\frac{1}{2}\pi$.

PHILOSOPHICAL TRANSACTIONS OF THE ROYAL SOCIETY A MATHEMATICAL, PHYSICAL & ENGINEERING SCIENCES

of figure 7*b*, *c* for ζ_{11} with figure 9*b*, *c* shows that the large interfacial displacements near the lake ends go in tandem with large upper layer velocities.

Figure 10 shows the evolution of ζ_{12}, the first higher mode with a nodal ellipse in the interior. Comparison of figures 10*a* and 6*a* for ψ_{12} indicates that high (low) levels of ζ again correspond to clockwise (anticlockwise) circulation cells in ψ. Also, from the propagation of the interfacial patterns in figure 10*b*–*e* one can visualize the time sequels to ψ_{12} shown in figure 6*a*.

The upper layer baroclinic currents (figure 11*a*) associated with ζ_{12} are rather strong, being about one order of magnitude larger than $\boldsymbol{u}^{\mathrm{bc}}$ for the fundamental mode (figure 8*a*). But note that the baroclinic current is again about 180° out of phase with $\boldsymbol{u}^{\mathrm{bt}}$ for this mode (which can be deduced from figure 6*a*). This was also found to be the case for the fundamental mode. However, the barotropic component is very small for this mode, as attested by figure 11*b*, which shows that the total upper layer current is nearly the same as the baroclinic part (figure 11*a*).

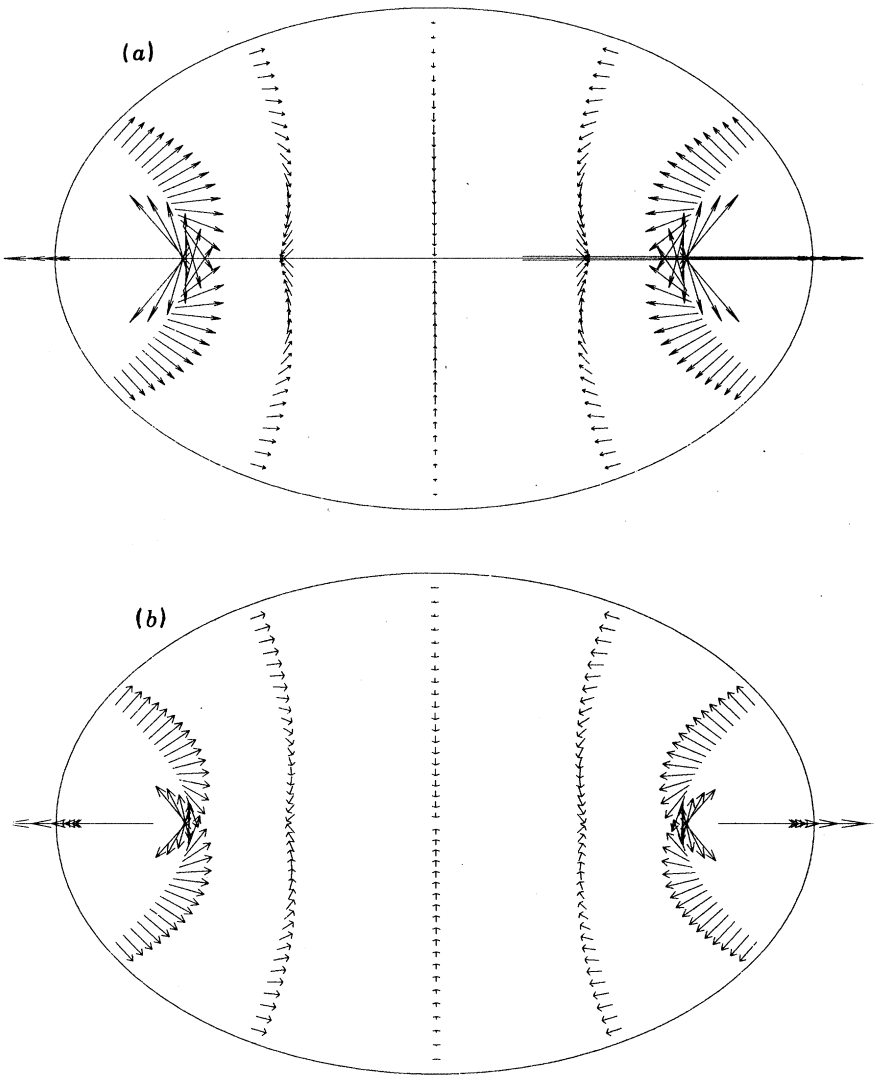

FIGURE 13. (*a*) Upper layer baroclinic current, $\boldsymbol{u}^{\mathrm{bc}}$, for mode $m = 2$, $n = 1$ at $\sigma_{21}\, t = -\frac{1}{2}\pi$. The current scale and parameters are the same as in figure 8. (*b*) Upper layer total current $\boldsymbol{u}_1$ as given by (5.10) for mode $m = 2$, $n = 1$ at $\sigma_{21}\, t = -\frac{1}{2}\pi$. The current scale and parameters are the same as in figure 9.

PHILOSOPHICAL TRANSACTIONS OF THE ROYAL SOCIETY A MATHEMATICAL, PHYSICAL & ENGINEERING SCIENCES

Finally, figure 12 shows the evolution of ζ_{21}, the first higher mode with two complete waves wrapped around the basin. The evolution patterns of ζ_{21} mimics, of course, that of ψ_{21}, which is shown only at $\sigma_{21}\, t = -\frac{1}{2}\pi$ in figure 6*b*. The associated upper layer velocity for this mode is also dominated by the baroclinic part (compare figure 13*a* with 13*b*), which is 180° out of phase with the barotropic part (see figure 6*b*).

6. Application to the Lake of Lugano

(*a*) *Field data and instrumentation*

The Lake of Lugano, located in the southern Swiss Alps, is made up of three separate basins. The north basin studied here is a narrow, extremely deep, L-shaped channel with a length of about 17 km, a mean width of about 1500 m and a mean depth of 175 m. The basin tends towards northeast and has very steep shores sloping down to a maximum depth of 288 m (see figure 14). Riverine-induced circulation is negligible for this basin (Hutter *et al.* 1983). Because the north basin is separated from one of the south basins by a dam, their dynamics can be studied independently.

To understand the lake's response to meteorological forcing, a threefold field programme was conducted from 3 July until 27 August 1979. Firstly, the mean spatial density distribution was determined by taking vertical temperature and conductivity profiles at isolated points, indicated by open circles in figure 14. Secondly, an intensive synoptic programme was made along a triangular course (indicated by solid circles in figure 14) in and immediately outside the bay of Lugano. Thirdly, current meters and thermistor chains that recorded every 20 minutes were deployed at seven mooring positions along the lake (see solid triangles in figure 14), and meteorological buoys were installed at three positions (indicated by solid squares in figure 14) near moorings 2, 4 and 8.

Temperature data from the positions marked with open circles in figure 14, collected in an internal report, indicate that stratification was fairly stagnant throughout the field programme despite varied meteorological forcing. (Misure idrologiche, lago di lugano, estate 1979. Joint report by Laboratorio di Fisica Terrestre, ICTS, Lugano Trevano and Laboratory of Hydraulics, Hydrology and Glaciology, ETH, Zurich (unpublished 1982).) The mean of all vertical temperature profiles is plotted in figure 15, which shows a warm and light top layer of about 10 m thickness that is separated from the relatively uniform hypolimnion at a temperature of less than 6 °C by a rather sharp thermocline transition. Also indicated in the figure is the two-layer approximation we shall use, consisting of a 10 m deep epilimnion at 21 °C and a very deep hypolimnion at 5.9 °C.

Originally it was intended to take current and temperature measurements in the epilimnion, the thermocline and the lower hypolimnion. However, because of inaccuracies in the available bathymetric charts, and furthermore because of the steep shores of the basin, depth estimation of moorings was inaccurate and all instruments were positioned at substantially lower depths. The highest current meter was at 15 m depth and thermistor chains covered the depth range from 17 to 68 m, recording temperatures from approximately 5 to 10 °C at most. Because (i) all current meter instruments came to lie in the upper hypolimnion and (ii) for most measurements current speeds are below the threshold of the instruments, currents were continuously recorded only at the mid-lake station 6 (near Gandria).

Wind data from the three meteorological buoys were collected between 9 July and 21 August,

PHILOSOPHICAL TRANSACTIONS OF THE ROYAL SOCIETY A MATHEMATICAL, PHYSICAL & ENGINEERING SCIENCES

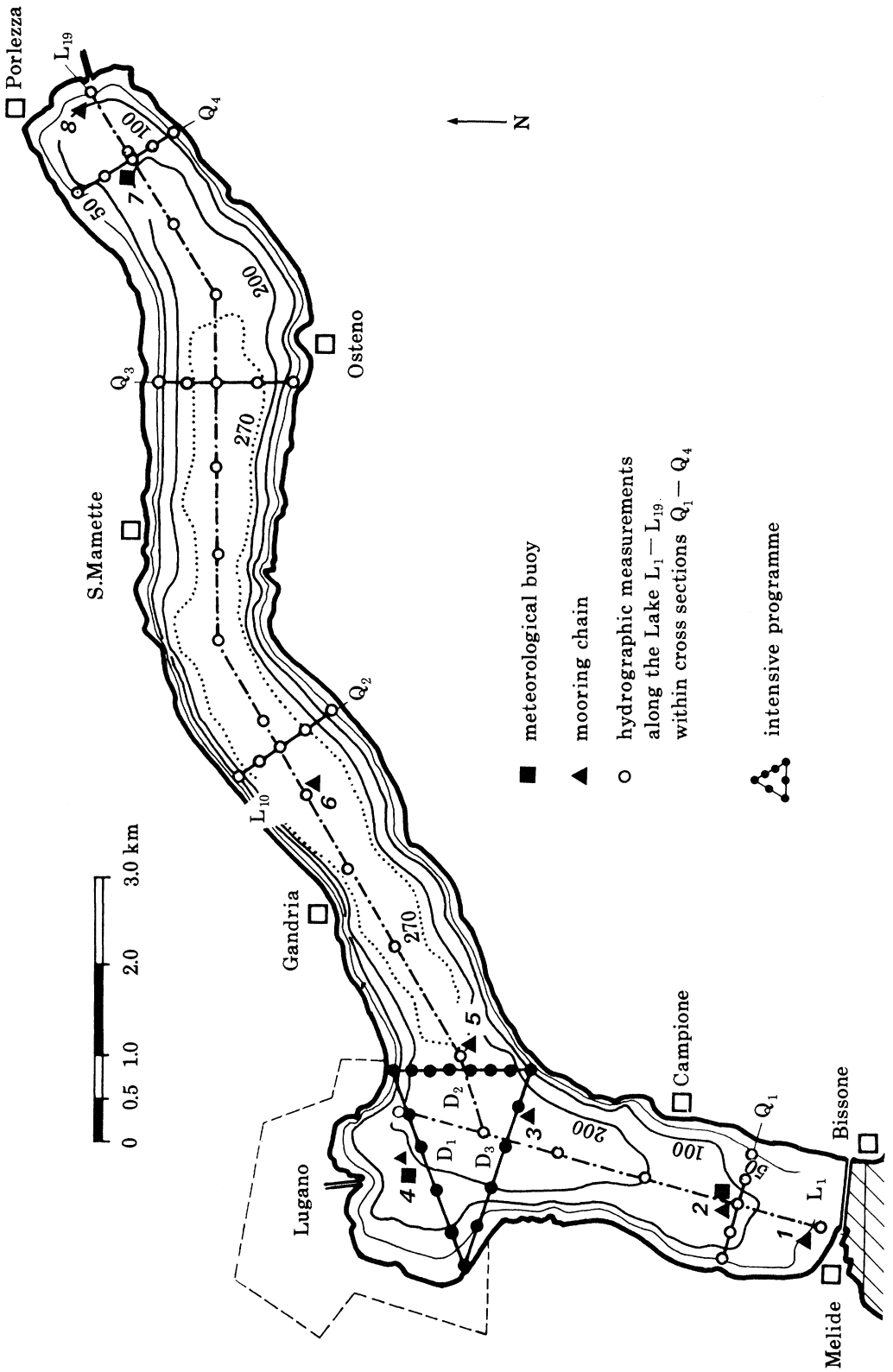

FIGURE 14. Topographic chart of the north basin of the Lake of Lugano with indications where hydrographic measurements were taken, where an intensive field programme was conducted and where thermistor chains, current meters and meteorological instruments were moored. Sloping numbers indicate moorings, with which we associate the following place names: Melide 1, Ferrera or Campione 2, Caprino 3, Cassarate 4, Gandria 6, Porlezza 7 and 8. Data were not available from mooring 5, which is therefore left unnamed. (From Hutter *et al.* 1983.)

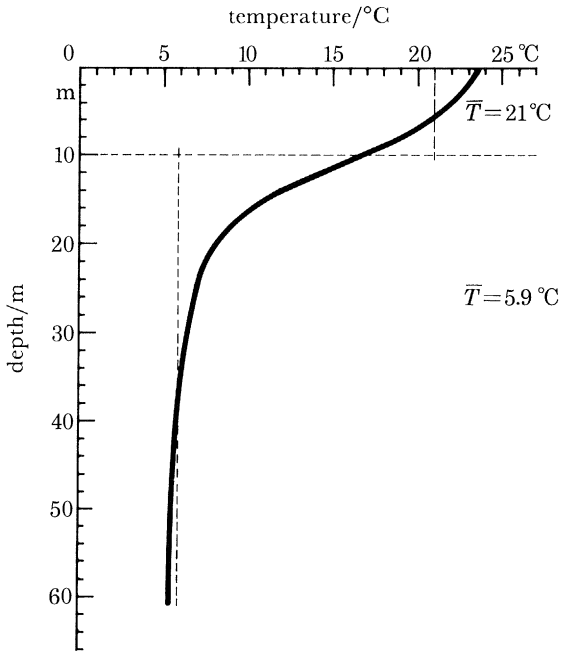

FIGURE 15. Average vertical temperature profile determined from all temperature profiles taken in the positions shown with open circles in figure 14 during the entire measuring period in July–August 1979. The stratification is approximated by a two-layer model with an upper layer depth and temperature of 10 m and 21 °C, and lower layer temperature 5.9 °C. These temperatures give $\epsilon = 1-\rho_1/\rho_2 = 1.94 \times 10^{-3}$. (From Hutter *et al.* 1983.)

but the measurements of the buoy at Cassarate station 4 (near Lugano) were interrupted owing to unexpected repairs, and atmospheric measurements taken at the Porlezza station terminated on 8 August because of vandalism. Wind data show a conspicuous daily cycle at the Porlezza station 7. The winds are mainly along the lake axis with strong maxima usually arising at 16h30 G.M.T. and blowing roughly from WSW to ENE. This daily cycle is also seen at Cassarate station 4 with, however, smaller maximum amplitudes and less structure along the shore. At the third meteorological buoy, Campione-Ferrera station 2, the daily cycle is still weaker and is overshadowed by relatively strong wind gusts every 2–3 days. The strong daily signal at Porlezza station 7 is responsible for the onset of the fundamental and higher mode internal gravity wave seiches (Hutter *et al.* 1983). The lower-frequency 2-to 3-day signal at Campione-Ferrera station 2, on the other hand, appears to have excited low-frequency (3-day) second-class topographic waves. The primary purpose of §6 is to demonstrate this result, which was not expected in so small a lake (17 km × 1.5 km).

(*b*) *Discussion of temperature, current and wind time-series*

Here we describe the various time series obtained from moorings 1–8 shown in figure 14. Despite the fact that the thermistor chains were positioned in the upper hypolimnion and recorded temperatures between 5 and 10 °C or less, these records form the backbone of the field programme. Isotherm-depth time-series, interpolated from the thermistor chain temperature measurements, are often interrupted because isotherm depths leave the depth range in which temperatures were recorded. Nonetheless, direct inspection of isotherm-depth series can reveal the fundamental time scales of the processes in the lake. However, for spectral analysis

(see §6*d*) continuous records of the temperature data are required. The mean temperature displacement function $\hat{z}(t)$ is used for that purpose, which can be interpreted as the vertical displacement of the water particles. The function $\hat{z}(t)$ is representative of the mean isotherm-depth time-series, but it is also an extrapolation outside the range of recorded temperature. The details of calculating $\hat{z}(t)$ from thermistor chain data and its comparison with isotherm-depth time-series are given in Hutter *et al.* (1983).

Figure 16 shows examples of the unfiltered time series of wind energy and isotherm depth, and serves as an illustration of the processes and associated time scales that can be identified. Note that the temperatures belonging to the isotherm-depth time-series are not all the same, the range being from 6.6 to 7.5 °C. This is because, in all cases, only those isotherm depths that were least interrupted were selected.

With the exception of the period from 9 to 14 July, the mean wind field at Porlezza and Cassarate is dominated by strong northeasterly afternoon winds down the mountain flanks with maximum 2 h means of approximately 7 m s^{-1}. This 24 h oscillation is extremely weak at station 2 (Campione-Ferrera, not shown in the figure) where somewhat smaller-scale wind gusts arise at an intermittency of about 2 days. The isotherm-depth time-series disclose oscillations with periods of 24, 12 and 8 h (indicated by open triangles and arrows in figure 16) and interstation phase differences which, by use of a two-layer model, can be interpreted as internal gravity wave seiches (Hutter *et al.* 1983). We now focus our attention on the earlier part of the isotherm-depth time-series from stations 1, 4 and 8, which clearly reveal a 74 h signal (marked by circles ◓). It is this low-frequency oscillation that led to the conjecture (Hutter *et al.* 1983) of second-class waves existing in the Lake of Lugano.

To emphasize this wave signal the troughs of the isotherm depths in figure 16 have been made prominent by thick solid and dotted lines. The front of this wave arises first at station 4 (9 and 10 July), propagates southwards and reaches station 1 approximately 7 h later (indicated by the solid line connecting the troughs at Cassarate and Melide). Upon reflection at the southern end (Melide), the wave reaches station 4 again (though split up into two smaller minima with an intermediate maximum, indicated by an arrow marked with an encircled 1), is next seen at station 8 with a conspicuous minimum (dotted heavy lines) and reappears in the early morning of 13 July at station 4. This completes one cycle forth and back along (anticlockwise around?) the lake. The propagation of the wave can clearly be followed from 13 to 16 July; the troughs are again marked by heavy lines in figure 16, but beyond 16 July an identification of the process by eye is doubtful. Nevertheless, the recorded time series covers approximately 40 days, corresponding to 13 cycles, which is long enough for filtered data to disclose reliably the significance of processes with the time scales of the order of 3 days. The associated wave speed seen in figure 16 is approximately 12 cm s^{-1} – much smaller than the speed of 43 cm s^{-1} of a long internal gravity wave in a two-layer model (see equation (6.3)). This fact alone strongly suggests that the 74 h signal is a second-class wave. (Also, it cannot be an internal (two-layer) Kelvin wave since this travels with the internal wave speed given earlier.)

To see the 74 h period signal more clearly, time series for July and August are filtered such that all high-frequency gravity oscillations were removed. A rectangular filter with a cut-off period of 30 h was used and the smoothed data were replotted (figure 17). At the top, stick diagrams of the wind velocities at Campione (i.e. Ferrera), Cassarate and Porlezza (where available) are shown; below them, the mean temperature displacement functions at the stations

PHILOSOPHICAL TRANSACTIONS OF THE ROYAL SOCIETY A MATHEMATICAL, PHYSICAL & ENGINEERING SCIENCES

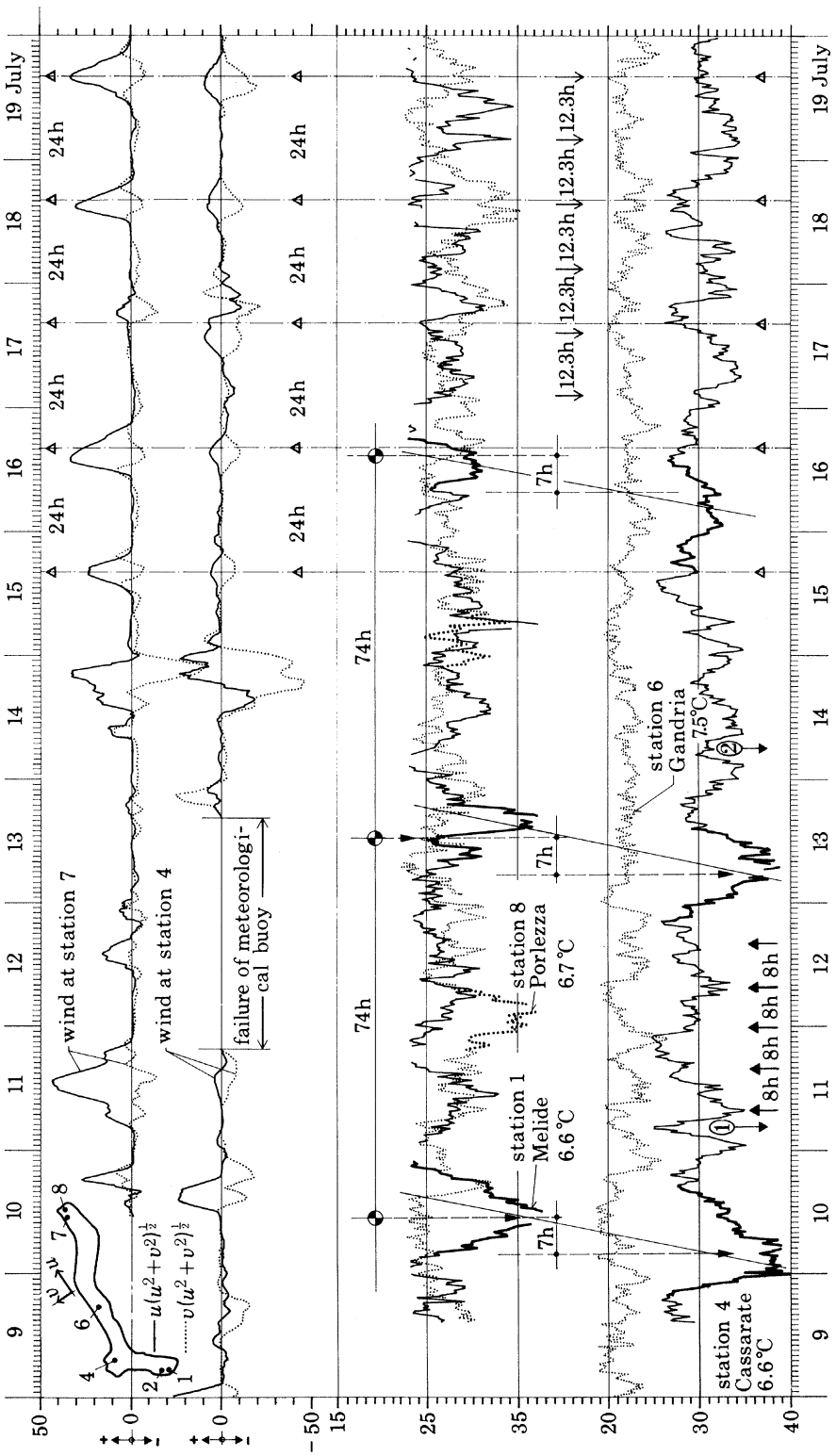

FIGURE 16. Time series of 2 h means of the longitudinal and transverse components of the wind energy ($\frac{1}{2}(u^2+v^2)^{\frac{1}{2}}u$, $\frac{1}{2}(u^2+v^2)^{\frac{1}{2}}v$, with directions of u and v components as indicated in the insert in the upper left corner) at the stations 7 (Porlezza) and 4 (Cassarate) and unfiltered time series of selected isotherm depths at the stations 1 (Melide, top solid curve), 8 (Porlezza, dotted, superposed on the Melide curve) and 4 (Cassarate, solid curve). Components of the motion with conspicuous periods are marked by special symbols: troughs in heavy solid and dotted lines and marked by circles ● are for 74 h; triangles for 24 h; arrows for 12 h or 8 h. The time shown is from 9 to 19 July 1979. (From Hutter *et al.* 1983.)

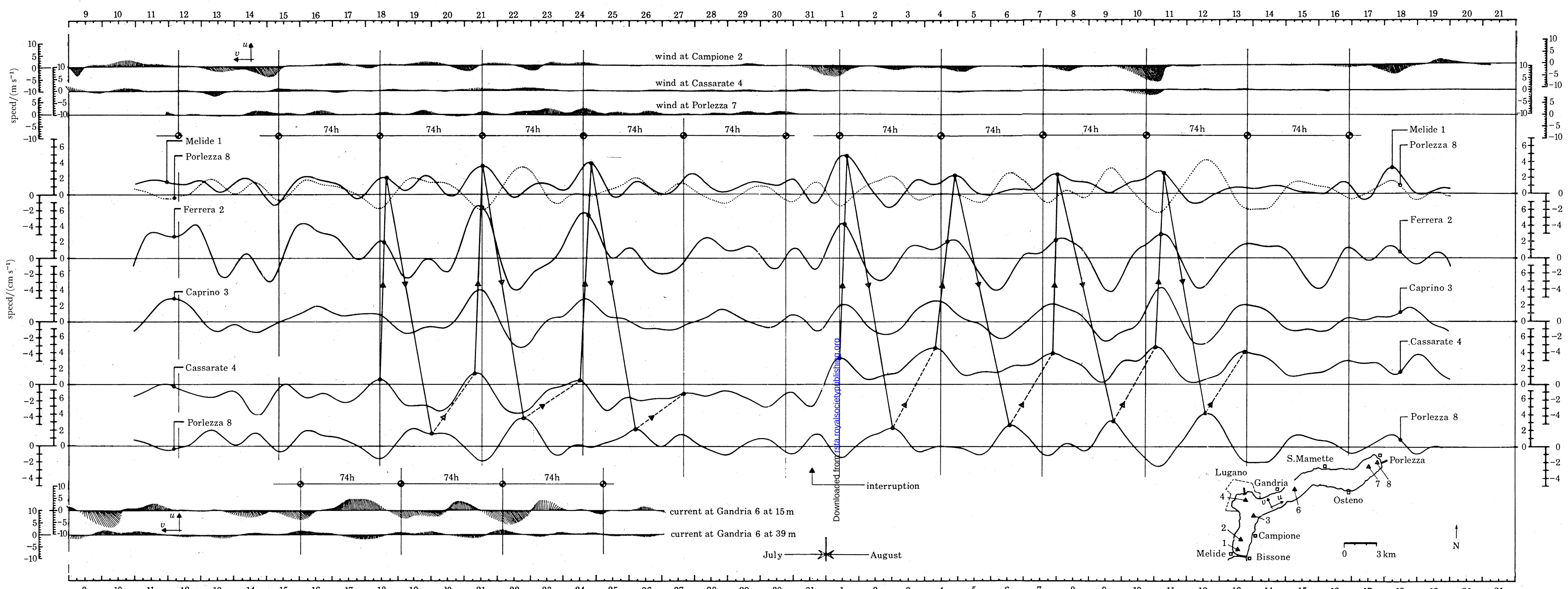

FIGURE 17. Time series for the Lake of Lugano measurements from 9 July to 21 August 1979. The data were smoothed to eliminate all processes with periods shorter than 30 h. At the top, stick plots of the wind at stations Campione (Ferrera) 2, Cassarate 4 and Porlezza 7 are shown (see insert for location). In the middle, the mean temperature displacement functions at Melide 1, Ferrera 2, Caprino 3, Cassarate 4 and Porlezza 8 are displayed. Superimposed on the time series at Melide is that of Porlezza (dotted). At the bottom, stick diagrams of the current at 15 and 39 m depths at Gandria 6 are shown. For both the wind and current, the directions of the components u, v are as indicated in the insert in the lower right corner. For all stations, u is 30° north of east. Vertical lines mark a period of 74 h and the sloping lines indicate the progression of the wave crests (marked with dots).

(*Facing p.* 32)

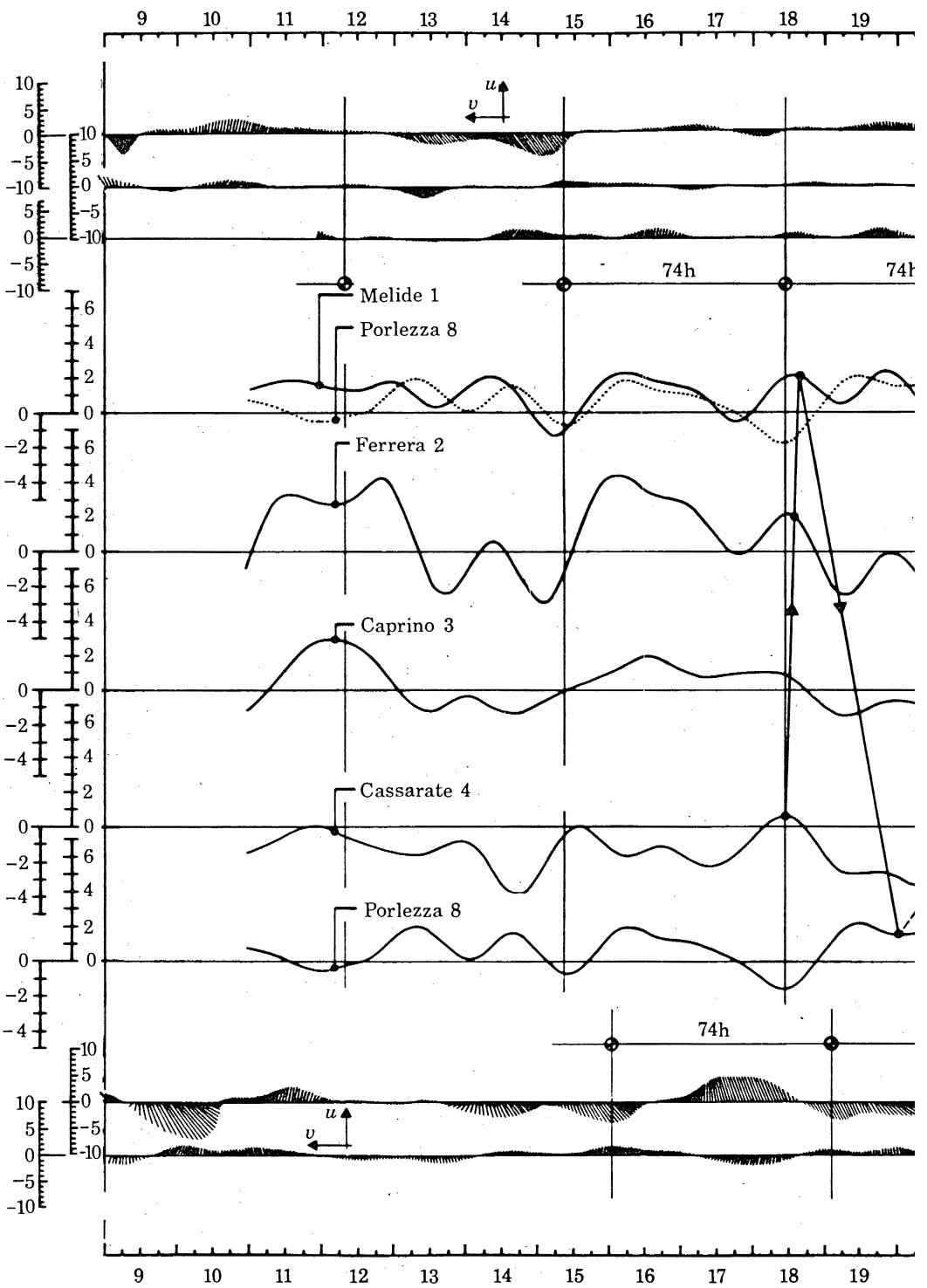

FIGURE 17. Time series for
stations Campione (Fe
are displayed. Superi
the directions of the c
of the wave crests (ma

PHILOSOPHICAL TRANSACTIONS OF THE ROYAL SOCIETY A MATHEMATICAL, PHYSICAL & ENGINEERING SCIENCES

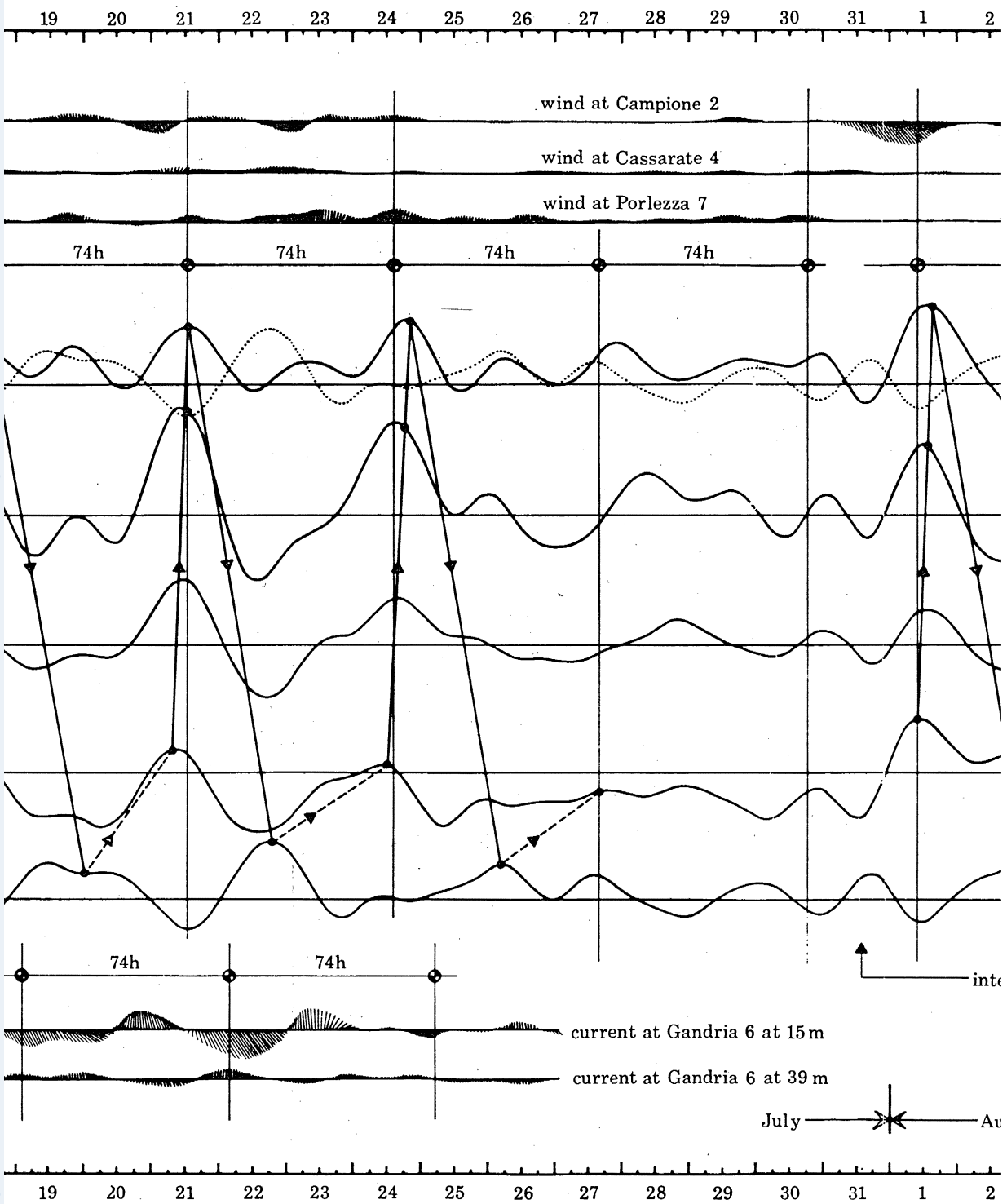

ne series for the Lake of Lugano measurements from 9 July to 21 August 1979. The data were smoothed to eliminate al
ampione (Ferrera) 2, Cassarate 4 and Porlezza 7 are shown (see insert for location). In the middle, the mean temperature di
yed. Superimposed on the time series at Melide is that of Porlezza (dotted). At the bottom, stick diagrams of the curren
ons of the components u, v are as indicated in the insert in the lower right corner. For all stations, u is 30° north of east. V
e crests (marked with dots).

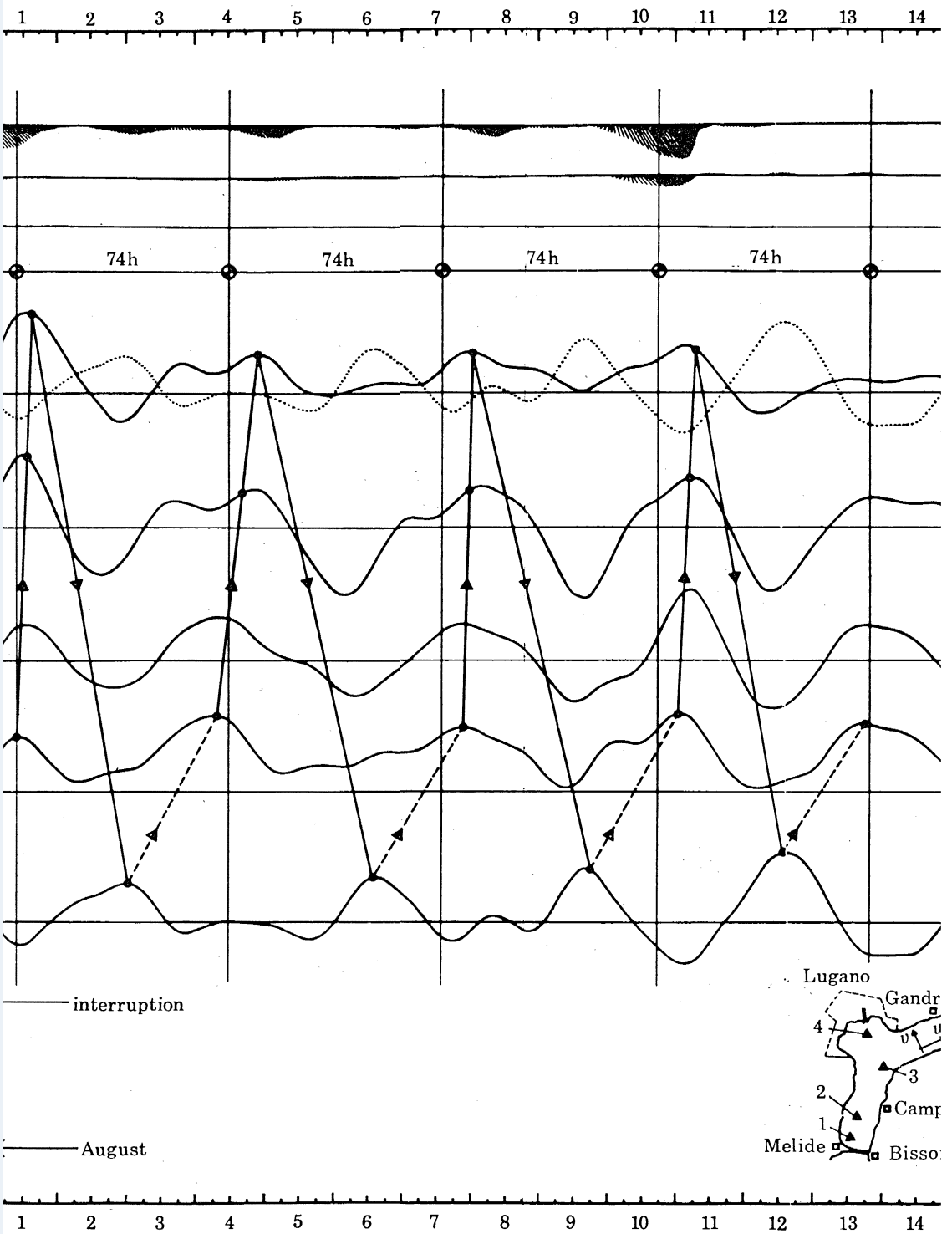

eliminate all processes with periods shorter than 30 h. At the top, stick plots of the wind at
nperature displacement functions at Melide 1, Ferrera 2, Caprino 3, Cassarate 4 and Porlezza 8
f the current at 15 and 39 m depths at Gandria 6 are shown. For both the wind and current,
th of cast. Vertical lines mark a period of 74 h and the sloping lines indicate the progression

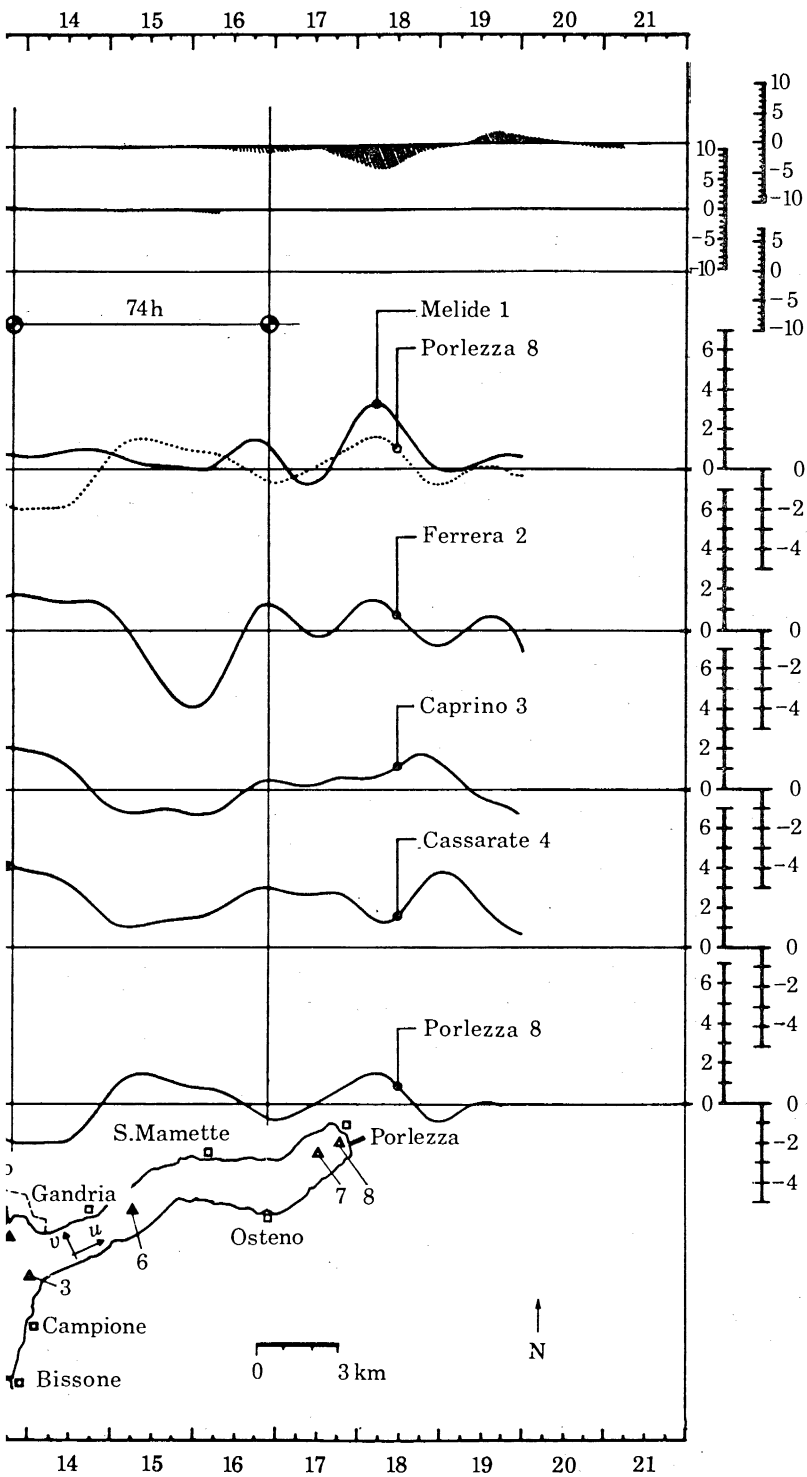

(*Facing p.* 32)

PHILOSOPHICAL TRANSACTIONS OF THE ROYAL SOCIETY A MATHEMATICAL, PHYSICAL & ENGINEERING SCIENCES

Melide 1, Ferrera 2, Caprino 3, Cassarate 4 and Porlezza 8 with the time series for station 8 superimposed on that of station 1; at the bottom, the stick diagrams show the current at Gandria 6 in 15 and 39 m depths. Vertical lines, marked by ◔, indicate a period of 74 h.

Figure 17 covers the period 9 July to 21 August, and hence the first part (9–19 July) overlaps with the unfiltered time series shown in figure 16. In particular, note that the two highs seen on 15 and 18 July in the unfiltered Cassarate time series (figure 16) are reproduced in the filtered time series (in figure 17 these highs have vertical lines through them). The same also applies to two corresponding lows seen in the Porlezza time series on these dates. Inspection of the filtered time series of mean temperature displacement functions reveals that the 74 h signal first noted in figure 16 is a dominant feature for the period 12–30 July (6 cycles) and again for the period 1–16 August (5 cycles). The two sub-sequences are broken up, with an episode of less than 74 h duration. The interruption of the 74 h rhythm on 30 July is probably due to the stormy winds blowing over the southern end of the lake on this day (see wind record from Campione). Comparison of the filtered wind data (where available) with the temperature time series indicates that the 74 h temperature oscillation cannot possibly be due to direct forcing from the wind, since the latter shows no regular 74 h signal. Rather, the filtered wind data reveal a certain spatial inhomogeneity, with long-period (2–3 days) wind fluctuations being the largest at Campione. It is such quasi-periodic winds that may continuously excite the 74 h temperature oscillations. Alternatively, the oscillations could be generated following a storm that suddenly ceases (for example, as on 15 July).

Regarding interstation phase relations, we note that, very roughly, the temperature time series for the four southwestern stations (1–4) show a high when that at Porlezza to the northeast has a low, and vice versa. But this out-of-phase behaviour is not always discernible (for example, on 15 July). Rather, the connected slanted lines in figure 17 suggest a progression (of wave crests marked with solid circles) in the order Cassarate, Ferrera, Melide, Porlezza and back to Cassarate, which is consistent with the anticlockwise progression noted in figure 16 during the period 10–16 July. To save space, the time series from Caprino 3 has not been fitted into this phase progression. To do so we would have had to place the Caprino time series high above that of Melide to simulate the geographical separation of Caprino from Melide.

A further interesting piece of information that can be extracted from figure 17 concerns the relative amplitudes of the mean temperature displacement functions $\hat{z}(t)$. Amplitudes are largest at station Ferrera 2, moderate at Caprino 3 and small at the other stations. However, one must be cautious in making a quantitative comparison of these amplitudes since the depth range of the thermistor chain data (from which the $\hat{z}(t)$ functions were calculated) was not the same in all stations. (The ranges were: Melide 1, 23–38 m; Ferrera 2, 37–57 m; Caprino 3, 35–55 m; Cassarate 4, 19–39 m; Porlezza 8, 22–37 m.) Nevertheless, it is interesting to note that at the near-shore stations 1 and 8 the amplitude is quite small, in qualitative agreement with the geometrical optics solution for the interfacial displacement, which vanishes along the shore (see equation (5.8)).

Data on the current are only available up to 27 July and continuous records have only been obtained for the current meters moored at the mid-lake station Gandria 6 at 15 and 39 m depths. The first part of the record (10–15 July) shows (at both depths) an oscillation with a period of about 4–5 days. In the upper layer this current oscillation seems to be directly forced by the wind, although there is a lag of about half a day in the current. After 15 July, when the Campione wind died out, both time series indicate three cycles of an oscillation with a 74 h

PHILOSOPHICAL TRANSACTIONS OF THE ROYAL SOCIETY A MATHEMATICAL, PHYSICAL & ENGINEERING SCIENCES

period that is about three-quarters of a day out of phase with the temperature oscillations at southwestern stations 1–4. This phase shift lends further support to the hypothesis that the 74 h signal represents a (linear) wave motion, since Gandria mooring 6 is in the middle of the lake and therefore is about one-quarter of a period (three-quarters of a day) travel time away from the southwestern stations. Moreover, this oscillation is surface-intensified, and the currents at the two depths are approximately 180° out of phase during this period (16–25 July). Throughout the record we also note that the velocities at 39 m are mainly parallel to the shore (see insert in figure 17, where positive u- and v-components are defined), but those at 15 m depth also have a non-negligible transverse component. The upper layer currents (at 15 m) are evidently not simply correlated with the winds after 15 July, reflecting the fact that they are probably a mixture of barotropic, baroclinic and wind-driven components.

Figures 18 and 19 show progressive vector diagrams of the current at Gandria station 6, at 39 and 15 m respectively. At 39 m depth the path traversed by a 'particle' along the trace of the progressive vector diagrams is basically along the main axis of the lake. However, a small cross-lake component is visible, the result being several elongated open loops traversed in an anticlockwise manner. On the other hand, at 15 m (figure 19) the progressive vector diagram shows a substantial transverse excursion and a sequence of large open loops indicated by arrows. Except for the first, these loops are each traversed in approximately 3 days in the anticlockwise direction. However, the anticlockwise motion around these loops is approximately 180° out of phase with the anticlockwise motion around corresponding deeper loops in figure 18, a feature that is consistent with the 180° phase shift seen in the currents in figure 17. For example, see the loops for 16–18, 19–21 and 21–23 July.

The relatively large horizontal particle excursions implied by figure 19 (of the order 5 km) suggests that these oscillations of a period of several days could be very important for the dispersion of pollutants in the Lake of Lugano. Particulate matter released one day in the upper 10–15 m at Gandria, for example, could very well find its way to the bay of Lugano in the next day and a half.

(c) *Theoretical results for fundamental-mode period, interfacial displacement, and currents for Lugano parameters*

An estimate of the fundamental-mode period for the Lake of Lugano from use of the frequency relation (4.16c) was given by Mysak (1985). Based on the values of the topographic parameters shown in figure 20, we find $a = l/L = 0.575$ and hence $\xi_s = 1.15$ upon using the relation $a \cosh \xi_s = 1$ (see equation (4.4)). Such a relatively large value of ξ_s corresponds to a fairly wide lake model for Lugano ($W/L = 1/1.225$, whereas in reality $W/L \approx 1/10$ (see figure 14)). However, as discussed at length in Mysak (1985), only such large values of ξ_s accurately model the sloping topography at the ends of intermontane lakes, a feature that provides the basic restoring force for topographic waves. A small value of ξ_s (0.1 say, corresponding to $W/L = 1/10$ (see table 1)) is a poor fit to the topography in these end regions and leads to an extremely long (several months) fundamental-mode period. Substituting $\xi_s = 1.15$ and $d_s = D/D_s = 2.59$ into (4.21) gives $b = 0.83$. Hence from (4.16c), in which ξ_s, b have these values and $\alpha = \alpha_1 = \pi(1+\delta_1)/\xi_s$ (with $\delta_1 = -0.419$), we obtain

$$T_{11} = 2\pi/f\sigma_{11} = 74.2 \text{ h} \tag{6.1}$$

for $f = 1.05 \times 10^{-4}$ s^{-1}, the value of f at 46° N, the latitude of Lugano. The value of T_{11} as given by (6.1) is fairly robust to moderate changes in l, L, D and D_s (which determine ξ_s and b),

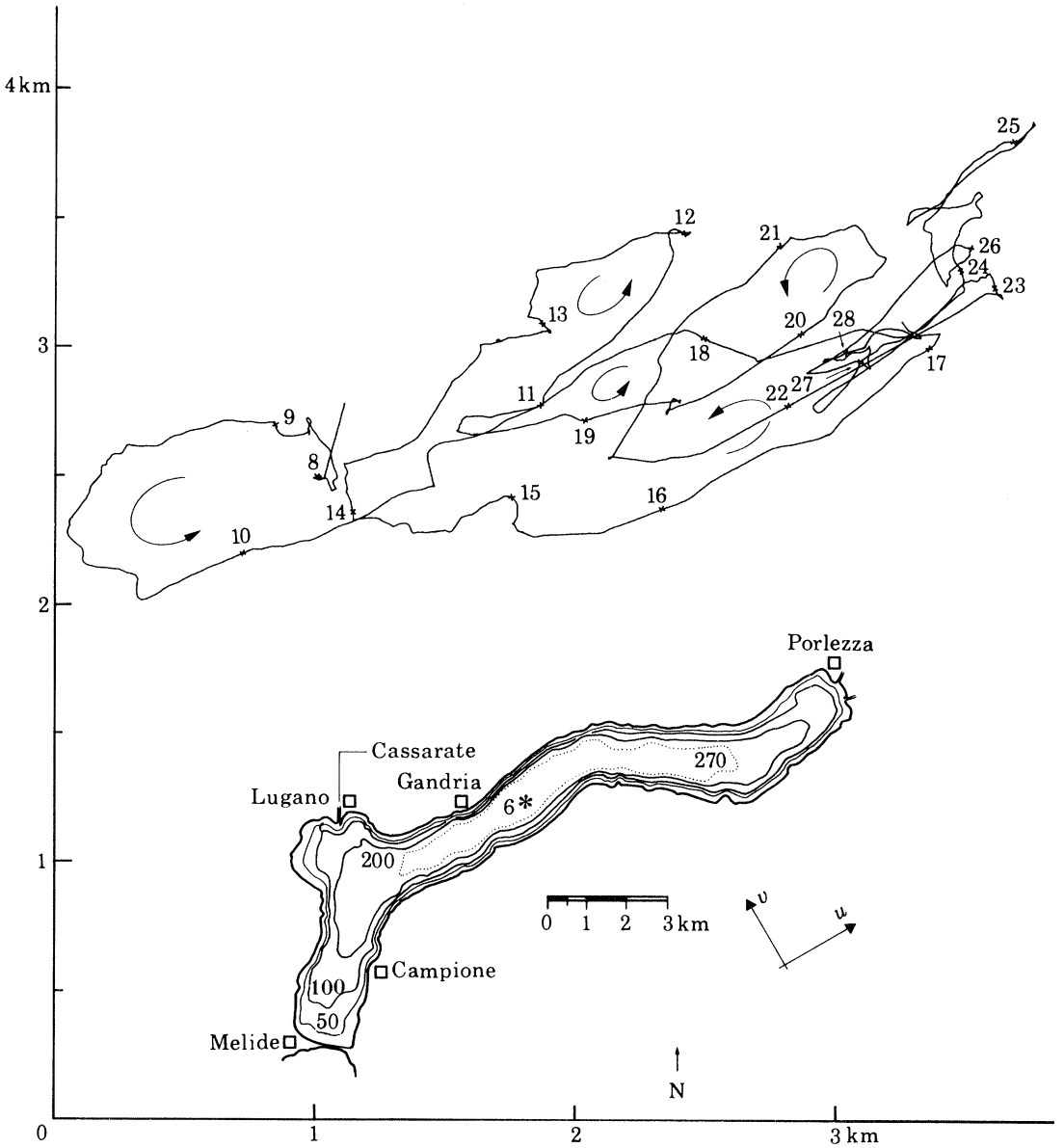

FIGURE 18. Progressive vector diagram of the current at station 6 (Gandria) at 39 m depth. The current is mainly along the shore (see insert), but anticlockwise rotation, indicated by arrows, is also discernible. Numbers indicate dates from 8 to 28 July 1979.

and thus the period 74.2 h can be regarded as a typical figure. It is surprisingly close to the observed value of 74 h.

As seen from figure 15, the stratification for summer 1979 in the Lake of Lugano is well described by a two-layer fluid with

$$\epsilon = 1-\rho_1/\rho_2 = 1.94\times 10^{-3}, \tag{6.2}$$

where $D_1 = 10$ m, $D_2 = 270$ m, so $D = D_1+D_2 = 280$ m. Hence

$$\left.\begin{aligned} c_i &= (\epsilon g D_1 D_2/D)^{\frac{1}{2}} = 0.428 \text{ m s}^{-1}, \\ r_i &= c_i/f = 4.08 \text{ km}. \end{aligned}\right\} \tag{6.3}$$

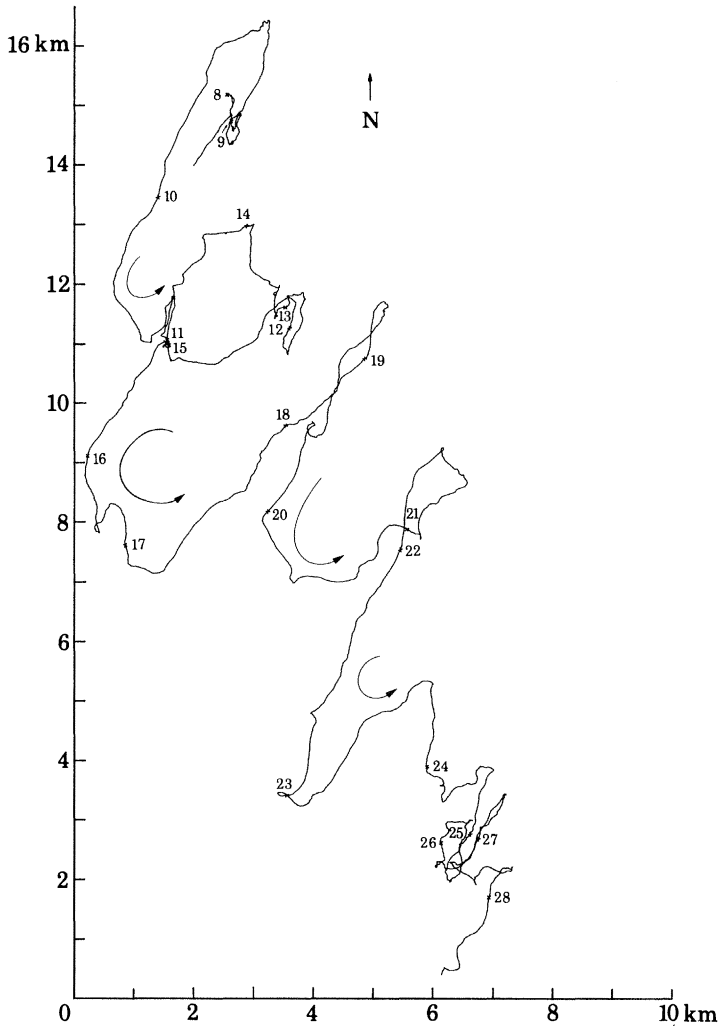

FIGURE 19. Progressive vector diagram of the current at station 6 (Gandria) at 15 m depth. The current has components along the shore and transverse to it. It rotates as indicated by the arrows, with a period of approximately 3 d. Numbers indicate dates from 8 to 28 July 1979.

The half-length L is 8.7 km (see figure 20), and therefore

$$S^{-1} = L^2/r_i^2 = 4.55. \tag{6.4}$$

Since $D_1/D_2 = 0.037$, neglecting terms of $O(D_1/D_2)$ is indeed a very good approximation for the Lake of Lugano. However, the geometrical optics approximation, which required neglecting a term of $O(1)$ compared to a term of $O(S^{-1})$, appears to introduce an error of about 20% (see equations (5.1), (5.5), (5.6) and (6.4)).

Figure 21 shows five 'snapshots' of the fundamental-mode interfacial displacement, as given by (5.9) for the Lugano parameters given above. In addition to the theoretically predicted anticlockwise propagation, which was observed in the mean temperature displacement functions plotted in figure 17, we note the large displacements near the ellipse's foci (see especially figure 21 *b*, *c*, *d*). This amplitude feature qualitatively agrees with large displacements seen in the temperature time-series from Ferrera, which lies near the focus closest to Melide.

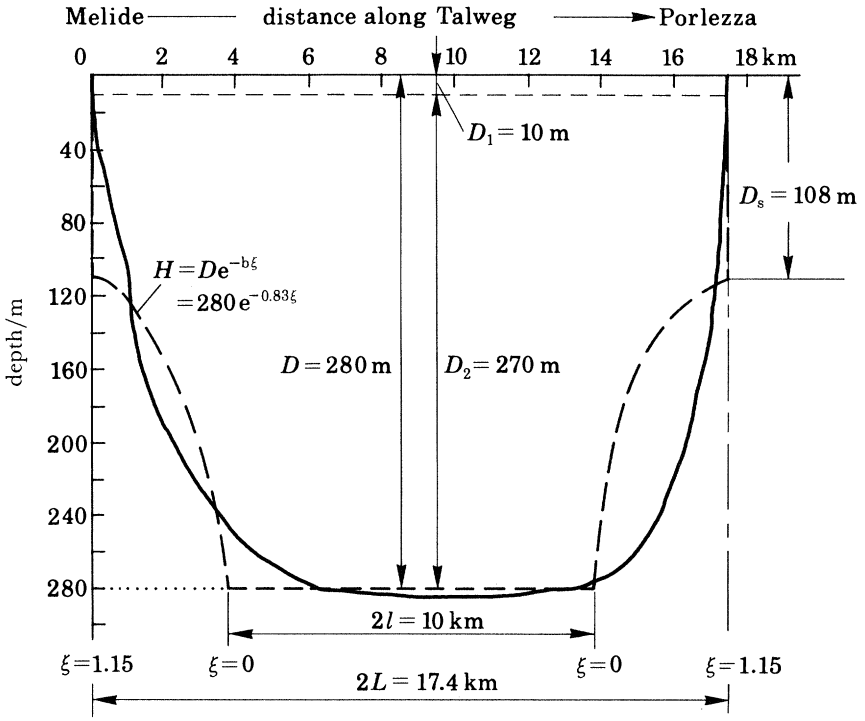

FIGURE 20. Depth profile along Talweg (solid line) and exponential model fit (broken line) of the north basin of the Lake of Lugano. Also shown is the two-layer stratification used in the theory (also see figure 15).

Also, from figure 21*b*, we note the behaviour of the displacement from each end of the lake, which is 180° out of phase, a result which was often observed in figure 17.

Figure 22 shows three shapshots of the fundamental-mode barotropic velocity, as given by (5.4) for the Lugano parameters. The anticlockwise rotation of the vector near the centre of the ellipse is in qualitative agreement with the anticlockwise motion seen in the Gandria progressive vector diagram for the data about the current at a depth of 39 m, which is representative of the lower layer motion (figure 18). Also, the elongated elliptical particle paths near the ellipse's centre can be seen in the data at 39 m (for example, see the loops for 11–14 July and 19–22 July in figure 18).

Figure 23 shows three shapshots of the fundamental-mode upper layer baroclinic velocity, given by (5.11) and (5.12) for the Lugano parameters. Comparison with figure 22 for the lower layer barotropic current shows that the currents are 180° out of phase and that the baroclinic currents are larger, by a factor of about ten near the ellipse's centre, and by a factor of about three near the sides. The composite of figure 22 and 23 is shown in figure 24, the total upper layer current given by (5.10). Clearly, the topographic wave currents in our model lake are surface intensified, with the upper layer current being largely baroclinic and having an amplitude about six times that of the lower layer near the lake centre. This is about twice as large as the observed ratio: the bottom part of figure 17 shows that the currents at 15 m have a typical scale of 8–9 cm s^{-1}, whereas the currents at 39 m are of order 2–3 cm s^{-1}. However, it must be emphasized that the record at a depth of 15 m is an *underestimate* of the upper layer currents since this depth occurs in the lower half of the thermocline (see figure 15). Thus it would be expected that the low-frequency currents nearer the surface would be even larger,

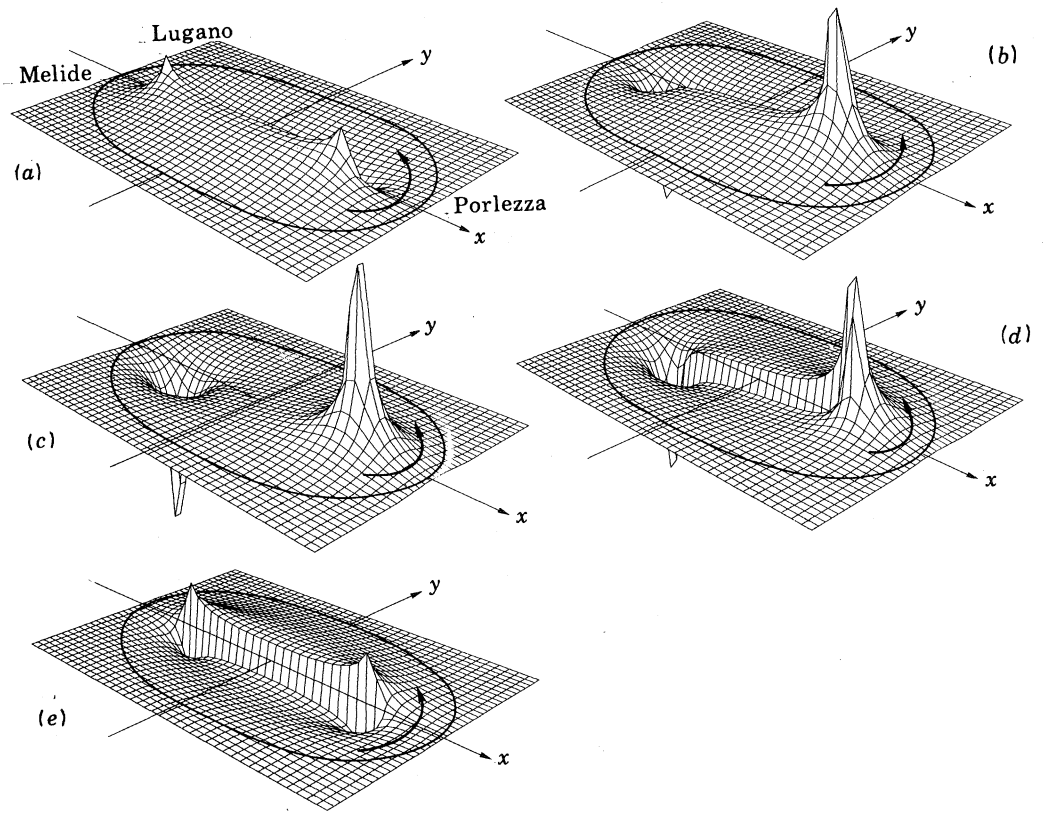

FIGURE 21. Interfacial displacement ζ_{11} for the Lugano parameters: $b = 0.83$, $\xi_s = 1.15$, $a = 0.575$ and $S = 0.22$ for (*a*) $\sigma_{11}t = -\frac{1}{2}\pi$, (*b*) $-\frac{1}{4}\pi$, (*c*) 0, (*d*) $\frac{1}{4}\pi$, (*e*) $\frac{1}{2}\pi$.

in agreement with the theoretical prediction. However, the theoretical upper and lower layer currents both rotate anticlockwise near the lake centre, in agreement with the motion in figures 18 and 19. Further, the currents in each layer are 180° out of phase, a feature that is also observed for the three cycles marked at the bottom of figure 17.

(*d*) *Spectral analysis of wind and temperature data*

The purpose of this subsection is twofold. Firstly, we carry out a spectral analysis of the wind fluctuations and study their coherence with the temperature fluctuations to determine whether the wind does indeed serve as a driving force for the 74 h oscillation observed in the time series (figure 17). Secondly, by means of a cross-spectral analysis of the temperature fluctuations from different pairs of stations, we wish to establish more rigorously the anticlockwise propagation of the 74 h signal around the lake.

For spectral analysis the original time series were filtered with a rectangular filter with cut-off period of 30 h. The corresponding transfer function was convoluted with a convergence factor that removes the Gibbs phenomena (Bloomfield 1976, p. 132). In the resulting time series, the best linear trend was determined and subtracted; the emerging time series then fluctuate about a zero mean and permit better identification of the conspicuous peaks, while associated periods are only slightly changed. To reduce leakage this time series was further processed by using a 'split cosine bell window', extending over the length of the data, and a tapering of 10% (see

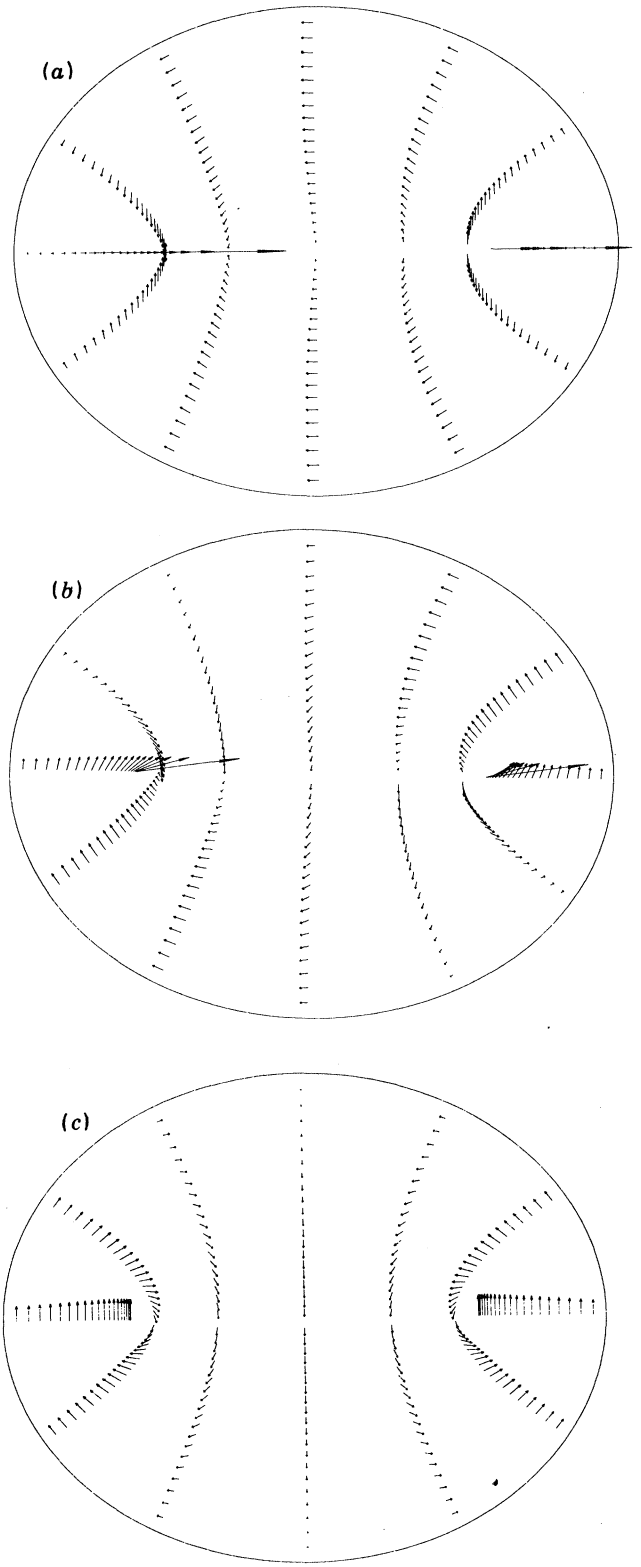

FIGURE 22. Fundamental-mode barotropic current for the Lugano parameters used in figure 21: (*a*) $\sigma_{11}\, t = -\frac{1}{2}\pi$, (*b*) $-\frac{1}{4}\pi$, (*c*) 0.

PHILOSOPHICAL TRANSACTIONS OF THE ROYAL SOCIETY A MATHEMATICAL, PHYSICAL & ENGINEERING SCIENCES

Bloomfield 1976, p. 84). After this process the fast Fourier transform was applied and the power spectra were further smoothed with the spectral window shown in the insert in some of the subsequent figures. Power spectra, coherence, and phase were calculated. In the power spectra graphs, 'energy density times frequency' is plotted against the logarithm of the frequency. Such a representation is energy conserving. Furthermore, for statistical confidence we use the χ^2-distribution with 15 degrees of freedom, and we plot coherence $c(f)$ against $\lg(f)$, but for the 95% confidence limit, $\arctan c$ will be used because this makes the 95% confidence limit independent of frequency (see Jenkins & Watts 1968).

The data processing was also done without a filter. Spectra of these unfiltered data give information about the amount of energy contained in gravitational oscillations and in the second-class modes. Figure 25 serves as an example. It shows the variance spectra and coherence for the mean temperature displacement functions at Porlezza and Ferrera in the period range from 10 to 1000 h. The dominant peak at 24 h marks the period of the fundamental internal gravity wave seiche; it contains the most energy. There are two sidelobes with high coherence at periods of 12 h and approximately 74 h. All oscillations with periods less than or equal to 26 h, say, can be interpreted as internal gravity wave seiches (Hutter *et al.* 1983). They cannot have periods longer than the cut-off period of 30 h. But processes with longer periods are sufficiently rich in energy that they form a significant part of the overall motion. From figure 25 we note that oscillations in the period range 60–90 h carry far more energy than does the second mode of the gravity seiches. This is also qualitatively true for the other spectra. Second-class motions are therefore at least as important as the higher mode internal seiches.

(i) *Wind data*

Owing to instrument failure and vandalism, wind data from Campione (Ferrera), Cassarate and Porlezza have different lengths. The missing event at station 4 for 11–13 July (see figure 16), resulting from a failure of the meteorological buoy, was filled by repeating the data measured at the nearby station Campione. This allowed comparison of time series of the wind at Campione and Cassarate covering approximately 43 days (about 14 periods). Measurements at the meteorological buoy at Porlezza terminated on 3 August. Cross-spectra obtained with time series of this station are, therefore, based on 23-day records only.

Figure 26 shows the station-pair distribution of variance spectra, coherence and phase difference of the more energetic u-component of the wind from the stations Campione 2, Cassarate 4 and Porlezza 7 (for location of the station and definition of the u-component, see insert map). According to figure 26*a* (upper left corner), during the 43-day episode most of the low-frequency energy occurs at Campione, the southernmost station. This is also evident from the wind time-series in figure 17. We also note that although each variance spectrum has an energy peak in the 60–90 h band, the coherence between the two time series (Campione and Cassarate) is low in this frequency range, indicating spatial inhomogeneity of the winds during this period. During the shorter 23-day event for the same station pair (figure 26*b*), the variance spectra are somewhat smaller but the fluctuations in the 60–90 h band are now coherent at the 95% level. Similar remarks also apply to the other station pairs, Porlezza–Campione (*c*) and Porlezza–Cassarate (*d*). Note that for the 23-day period 10 July to 2 August, the wind energy decreases from southwest to northeast, but the coherence is generally high in the indicated band. Hence there is coherent wind energy at 74 h, which could in principle generate temperature oscillations of this period, although at individual stations the energy maxima are

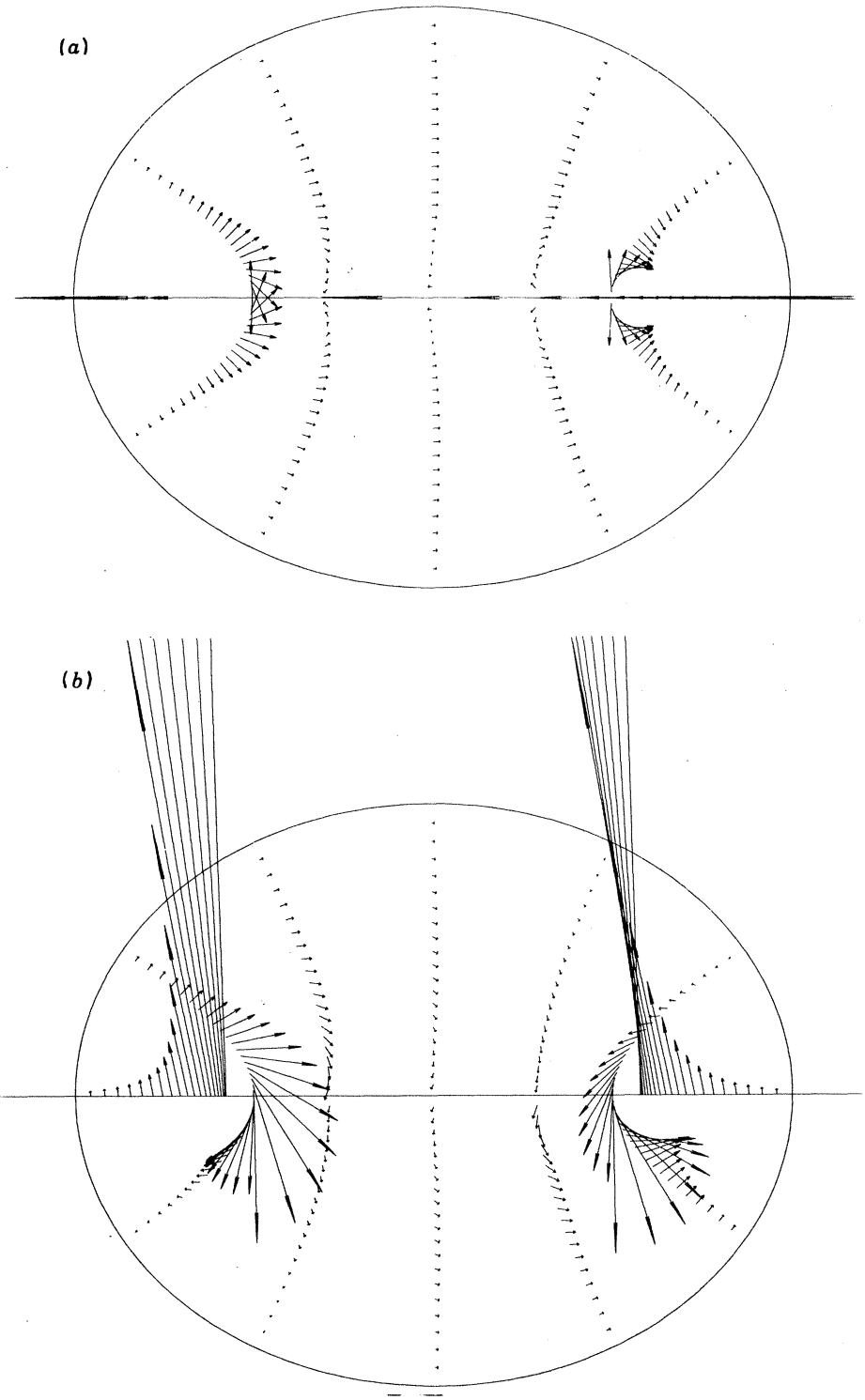

FIGURE 23. Fundamental-mode upper layer baroclinic current for the Lugano parameters used in figure 21: (*a*) $\sigma_{11}t = -\frac{1}{2}\pi$, (*b*) $-\frac{1}{4}\pi$, (*c*) 0. To compare with figure 22, the vectors here must be lengthened by a factor of 5.

PHILOSOPHICAL TRANSACTIONS OF THE ROYAL SOCIETY A MATHEMATICAL, PHYSICAL & ENGINEERING SCIENCES

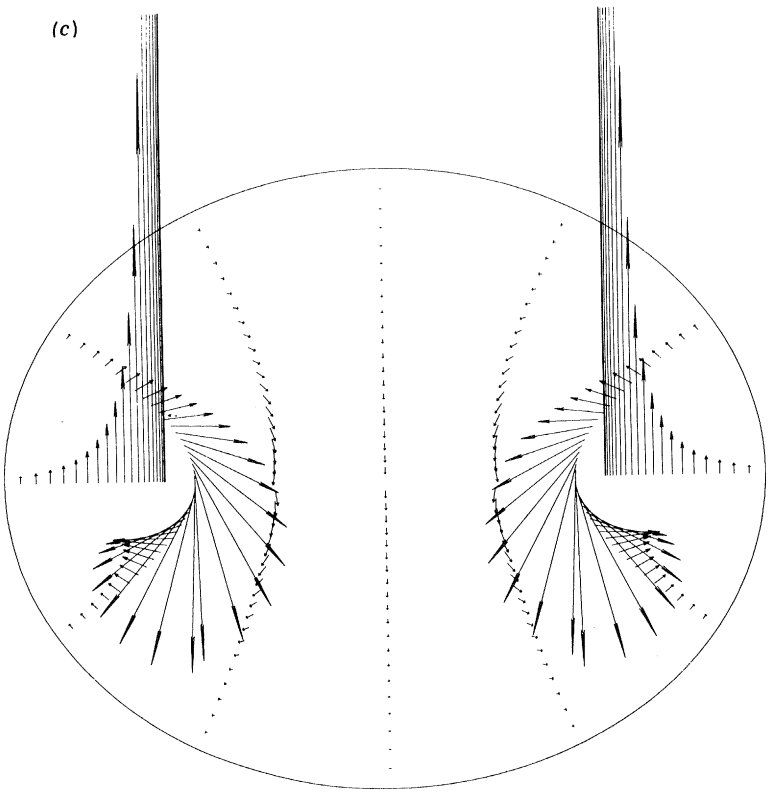

FIGURE 23*c*. For description see previous page.

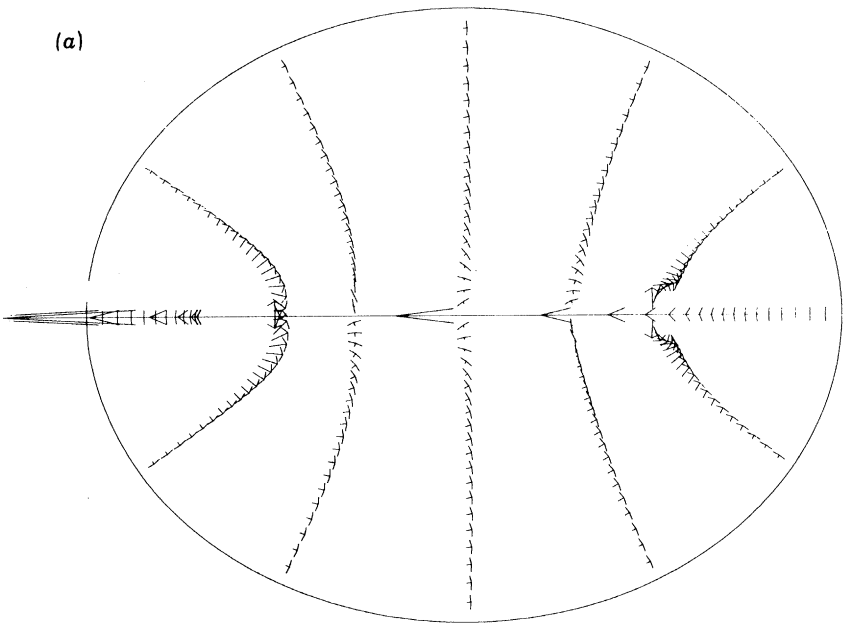

FIGURE 24. Total fundamental-mode upper layer current for the Lugano parameters used in figure 21: (*a*) $\sigma_{11}\, t = -\frac{1}{2}\pi$, (*b*) $-\frac{1}{4}\pi$, (*c*) 0. To compare with figure 22, the vectors here must be lengthened by a factor of 5.d

PHILOSOPHICAL TRANSACTIONS OF THE ROYAL SOCIETY A MATHEMATICAL, PHYSICAL & ENGINEERING SCIENCES

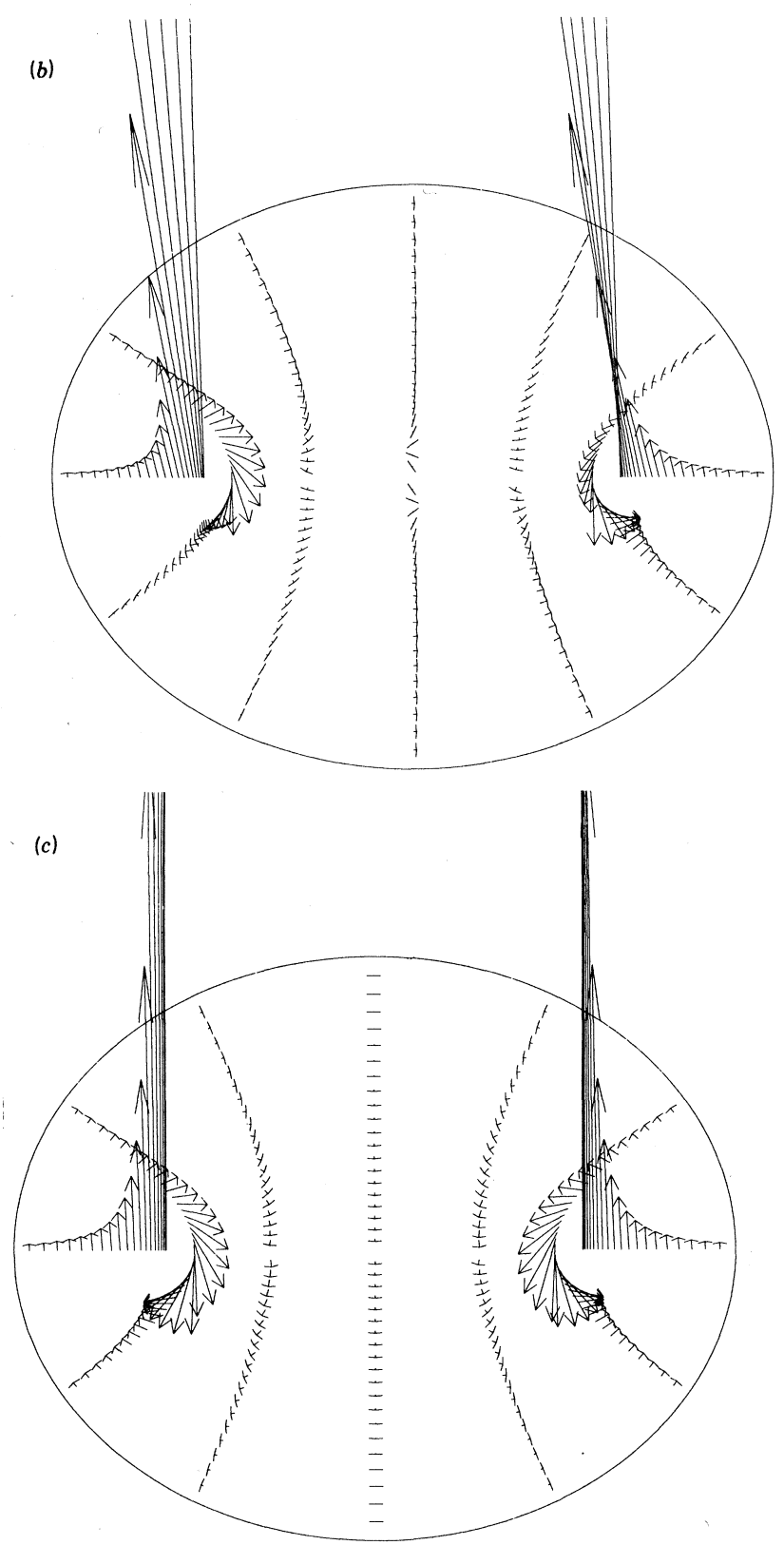

FIGURE 24 *b*, *c*. For description see opposite.

PHILOSOPHICAL TRANSACTIONS OF THE ROYAL SOCIETY A MATHEMATICAL, PHYSICAL & ENGINEERING SCIENCES

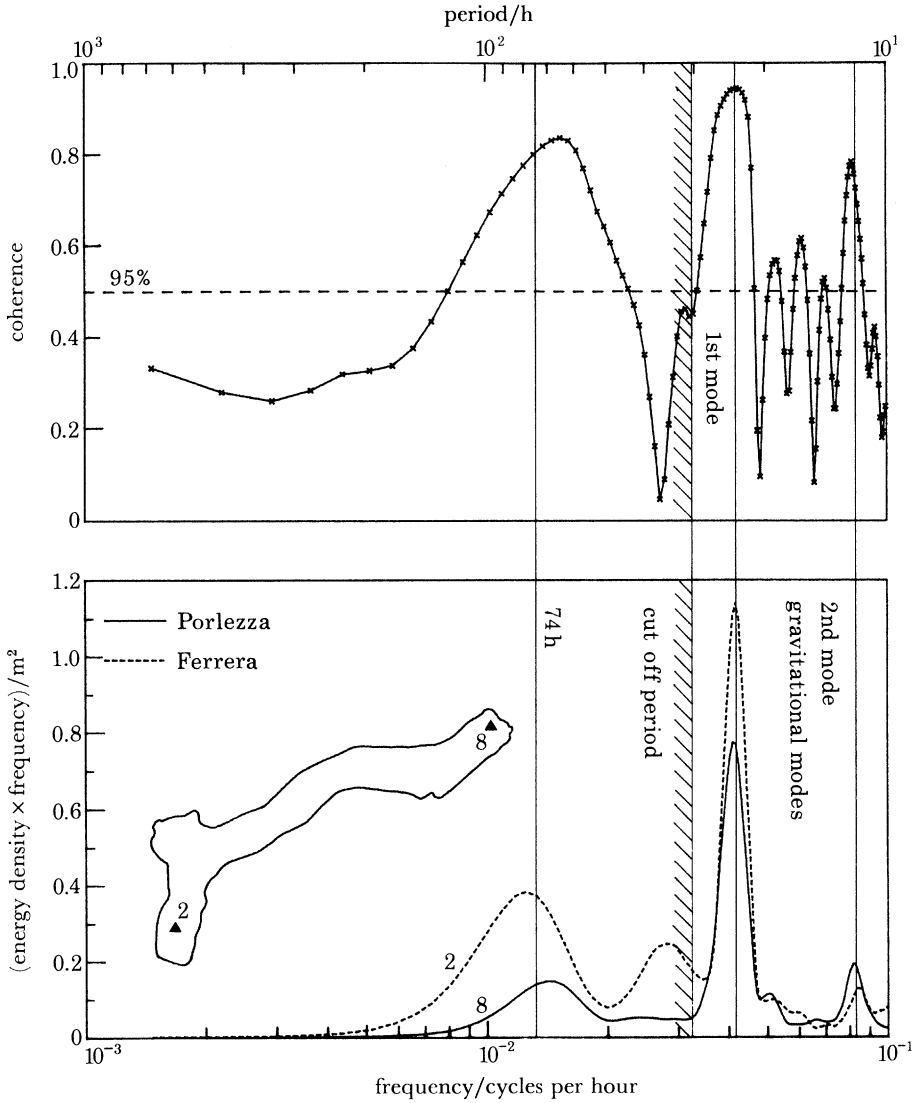

FIGURE 25. Variance spectra (energy density times frequency) of the unfiltered mean temperature displacement functions for the stations 2 and 8 as indicated in the insert (bottom), and coherence spectra of the time series pair (top) plotted against frequency or period. The duration of the time series was from 14h40 on 9 July to 09h20 on 21 August. The broken horizontal line indicates the 95% confidence limit. The two peaks to the right of the cut-off period of 30 h can be interpreted as the periods of the first two internal gravity wave modes. The vertical line labelled 74 h marks the period of the fundamental-mode topographic wave.

outside the 60–90 h band. This latter observation, however, appears to rule out the possibility of the 74 h temperature oscillation being directly wind-forced and thus being in resonance with the wind fluctuations. This point will now be examined more closely.

(ii) *Relation between wind and temperature fluctuations*

To show conclusively that the wind and the lake do not respond *unisono* to each other, cross-spectra of the *u*-component of the wind at a given station and the mean temperature displacement function at the same or neighbouring station were calculated (figure 27). The energy distributions of the wind data are broader than those of the mean temperature

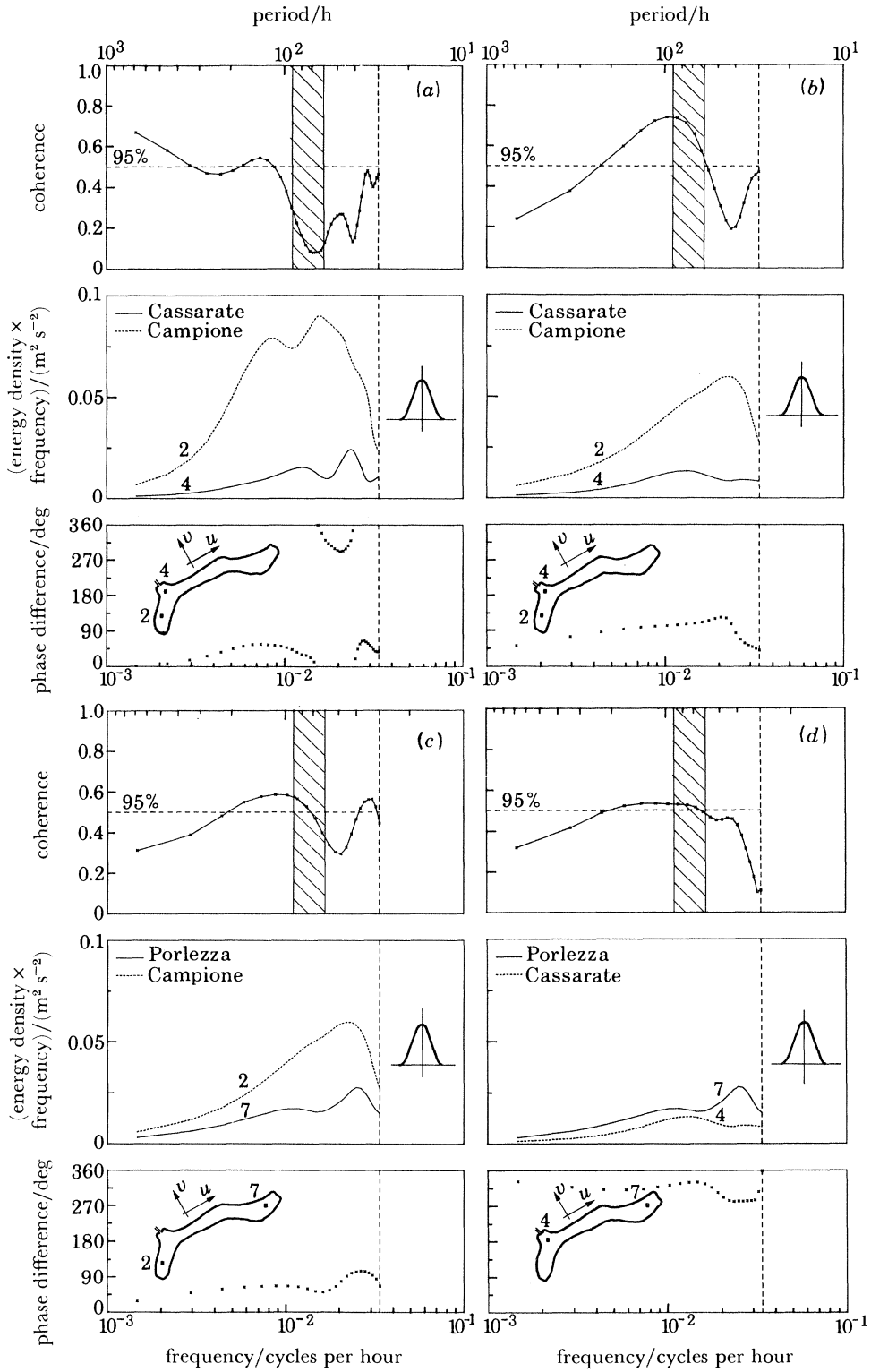

FIGURE 26. Variance spectra, coherence and phase difference of the filtered u-component (alongshore) wind measured 3 m above the water surface. Quadrants (*a*) and (*b*) (top) are both for the station pair Cassarate–Campione, but for different lengths of data (43 and 23 days respectively). In the lower left (*c*) and lower right (*d*) are the spectra for the station pairs Porlezza–Campione and Porlezza–Cassarate respectively, from which 23-day records were available. The middle figure in each quadrant contains the variance spectra, smoothed with the window shown in the insert. The top figure in each quadrant shows the coherence $c(f)$, and as a broken line, the 95% confidence limit of arctan c. The 60–90 h period band is also shown as a broken line. The bottom figure in each quadrant displays the phase difference of the two time series, with positive phase corresponding to the solid line station (see middle of quadrant) leading the dotted line station.

displacement functions. Coherence between the two data sets at Cassarate and Porlezza is generally very low, particularly in the 60–90 h band. Only the wind at Campione and the mean temperature displacement function at Ferrera have substantial energy at 74 h, and at this period the coherence between the two signals is close to the 95% confidence limit (see centre of figure 27). However, the phase difference does not show a 180° shift as the 74 h period is crossed, a feature that would arise in a resonant response of the lake. Nevertheless, it is conceivable that the energy source for the topographic waves in the Lake of Lugano could come from low-frequency, approximately alongshore wind fluctuations at the southern end of the lake. But clearly, more theoretical and observational work is required to elucidate the mechanism involved.

At this stage it is of interest to determine whether the winds of long period at Campione, whose amplitude scale can be estimated from figure 17, are sufficiently energetic to drive interfacial displacements of the scale observed at Ferrera and barotropic currents of the scale observed at Gandria (at 39 m depth). (It is more reliable to use the time series to estimate a typical wind speed than the spectrum in figure 27 since the latter are tapered, a process that reduces the amplitude scale and spreads the energy in frequency space. Also, as a consequence of removing the linear trend from the time series, the amplitude of a computed spectrum is significantly reduced (see, for example, figure 2 in Mortimer & Fee 1976).) For this purpose we now estimate the amplitude scales ζ_0 and U from the theoretical expressions (3.16) and (3.17) respectively. However, first we need a value for the wind stress scale τ_0. From the top of figure 17 we estimate that the wind fluctuations have a typical speed of $U_w = 3$–4 m s^{-1}. Taking $U_w = 3.5$ m s^{-1} as a characteristic value and using this in the formula

$$\tau_0 = \rho_{air}\, c_d\, U_w^2 \tag{6.5}$$

along with $\rho_{air} = 1.29$ kg m^{-3} and the drag coefficient $c_d = 2 \times 10^{-3}$, we find $\tau_0 = 0.032$ N m^{-2}. Hence

$$\zeta_0 = 1.5 \text{ m}, \quad U = 3.0 \text{ cm s}^{-1} \tag{6.6}$$

upon using (3.16) and (3.17). While the computed value of ζ_0 is somewhat lower than the observed displacements (typically 2–3 m; see middle of figure 17), the value of U agrees quite favourably with the magnitude of the barotropic (39 m) currents (typically 2–3 cm s^{-1}; see bottom of figure 17). It is important to recall, however, that the values in (6.6) have been obtained only from formulae derived from scaling arguments and *not* from the solution of the relevant forced problem. In this light the agreement between (6.6) and the observed amplitudes is quite good. It seems reasonable to argue, therefore, that the low-frequency fluctuations in the Lake of Lugano are adequately described by the system of equations (3.18), (3.19), (3.23*a*, *b*).

(iii) *Temperature cross-spectra*

To establish the anticlockwise propagation of the 74 h signal statistically, we now discuss the coherence and phase of the mean temperature displacement functions at the station pairs 8/4, 8/2, 8/1, 8/3 (figure 28) and 4/2, 4/1, 4/3 and 4/8 (figure 29). All the spectra are based on time series of approximately 43 days duration. The energy spectra of all mean temperature displacement functions have a maximum between approximately 69 and 80 h, where coherence between data pairs is generally high (over 0.85). The largest amplitude arises at station 2, Ferrera (figure 28, upper right; figure 29, upper left); the second largest but already

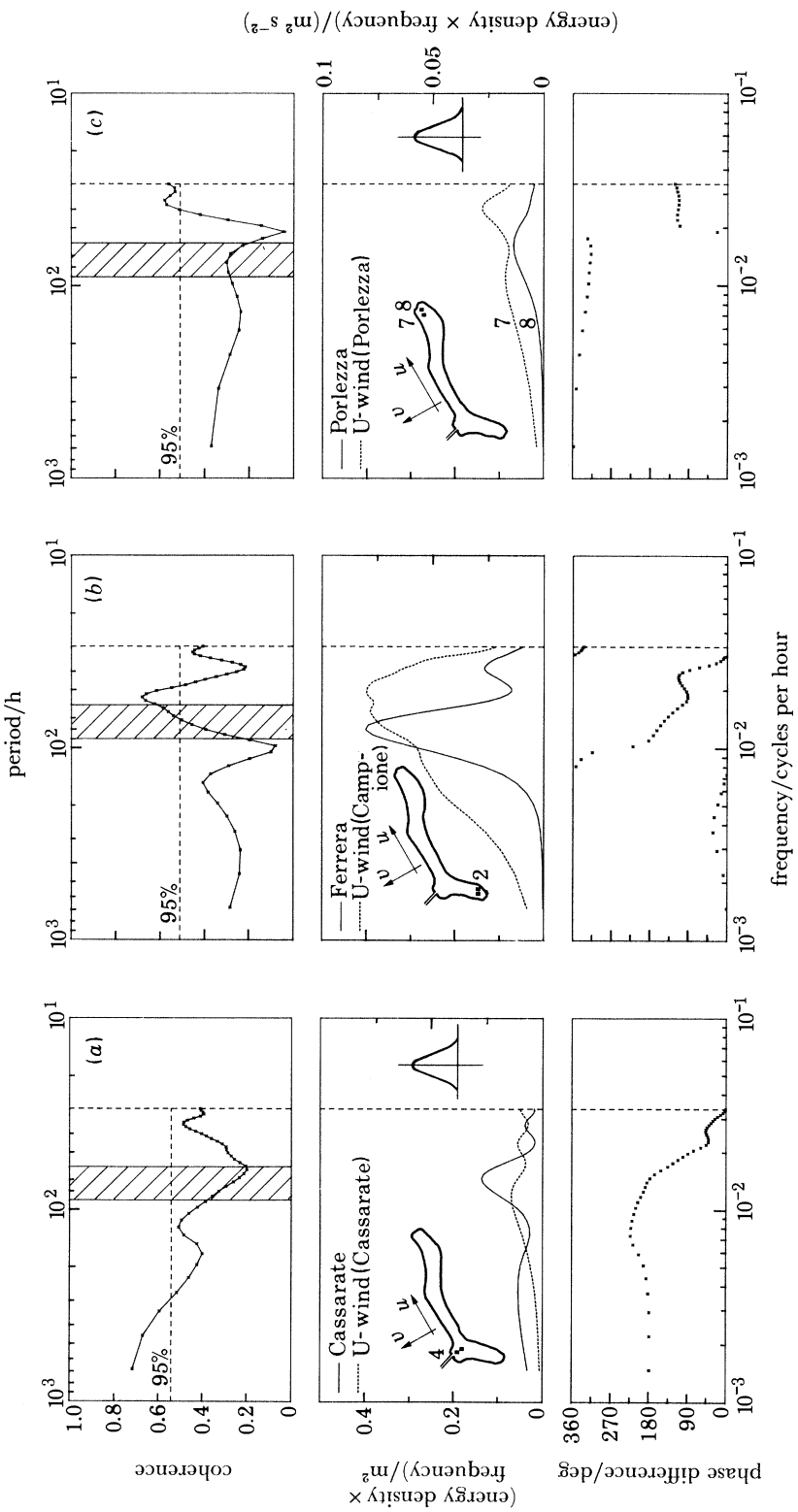

FIGURE 27. Variance spectra, coherence and phase difference of the filtered u-component of wind, measured 3 m above the water surface, and the mean temperature displacement function for the time series pairs: (*a*) wind (Cassarate)–temperature (Cassarate), (*b*) wind (Campione)–temperature (Ferrera), and (*c*) wind (Porlezza)– temperature (Porlezza) for the time periods. (*a*) *ca.* 40 days, (*b*) *ca.* 43 days, (*c*) 23 days. In the variance spectra the right and left scales apply to the wind velocity and temperature displacement respectively. Inserted in the variance spectra is the window used in the tapering of these spectra. At the bottom of each grouping the phase differences are shown; the definition of this phase difference is such that phases of data shown as solid curves in the variance spectra lead those of the data shown as dotted curves. Energy density scales for the mean temperature displacement function are shown on the left, those for the wind on the right.

PHILOSOPHICAL TRANSACTIONS OF THE ROYAL SOCIETY A MATHEMATICAL, PHYSICAL & ENGINEERING SCIENCES

substantially smaller peak arises at station 3, Caprino. The energies of remaining spectra are even smaller and follow in the order 8 (Porlezza), 4 (Cassarate), 1 (Melide). The maps inserted in the graphs of the energy spectra in figures 28 and 29 show the locations of the stations where the temperature measurements from the thermistor chains were taken, the arrow indicating the direction in which the phase propagates. Phase progression is always from the time series whose energy spectrum is shown as a solid line to that whose energy spectrum is shown as a broken line. Phase differences between station pairs at the 74 h period are indicated in figures 28 and 29 by an arrow at the left margin of the corresponding phase difference.

It is clear from figures 28 and 29 that the dominant process is an oscillation with a period of approximately 74 h. (The computations yield the energy maxima at the following periods: Porlezza, 71.8 h; Cassarate, 71.8 h; Caprino, 80.3 h; Melide, 68.5 h; Ferrera, 80.3 h; corresponding to a mean of 74.5 h). If this is the period of a topographic wave travelling around the basin in an anticlockwise manner, then the phase differences 8/4, 8/2, 8/1, 8/3 at the 74 h period should increase in this order. From the relative positions of the stations, one would expect that the phase differences should lie approximately between 150° and 225°. In fact the observed phase differences are 165° for 8/4, 185° for 8/2, 191° for 8/1 and 182° for 8/3. Except for this last pair, the phase indeed progresses in the expected manner, even though the phase differences appear to be a bit too large (one would expect the phase for 8/1 to be about 180°). The reason for the discrepancy in the phase difference of the station pair 8/3 is unknown. (A possible explanation may be because of interference of the Cassarate fluctuations on the Caprino record. Between Porlezza and Caprino one would expect approximately a 200° phase difference. This and the 165° phase difference observed between Porlezza and Cassarate average out to 182.5°, which is what is observed for 8/3.) But the phase difference of more than 180° between stations 8 and 1 in figure 28 may qualitatively be explained as follows: the wave travels right, bounded by the edge of the basin; if equal segments of the circumference are traversed in equal times, then it is natural that travel times between 8 and 1 along the northern shore are longer than along the southern shore, simply because of the bay at Lugano (see figure 14).

Conclusions from figure 29, which displays the variance, coherence and phase differences for the station pairs 4/2, 4/1, 4/3 and 4/8, are similar to those that can be deduced from figure 28. The coherences are very large at the 74 h period, and the insert maps again show the station pairs analysed and the direction in which the phase is propagating. For a topographic wave model, the phases must increase in the order of the station pairs 4/2, 4/1, 4/3 and 4/8. The observed phase differences in this order are 22°, 40°, 22°, 195°. Except for the station pair 4/3, this conforms with the predicted sequence and shows a consistency in the data with respect to phase.

Figure 30 shows all the variance spectra together in one graph. The relatively small amplitude of the 68.5 h peak of the spectrum for Melide 1, which is located in shallow water very close to shore, is consistent with the geometrical optics solution for ζ, since the latter is zero at the coast. The relatively large amplitude of the 80 h peak for Ferrera 2 can also be explained in part by the theory. Figure 21*c* shows that for $\eta = 0$ and π and $0 < \xi < \xi_s$, ζ is rather large and increases in amplitude as $\xi \to 0$ (the foci are approached). Since Ferrera lies on the line segment $\eta = \pi$ and is near the focus at this end of the lake, the observed relatively large amplitude is thus expected. However, another factor that could lead to the amplification of the Ferrera temperature displacement function is the relatively strong 2–3 day wind fluctuation at this location (see figure 27).

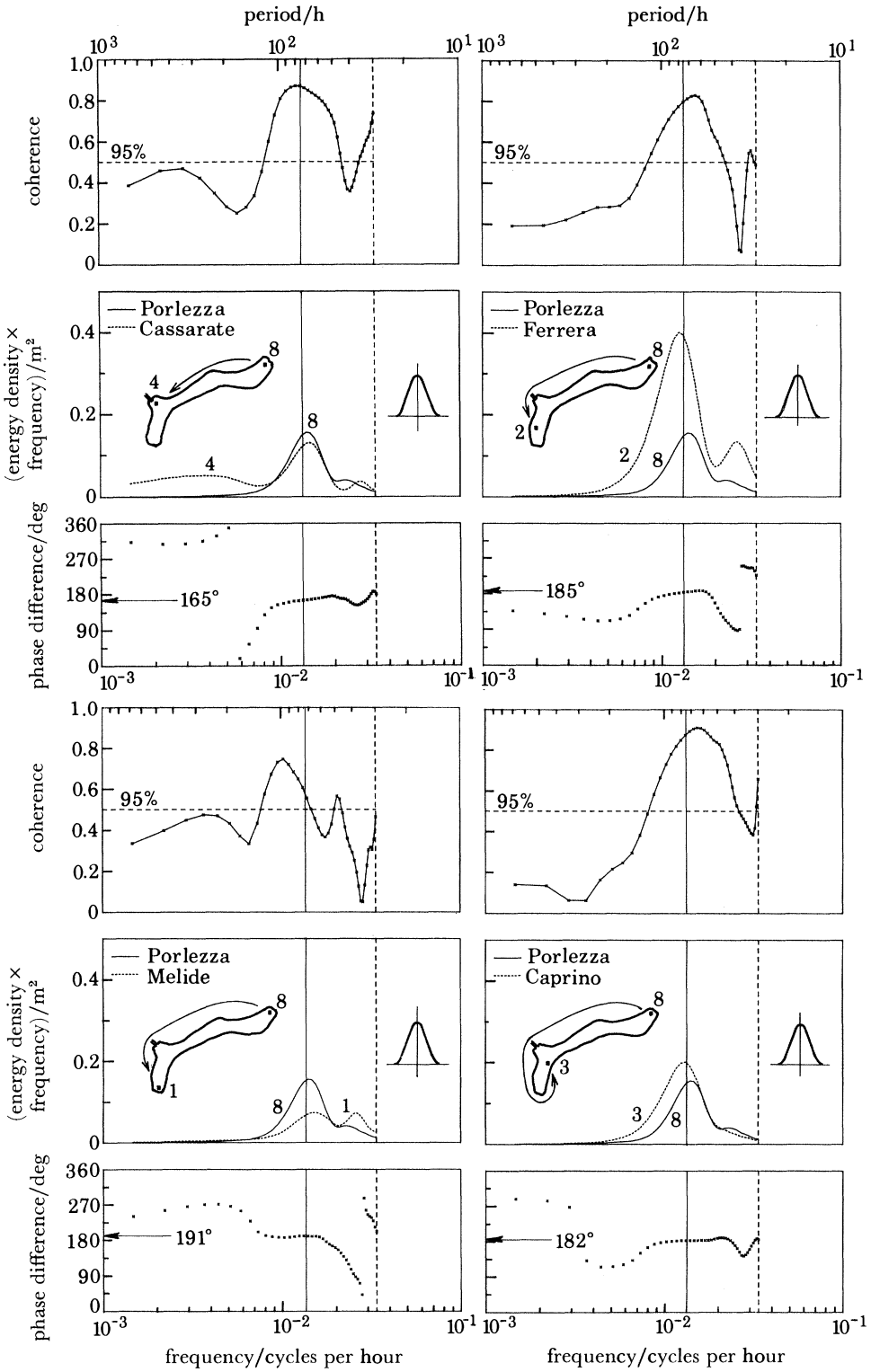

FIGURE 28. Variance spectra, coherence and phase difference of time series pairs of the mean temperature displacement function for an event of 43 days duration. Each quadrant is subdivided into three subfigures where coherence c, variance and phase difference are plotted. The vertical broken line marks the cut-off period of 30 h and the horizontal broken line in the coherence diagrams mark the 95% confidence limit of arctan c. The insert maps show the station pairs, the arrow indicating the direction of phase progression. The inserted window indicates the tapering of the spectra. The vertical solid line marks the period of 74 h, and the arrow on the left of each coherence diagram indicates the phase difference between the time series pair at that period.

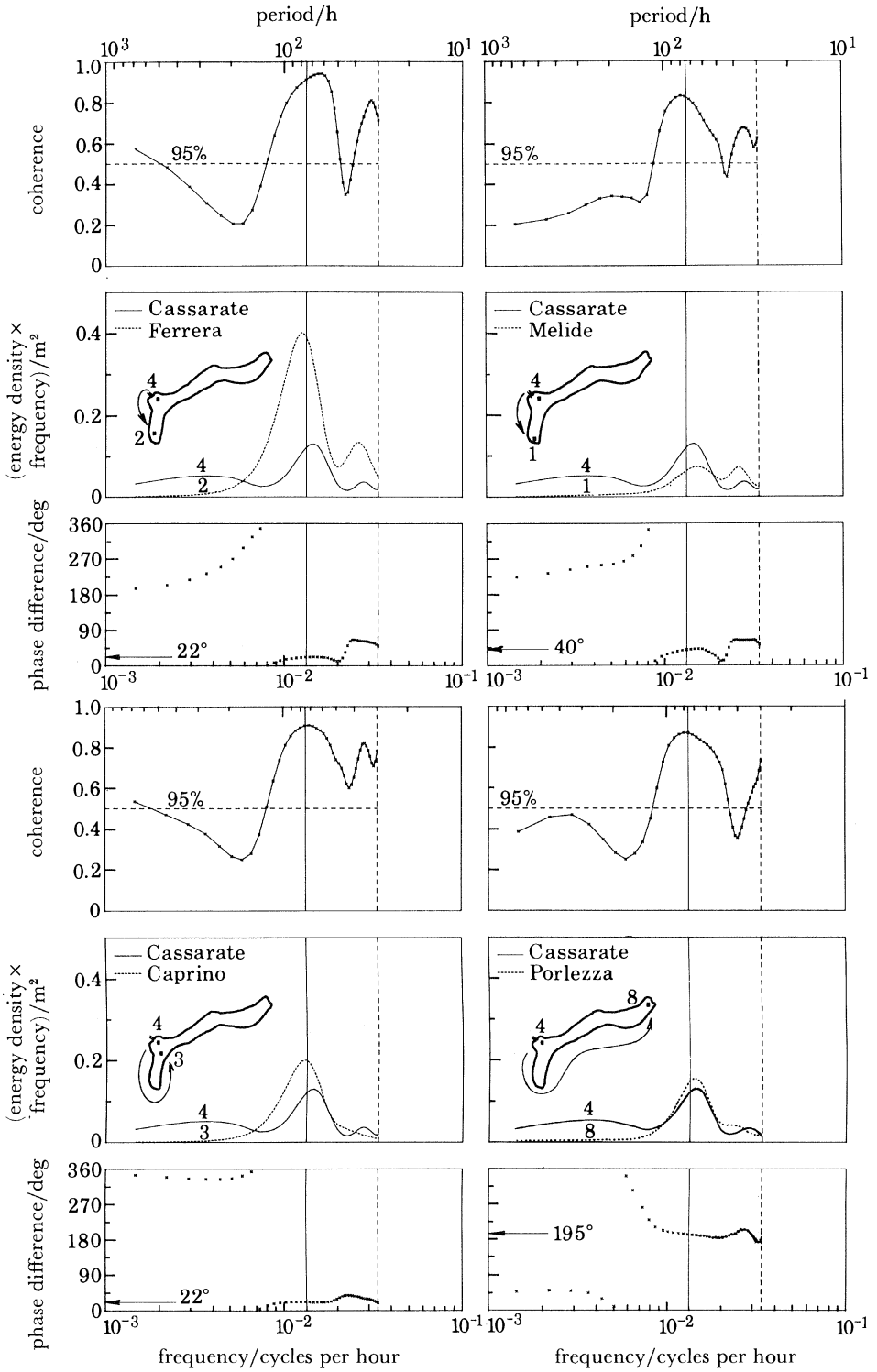

FIGURE 29. Same as figure 28 but for different station pairs.

PHILOSOPHICAL TRANSACTIONS OF THE ROYAL SOCIETY A MATHEMATICAL, PHYSICAL & ENGINEERING SCIENCES

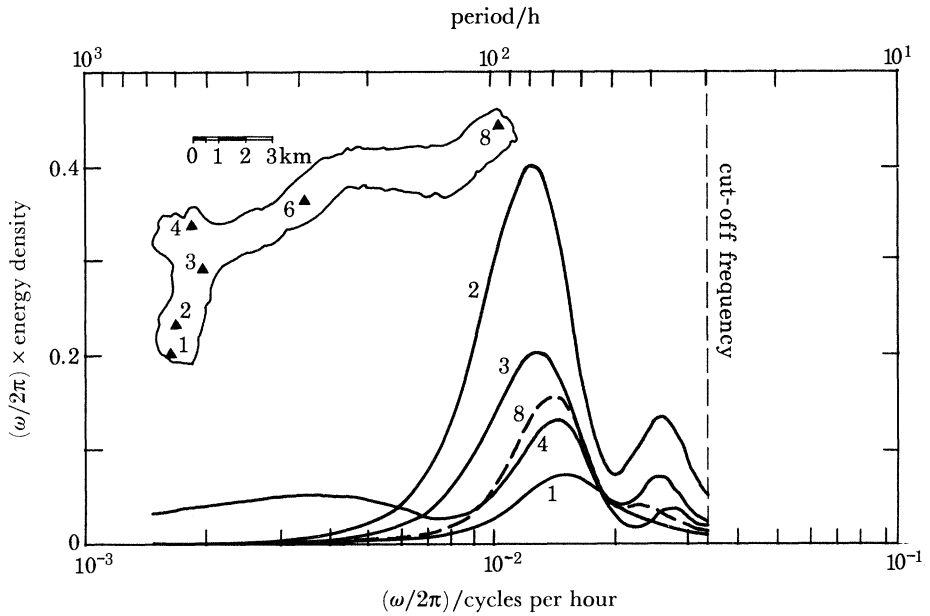

FIGURE 30. Variance spectra of the mean temperature displacement functions at the stations 1, 2, 3, 4 and 8.

(*e*) *Can the observations be interpreted as responses of a higher-order baroclinic Kelvin wave?*

It was suggested by a referee that the presence of higher vertical mode waves (for example, a second-mode internal Kelvin wave) may be able to account for the observed 74 h oscillation in the Lake of Lugano. To test this possibility several 'best fits' to the vertical temperature profile of figure 15 of a three-layered model were constructed and the associated internal Rossby radii and wave periods in a constant depth basin were calculated, by using Longuet-Higgins equations in Mortimer (1952). Table 3 summarizes a selection of such calculations and shows that the first and second-order vertical baroclinic modes have Rossby radii and periods as follows:

$$3800 \text{ m} < R_1 < 4755 \text{ m}, \quad 23.8 \text{ h} > P_1 > 19.1 \text{ h},$$

$$1220 \text{ m} < R_2 < 1890 \text{ m}, \quad 74.3 \text{ h} > P_2 > 48.0 \text{ h}.$$

While selection of the 'best' three-layer approximation is not unique, there is one set of choices (the first grouping in table 3) in which the period pair is close to (24 h, 74 h); all other choices have smaller periods. Thus the 74 h period must form a kind of threshold, which is difficult to bypass by the three-layer approximation of the given temperature profile. This is a first indication that the long-period response should not be interpreted as a higher order baroclinic internal Kelvin wave, simply because the measured spectra peak at 74–78 h and taper off to lower *and* higher periods.

The Rossby radii R_1 and R_2 are of the order of 4 km (as expected) and 1.2 km (for the 74 h period), respectively, which is slightly smaller than the minimum width of the lake. Phase progression of the waves is thus qualitatively consistent with a second vertical mode (74 h) Kelvin wave propagating cyclonically around the basin. There are, however, secondary observations, which make this interpretation an unlikely one: one has been mentioned above; another is that an effect of shore-trapping should be detectable. However, the isotherm-depth time-series of figure 16 show the largest amplitudes at Cassarate 4 and comparable or smaller

Table 3. Layer depths and temperatures of three-layer model approximations of the temperature profile (figure 15) and associated first- and second-order baroclinic radii and periods

layer depths/m			temperatures/K			Rossby radii/m		periods/h		
h_1	h_2	h_3	T_1	T_2	T_3	R_1	R_2	P_1	P_2	comments
11	19	149	21	8	5.5	4269	1231	21.3	73.8	Top temperature varies. Sensitivity to variations in third-layer variations is small.
.	.	.	20	.	.	4031	1227	22.5	74.0	
.	.	.	19	.	.	3792	1222	23.9	74.3	
11	19	189	21	8	5.5	4299	1298	21.1	70.0	
.	.	.	20	.	.	4060	1241	22.4	73.2	
.	.	.	19	.	.	3820	1236	23.8	73.5	
9.5	15.5	154	21	9	5.5	3992	1417	22.7	64.1	Temperature in middle layer varies. Strong temperature influence.
.	.	.	.	10	.	4007	1673	22.7	54.3	
.	.	.	.	11	.	4046	1889	22.4	48.0	
9.5	9.5	160	21	17	5.8	4755	1667	19.1	54.5	Variation of (h_1+h_2) with best temperature fit.
.	15.5	154	.	10	5.5	4007	1673	22.6	54.3	
.	20.5	149	.	9	5.5	3988	1603	22.8	56.6	

ones at Melide 1 and Porlezza 8. Also, and perhaps most importantly, from a Kelvin-wave point of view, reflections at the long ends of a basin are complete for such a long and narrow basin. Consequently, the Poincaré waves are all evanescent as one moves away from the long ends, and rotation of the velocity vector should not occur in the middle of the lake, as Kelvin-wave velocities are along the shore for all times. But figures 18 and 19 indicate an *anti*clockwise rotation of the velocities at the mid-lake station as they must for a topographic wave interpretation.

So, in all likelihood, the topographic wave model is the correct interpretation.

(*f*) *Summary of observations to support the topographic wave hypothesis*

We now briefly summarize the observations that support the concept of a free topographic wave in the Lake of Lugano.

(1) Time series of current and temperature data in the lake all show a coherent oscillation with a 74 h period; this period is longer than the fundamental internal seiche period of the Lake of Lugano. Energy spectra, in which gravity waves are filtered out, indicate that most energy is clustered around this period. The theoretical period of a fundamental-mode topographic wave in our model is 74.2 h.

(2) Cross-spectra of wind and temperature time-series show low coherence at 74 h, except at the southern end of the lake. However, even there, the coherence is just below the 95% confidence limit at a period of 74 h. Moreover, the wind forcing energy extends over a wider frequency band than that associated with the 74 h signal. So, the 74 h oscillation must be an intrinsic property of the lake, and not due to direct meteorological forcing.

(3) Order of magnitude estimates for the scales of the thermocline displacement ζ_0 and the barotropic current U made by using the theoretical relations (3.16) and (3.17) agree favourably with the observed amplitudes of the temperature displacement function and the barotropic current.

(4) The currents at a station close to the centre of the lake rotate in the anticlockwise direction, as predicted by the lowest mode of the elliptic topographic wave model. Moreover,

the currents are surface intensified and the upper and lower layer current fluctuations are 180° out of phase, in agreement with the theory.

(5) The distribution of the maxima of the temperature displacement functions at the various stations exhibits the behaviour predicted by the model. Amplitudes are small close to the shore and large near the southern focus of the elliptic lake model.

(6) Except for one station (Campione), in which the phase seems to be contaminated by interference with the signal from a nearby station, the phase of the 74 h signal propagates anticlockwise around the lake, with station-pair phase differences that are in qualitative agreement with the propagation of a fundamental-mode topographic wave.

7. Summary and concluding remarks

We have shown that for deep, stratified elongated lakes it is possible to decouple the governing differential equations for ψ (the barotropic stream function) and ζ (the interfacial displacement). This decoupling means that correct to $O(D_1/D_2)$, where D_1 and D_2 are the characteristic upper and lower layer depths (see figure 1), we first can solve the usual barotropic topographic wave equation for ψ. In general, this equation will contain wind-forcing terms, the largest of which is proportional to $\boldsymbol{\tau} \times \nabla h^{-1}$. This forcing term determines the amplitude scale for ψ and hence U, the barotropic current scale. The solution for ψ is then substituted into the governing equation for ζ and thus serves as a known driving mechanism for the interfacial displacement. Under the low-frequency approximation ($\mathscr{L} = \partial_{tt} + f^2 \simeq f^2$), ζ satisfies a forced modified Helmholtz equation. However, if $S^{-1} = L^2/r_1^2 \gg 1$, the geometrical optics approximation applies, yielding simply $\zeta = S \int (\nabla\psi \times \nabla h^{-1}) \cdot \hat{\boldsymbol{z}}\, \mathrm{d}t$. Finally, ψ and ζ are substituted into a pair of expressions for $\boldsymbol{u}_1$ and $\boldsymbol{u}_2$, the horizontal currents in each layer. To $O(D_1/D_2)$, $\boldsymbol{u}_2 = h^{-1}\hat{\boldsymbol{z}} \times \nabla\psi$, the barotropic current. The upper layer current, however, is a combination of barotropic and baroclinic parts, plus a direct wind-forced component. The horizontal currents are generally surface intensified.

The theory has been applied to the Lake of Lugano, in southern Switzerland, where a 74 h oscillation has been observed in the summer 1979 temperature and current records. From an analysis of this data we find evidence that this signal is most likely due to a fundamental-mode topographic wave of the type modelled in this paper. In addition to explaining the observed period, phase propagation, isotherm-depth amplitudes along the lake and current motions, the theory has been used to show that the energy level of this oscillation is consistent with the observed amplitude of the wind forcing at the southern end of the lake. However, further work is required on the forced problem to understand the details of the coupling between the atmosphere and the lake at this time scale. In particular, because of the spatial inhomogeneity of the wind forcing over the lake (see figure 26), it appears that traditional forced topographic wave models in which $\boldsymbol{\tau} = \boldsymbol{\tau}(t)$ (see, for example, Huang & Saylor 1982) will have to be extended to include terms proportional to the wind stress curl.

Other theoretical problems that deserve further consideration include an analysis of the validity of the geometrical optics approximation and numerical work on topographic waves in elongated lakes. Possible approaches to the second topic involve finite-element methods (Hamblin 1976), finite difference methods (Bennett & Schwab 1981) and extended channel models (Raggio & Hutter 1982).

PHILOSOPHICAL TRANSACTIONS OF THE ROYAL SOCIETY A MATHEMATICAL, PHYSICAL & ENGINEERING SCIENCES

The theory developed here could also readily be applied to other intermontane lakes of similar scale, such as the Lake of Zurich, where a 100 h oscillation has recently been observed (Mortimer & Horn 1982) and conjectured (Mysak 1985) to be a fundamental-mode elliptical topographic wave. For larger lakes (for example, the Lake of Geneva and the Laurentian Great Lakes) it is possible that low-frequency internal Kelvin waves and gravity seiches may also exist during summer, in addition to topographic waves. To apply the theory to these lakes, one would have to retain the full operator $\mathscr{L} = \partial_{tt} + f^2$ in the governing equation for ζ and in the expressions for $\boldsymbol{u}_1$ and $\boldsymbol{u}_2$. However, the decoupling of the governing equations for ψ and ζ should still hold since generally $D_1 \ll D_2$ applies to these lakes in summer.

This work has been partly supported by the Swiss National Science Foundation under its programme 'Basic Problems of the Swiss Water Budget' through contracts 4.006.0.76.02 (K.H.), 4.011.0.76.02 (G.S.) and through contract 2.829.0.80 (T.S.). L.A.M. was supported by the ETH, Zurich, and the Izaak Walton Killam Memorial Fund for Advanced Studies. His contribution to this paper was made during a sabbatical visit (1982–83) to the limnology group of the Laboratory of Hydraulics, Hydrology and Glaciology, ETH, Zurich.

We are very grateful to C. Bucher for helping to produce the final graphs.

References

Allen, J. S. 1975 Coastal trapped waves in a stratified ocean. *J. phys. Oceanogr.* **5**, 300–325.

Ball, F. K. 1965 Second-class motions of a shallow liquid. *J. Fluid Mech.* **23**, 545–561.

Bennett, J. R. & Schwab, D. J. 1981 Calculation of the rotational normal modes of oceans and lakes with general orthogonal coordinates. *J. comput. Phys.* **44**, 359–376.

Birchfield, G. E. & Hickie, B. P. 1977 The time-dependent response of a circular basin of variable depth to a wind stress. *J. phys. Oceanogr.* **7**, 691–701.

Bloomfield, P. 1976 *Fourier analysis of time series: an introduction.* New York: John Wiley.

Buchwald, V. T. & Adams, J. K. 1968 The propagation of continental shelf waves. *Proc. R. Soc. Lond.* A **305**, 235–250.

Csanady, G. T. 1976 Topographic waves in Lake Ontario. *J. phys. Oceanogr.* **6**, 93–103.

Gratton, Y. 1982 Low-frequency motion on strong topography. *Atmospheric-Ocean* **16** (Congress Issue), 57.

Gratton, Y. 1983 Low-frequency vorticity waves over strong topography. Ph.D. thesis. University of British Columbia.

Hamblin, P. F. 1976 Seiches, circulation, and storm surges of an ice-free Lake Winnipeg. *J. Fish. Res. Bd Can.* **33**, 2377–2391.

Holland, W. R. 1973 Baroclinic and topographic influence on the transport in western boundary currents. *Geophys. Fluid Dyn.* **4**, 187–210.

Horn, W., Mortimer, C. H. & Schwab, D. J. 1983 Wind-induced internal seiche response of the Lake of Zurich compared with predictions of two-layered numerical models. (In preparation.)

Huang, J. C. K. & Saylor, J. H. 1982 Vorticity waves in a shallow basin. *Dyn. Atmos. Oceans* **6**, 177–196.

Hutter, K., Salvadè, G. & Schwab, D. J. 1983 On internal wave dynamics in the northern basin of the Lake of Lugano. *Geophys. astrophys. Fluid Dyn.*, **27**, 299–336.

Jenkins, G. M. & Watts, D. G. 1968 *Spectral analysis and its applications.* San Francisco: Holden-Day.

LeBlond, P. H. & Mysak, L. A. 1978 *Waves in the ocean.* Amsterdam: Elsevier.

Mortimer, C. H. 1952 Water movements in lakes during summer stratification. Evidence from the distribution of temperature in Windermere. *Phil. Trans. R. Soc. Lond.* B **236**, 355–404.

Mortimer, C. H. & Fee, E. J. 1976 Free surface oscillations and tides of Lakes Michigan and Superior. *Phil. Trans. R. Soc. Lond.* A **281**, 1–61.

Mortimer, C. H. & Horn, W. 1982 Internal wave dynamics and their implications for plankton biology in the Lake of Zurich. *Vjschr. naturf. Ges. Zürich* **127**, 299–318.

Mysak, L. A. 1980 Recent advances on shelf wave dynamics. *Rev. Geophys. Space Phys.* **18**, 211–241.

Mysak, L. A. 1985 Elliptical topographic waves. *Geophys. astrophys. Fluid Dyn.* **31**, 93–135.

Raggio, G. & Hutter, K. 1982 An extended channel model for the prediction of motion in elongated homogeneous lakes. Parts 1–3. *J. Fluid Mech.* **121**, 231–299.

PHILOSOPHICAL TRANSACTIONS OF THE ROYAL SOCIETY A MATHEMATICAL, PHYSICAL & ENGINEERING SCIENCES

Rhines, P. B. 1970 Edge-, bottom-, and Rossby waves in a rotating stratified fluid. *Geophys. Fluid Dyn.* **1**, 273–302.
Saylor, J. H., Huang, J. S. K. & Reid, R. O. 1980 Vortex modes in southern Lake Michigan. *J. phys. Oceanogr.* **10**, 1814–1823.
Simons, T. J. 1975 Verification of numerical models of Lake Ontario. II. Stratified circulation and temperature changes. *J. phys. Oceanogr.* **5**, 98–110.
Simons, T. J. 1980 Circulation models of lakes and inland seas. *Can. Bull. Fish. aquat. Sci.* **203**. (146 pages.)
Wright, D. G. & Mysak, L. A. 1977 Coastal trapped waves, with application to the northeast Pacific Ocean. *Atmosphere* **15**, 141–150.

PHILOSOPHICAL TRANSACTIONS OF THE ROYAL SOCIETY A MATHEMATICAL, PHYSICAL & ENGINEERING SCIENCES

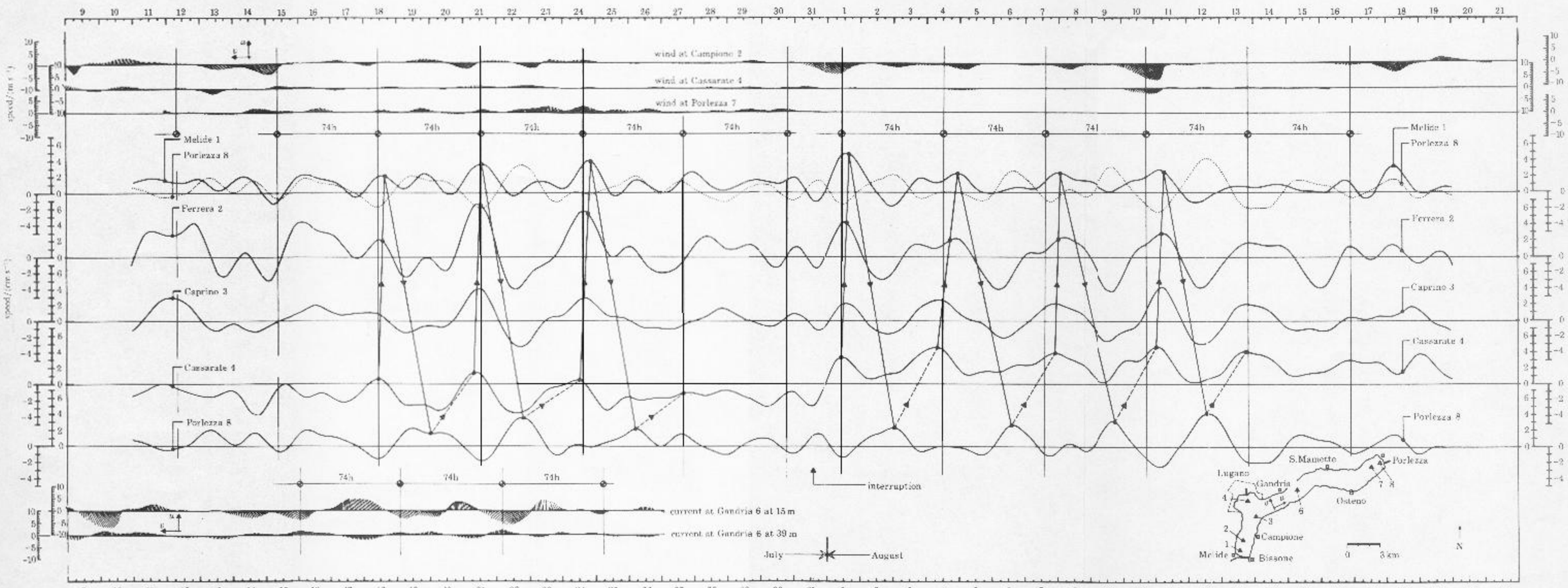

FIGURE 17. Time series for the Lake of Lugano measurements from 9 July to 21 August 1979. The data were smoothed to eliminate all processes with periods shorter than 30 h. At the top, stick plots of the wind at stations Campione (Ferrera) 2, Cassarate 4 and Porlezza 7 are shown (see insert for location). In the middle, the mean temperature displacement functions at Melide 1, Ferrera 2, Caprino 3, Cassarate 4 and Porlezza 8 are displayed. Superimposed on the time series at Melide is that of Porlezza (dotted). At the bottom, stick diagrams of the current at 15 and 39 m depths at Gandria 6 are shown. For both the wind and current, the directions of the components u, v are as indicated in the insert in the lower right corner. For all stations, v is 30° north of east. Vertical lines mark a period of 74 h and the sloping lines indicate the progression of the wave crests (marked with dots).

(*Facing p.* 32)

PHILOSOPHICAL TRANSACTIONS OF THE ROYAL SOCIETY A MATHEMATICAL, PHYSICAL & ENGINEERING SCIENCES